Publication of the Astronomy Department of
the Eötvös University

Volume 13

NATO ADVANCED RESEARCH WORKSHOP

TURBULENCE, WAVES, AND INSTABILITIES IN THE SOLAR PLASMA

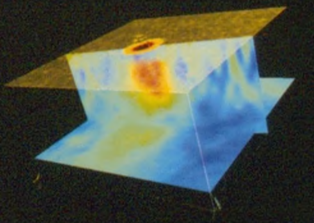

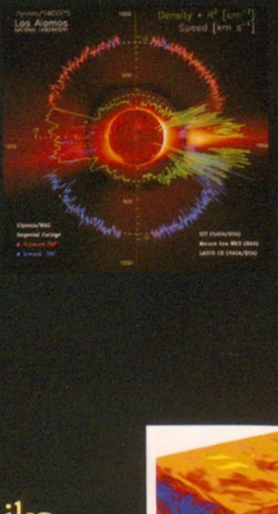

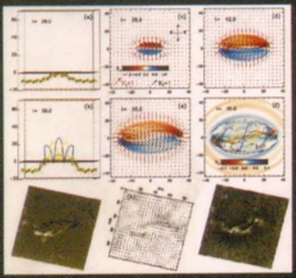

Edited by
E. Forgács-Dajka
K. Petrovay
R. Erdélyi

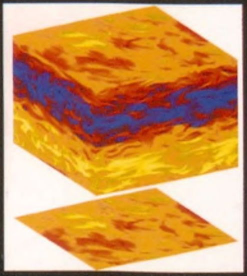

Budapest 2003

Publications of the Astronomy Department of
the Eötvös Loránd University
Vol.13.

NATO
Advanced Research Workshop
Budapest 2002
Turbulence, Waves and Instabilities in the Solar Plasma

NATO ADVANCED RESEARCH WORKSHOP

TURBULENCE, WAVES, AND INSTABILITIES IN THE SOLAR PLASMA

Hungary, 16-20 September 2002

EDITED BY

E. Forgács-Dajka
K. Petrovay
R. Erdélyi

Published by the Department of Astronomy of the Eötvös University
Budapest 2003

Publication of this volume has been aided by the EU 5th Framework Program "European Solar Magnetism Network" (contract no. HPRN-CT-2002-00313) and by the OTKA (grant no. T043741)

ISBN 963 463 557
Responsible publisher: Dr. Bálint Érdi

Contents

Instabilities and Motions in the Solar Interior and Tachocline

Turbulence in the Convective Zone and Photosphere

Parker Instability and Flux Tube Dynamics

Waves and Oscillations in the Solar Atmosphere

Turbulence and Reconnection in the Solar Corona

PREFACE

This volume contains focus reviews, oral contributions and poster papers presented at the NATO Advanced Research Workshop "Turbulence, Waves, and Instabilities in the Solar Plasma", held at Hotel Normafa, Budapest, 16–20 September, 2002. The more exensive invited reviews presented at the same meeting are published by Kluwer in a companion volume, with the same title as that of the meeting.

The purpose of the workshop was to facilitate interchange and communication between diverse groups studying different layers and regions of the Sun but from the same aspect, concentrating on the study of small-scale motions. While the emphasis was on the common theoretical roots of these phenomena, observational aspects were not excluded either.

The selection of invited speakers concentrated on the researchers currently most active in the field, mostly on a post-doctoral/tenure/fresh faculty position level. A number of senior experts and PhD students were also invited. Scientists from NATO partner countries were especially encouraged to apply.

Altogether, 50 scientists from 11 different countries participated in the workshop. The relative isolation of the venue, as well as the fact that the participants all lived at the same place, where the conference was also held, contributed to the success of the meeting, offering plenty of opportunities to meet and exchange ideas.

We are convinced that many of the papers in the present volume will prove to be a very useful reference for some rarely discussed chapters of solar physics.

The Editors

PREFACE

This volume contains focus reviews, oral contributions and poster papers presented at the NATO Advanced Research Workshop "Turbulence, Waves, and Instabilities in the Solar Plasma", held at Hotel Normafa, Budapest, 16-20 September, 2002. The more extensive invited reviews presented at the same meeting are published by Kluwer in a companion volume, with the same title as that of the meeting.

The purpose of the workshop was to facilitate interchange and communication between diverse groups studying different layers and regions of the Sun but from the same aspect, concentrating on the study of small-scale motions. While the emphasis was on the common theoretical roots of these phenomena, observational aspects were not excluded either.

The selection of invited speakers concentrated on the researchers currently most active in the field, mostly on a post-doctoral/tenure/fresh faculty position level. A number of senior experts and PhD students were also invited. Scientists from NATO partner countries were especially encouraged to apply.

Altogether, 50 scientists from 11 different countries participated in the workshop. The relative isolation of the venue, as well as the fact that the participants all lived at the same place, where the conference was also held, contributed to the success of the meeting, offering plenty of opportunities to meet and exchange ideas.

We are convinced that many of the papers in the present volume will prove to be a very useful reference for some rarely discussed chapters of solar physics.

The Editors

List of Participants

Name	Address
Aschwanden, Markus	Lockheed Martin, Solar & Astrophysics Lab. Bldg. / 252 Org./ L9-41, 3251 Hanover Palo Alto, CA 94304, USA E-mail: `aschwanden@lmsal.com`
Ballai, István	SPARC, Dept. of Applied Mathematics Univ. of Sheffield Hounsfield Road, Hicks Building Sheffield, S3 7RH, England, UK E-mail: `i.ballai@sheffield.ac.uk`
Ballester, J. L.	Dept. Fisica. Univ. Illes Balears C. Valldemossa, km 7.5. E - 07071 Palma de Mallorca, Spain E-mail: `dfsjlb0@uib.es`
Baranov, Vladimir	Institute for Problems in Mechanics Russian Academy of Sciences 119526 Moscow Prospect Vernadskogo 101, k. 1, Russia E-mail: `baranov@ipmnet.ru`
Brandenburg, Axel	Nordita Blegdamsvej 17, DK-2100 Copenhagen O Denmark E-mail: `brandenb@nordita.dk`
Chan, Kwing Lam	Astronomy Department, Yale University New Haven, Connecticut, USA E-mail: `maklchan@ust.hk`
De Moortel, Ineke	University of St Andrews North Haugh, St Andrews, KY16 9SS Scotland, UK E-mail: `ineke@mcs.st-and.ac.uk`
De Pontieu, Bart	Lockheed Martin Solar & Astrophysics Lab. Bldg. / 252 Org./ L9-41, 3251 Hanover Palo Alto, CA 94304, USA E-mail: `bdp@lmsal.com`

Erdélyi, Róbert	SPARC, Dept. of Applied Mathematics Univ. of Sheffield Hicks Building, Hounsfield Rd Sheffield, S3 7RH, England, UK E-mail: Robertus@sheffield.ac.uk
Erdős, Géza	KFKI Research Institute for Particle and Nuclear Physics Budapest, Hungary E-mail: erdos@rmki.kfki.hu
Fedun, Viktor	Kiev National University Glushkova St. 6 Kiev Ukraine 03680 E-mail: fedun@mao.kiev.ua
Ferriz-Mas, Antonio	Universidad de Vigo Facultad de Ciencias de Orense Campus Universitario E-32004 Orense, Spain E-mail: antonio.ferriz@oulu.fi
Homem, Miguel	University of Sheffield, SPARC Dept. Applied Maths Hicks Building, S3 7RH Sheffield, UK E-mail: m.homem@sheffield.ac.uk
Hurlburt, Neal	Lockheed Martin Solar and Astrophysics Lab. Bldg. / 252 Org./ L9-41, 3251 Hanover Palo Alto, CA 94304, USA E-mail: hurlburt@lmsal.com
Jahn, Krzysztof	Warsaw University Observatory Al. Ujazdowskie 4, 00-478 Poland E-mail: crj@astrouw.edu.pl
James, Stewart	SPARC, Dept. of Applied Mathematics Univ. of Sheffield Hounsfield Road, Hicks Building Sheffield, S3 7RH England, UK E-mail: s.p.james@shef.ac.uk
Kerekes, Andrea	Eotvos University, Dept. of Astronomy H-1117 Budapest, Pazmany P. setany 1/A Hungary E-mail: a.kerekes@astro.elte.hu

Kitchatinov, Leonid	Institute for Solar-Terrestrial Physics P.O.Box 4026, Irkutsk, 664033, Russia E-mail: `kit@iszf.irk.ru`
Kosovichev, Alexander	Crimean Astrophysical Observatory, Ukraine Nauchny, Crimea, Ukraine E-mail: `AKosovichev@solar.stanford.edu`
Kyzyurov, Yurij	Main Astronomical Observatory NASU Akademika Zabolotnogo Str., 27 Kiev, 03680, Ukraine E-mail: `kyzyurov@mao.kiev.ua`
Ludmány, András	Heliophysical Observatory of the Hung. Acad. of Sci. Debrecen, Hungary E-mail: `ludmany@tigris.klte.ku`
MacGregor, Keith	High Altitude Observatory/NCAR P.O. Box 3000, Boulder Colorado 80307, USA E-mail: `kmac@ucar.edu`
Magara, Tetsuya	Department of Physics Montana State University Bozeman MT59717, USA E-mail: `magara@solar.physics.montana.edu`
Marik, Dániel	Eotvos University, Dept. of Astronomy H-1117 Budapest, Pazmany P. setany 1/A Hungary E-mail: `d.marik@astro.elte.hu`
Mendoza-Briceno, Cesar	SPARC, Dept. of Applied Mathematics Univ. of Sheffield Hicks Building, Hounsfield Road Sheffield, S3 7RH England E-mail: `c.mendoza@sheffield.ac.uk`
Murawski, Kris	Dept. of Complex Physical Systems Fac. of Physics, UMCS Lublin ul. Radziszewskiego 10, 20-031 Lublin, Poland E-mail: `kmurawsk@tytan.umcs.lublin.pl`
Nakariakov, Valery	Nizhny Novgorod State Technical University Nizhny Novgorod, Russia E-mail: `valery@astro.warwick.ac.uk`

Nandi, Dibyendu	Montana State University Department of Physics Bozeman, Montana 59717, USA E-mail: `nandi@mithra.physics.montana.edu`
Norton, Aimee	High Altitude Observatory National Center for Atmospheric Research P.O.Box 3000, 3450 Mitchell Lane Boulder, CO 80307-3000, USA E-mail: `norton@hao.ucar.edu`
Ofman, Leon	Catholic University of America NASA GSFC Code 680, Greenbelt MD 20771, USA E-mail: `Leon.Ofman@gsfc.nasa.gov`
Oliver, Ramon	Departament de Física Universitat de les Illes Balears E-07071 Palma de Mallorca, Spain E-mail: `ramon.oliver@uib.es`
Osokin, Alexei	Sternberg Astronomical Institute Universitetskiy prospect 13 Moscow 119899 Russia E-mail: `arno@sai.msu.ru`
Petkaki, Panagiota	British Antarctic Survey High Cross, Madingley Road Cambridge, CB3 0ET, UK E-mail: `ppe@bas.ac.uk`
Petrovay, Kristóf	Eotvos University, Dept. of Astronomy Budapest, Pf. 32, H-1518 Hungary E-mail: `K.Petrovay@astro.elte.hu`
Primavera, Leonardo	University of Calabria, Dipartimento di Fisica 87036 Arcavacata di Rende (CS) - ITALY E-mail: `lprimavera@fis.unical.it`
Roberts, Bernard	University of St Andrews Mathematical Institute St Andrews, Fife KY16 9SS, Scotland, UK E-mail: `bernie@mcs.st-and.ac.uk`

Ruderman, Michael	Institute for Problems in Mechanics Russian Academy of Sciences Prospect Vernadskogo 101 117526 Moscow, Russia E-mail: `M.S.Ruderman@sheffield.ac.uk`
Rutten, Robert	Sterrekundig Instituut Utrecht Postbus 80 000, NL-3508 TA UTRECHT The Netherlands E-mail: `R.J.Rutten@astro.uu.nl`
Ryutova, Margarita	Budker Institute of Nuclear Physics Lavrentiev Prospect, 11 Novosibirsk 630090, Russia E-mail: `ryutova@igpp.ucllnl.org`
Spruit, Hendrik	MPI for Astrophysics Postfach 1317, Garching, Germany E-mail: `henk@mpa-garching.mpg.de`
Steiner, Oskar	Kiepenheuer-Institut fuer Sonnenphysik Schoeneckstrasse 6 D-79104 Freiburg, Germany E-mail: `steiner@kis.uni-freiburg.de`
Taroyan, Youra	SPARC, Dept. of Applied Mathematics Univ. of Sheffield The Hicks Building, Hounsfield Road Sheffield S3 7RH, UK E-mail: `Y.Taroyan@shefield.ac.uk`
Title, Alan	Stanford/Lockheed Institute for Space Research (LMATC) 3251 Hanover St.,Palo Alto, CA 94304, USA E-mail: `title@lmsal.com`
Tóth, László	Heliophysical Observatory of the Hung. Acad. of Sci. Debrecen, Hungary E-mail: `tothla@tigris.klte.ku`
van **Driel-Gesztelyi**, Lídia	Observatoire de Meudon Paris, France E-mail: `Lidia.vanDriel@obspm.fr`
Vekstein, Grigory	UMIST P.O.Box 88, Manchester M60 1QD, UK E-mail: `g.vekstein@umist.ac.uk`

Voytenko, Yuriy
Main Astronomical Observatory (NASU)
Kyiv, Ukraine
E-mail: `Yuriy.Voitenko@wis.kuleuven.ac.be`

Wills-Davey, Meredith
Montana State University
Physics Department
EPS 264, Bozeman, MT 59717, USA
E-mail: `meredith@solar.physics.montana.edu`

Zaqarashvili, Teimuraz
Abastumani Astrophysical Observatory
Al. Kazbegi ave. 2a, 380060 Tbilisi, Georgia
E-mail: `temury@mail.ge`

Zhugzhda, Yuzef
IZMIRAN
Troitsk, Moscow Region, 142092 Russia
E-mail: `zhu@izmiran.rssi.ru`

PART ONE

INSTABILITIES AND MOTIONS IN THE SOLAR INTERIOR AND TACHOCLINE

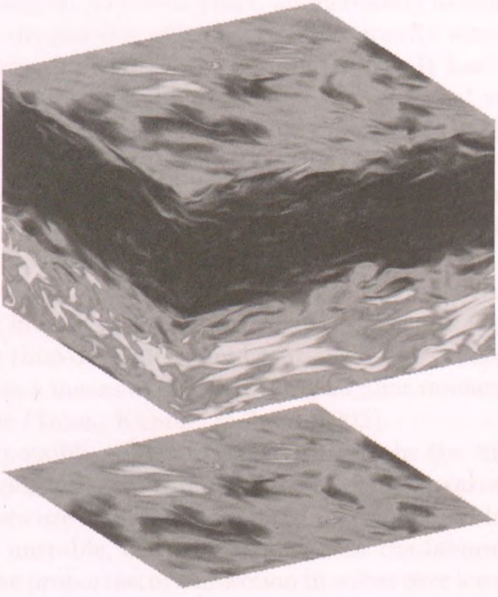

GRAVITY WAVES IN THE RADIATIVE ZONE AND TACHOCLINE

K. B. MacGregor
High Altitude Observatory, National Center for Atmospheric Research
P. O. Box 3000, Boulder, CO 80307-3000, U. S. A.
E-mail: `kmac@ucar.edu`

Abstract

We review the properties of internal gravity waves under physical conditions like those of the solar radiative interior, and consider a few of the ways in which such disturbances might influence the dynamical structure of the tachocline region.

1. Introduction

Disturbances in an incompressible fluid that is stably and continuously stratified under the influence of an external gravitational force take the form of internal waves. Waves of this kind have long been studied by geophysical fluid dynamicists, who have invoked their properties to explain a diversity of flow phenomena in the Earth's atmosphere and oceans. In recent years, an increasing amount of attention has also been given to the possible effects of internal gravity waves on the structure and dynamics of the interiors of the Sun and stars. It has been suggested, for example, that the fluid motions associated with internal waves can contribute to compositional mixing in the innermost portion of the Sun's radiative core (Press, 1981), as well as in the layers immediately below the convection zone (Garcia-Lopez & Spruit, 1991; Schatzman, 1996; Fritts, Vadas, & Andreassen, 1998). Mixing by gravity waves in this latter region might play a role in the overall process by which Li is depleted in the envelopes of the Sun and solar-type stars. Similarly, the interaction between propagating gravity waves and a shear flow has been investigated within the context of solar physics both as a mechanism for forcing time-dependent fluid motions in the tachocline (Kim & MacGregor, 2001), and as a means of redistributing angular momentum throughout the radiative interior (Talon, Kumar, & Zahn, 2002).

Impetus for examining the possible effects of gravity waves in the Sun is provided by the following fact, gleaned from careful observations of a variety of terrestrial systems: internal waves are commonly detected in stable fluid layers that are located adjacent to an unstable, convective region. In the laboratory, experiments designed to study the properties of convection in water over ice show fluctuations in the stable fluid layer that are identifiable as internal gravity waves (Townsend, 1964; Adrian, 1975). Evidently, these disturbances are excited when convective fluid motions deform the interface between the stable and unstable regions within the liquid volume. In the atmosphere, vertically propagating internal gravity waves are observed in the stable layers that overlie convective storm systems (see, e.g., Alexander, Holton, & Durran, 1995, and references therein). These waves are thought to result from the interaction of rising/sinking convective elements with the stable air above a cumulus cloud, in particular, from mechanical or thermal forcing of overlying stationary layers, or from the obstruction and deflection of a background horizontal wind flow (Fovell, Durran, & Holton, 1992).

The examples cited in the preceding paragraph suggest that gravity waves are likely to be present in the radiative regions that abut the Sun's convection zone at its upper and lower boundaries. Convective flow time scales at both interfaces exceed the local period of buoyancy oscillations, so that the impact of these motions on neighboring stably stratified layers would seem to be a natural mechanism for producing internal waves. In subsequent sections of this paper, we adopt the foregoing picture of gravity wave generation inside the Sun as a working assumption, and examine how such disturbances might affect the radiative layers just beneath the base of the convection zone. In sections 2 and 3, we briefly review the properties of hydrodynamic (HD) gravity waves, and consider some of the ways in which radiatively damped waves can modify the dynamics of the tachocline. In section 4, we describe the properties of magnetohydrodynamic (MHD) gravity waves, and conclude in section 5 by investigating the possibility of wave reflection and ducting by the magnetic and shear structure associated with the tachocline.

2. Properties and Propagation of HD Gravity Waves

The present paper is concerned with physical processes involving inward propagating waves that originate in the overshoot region at the bottom of the solar convective envelope. Of particular interest is the interaction between such waves and the flow and magnetic field that exist within the tachocline, the rotational shear layer that directly underlies the radiative-convective interface. Helioseismic inferences regarding the structure of the tachocline indicate that it is geometrically thin, having a radial extent at equatorial latitudes $\approx 0.04\ R_\odot$ (Charbonneau et al., 1999). In view of this, the following exposition of gravity wave properties is most easily carried out using a local Cartesian coordinate system in which the directions of increasing x, y, and z correspond, respectively, to the directions in which the spherical polar coordinates θ, ϕ, r increase.

Consider a stationary ($\mathbf{u} = 0$), unmagnetized ($\mathbf{B} = 0$) fluid in which the local pressure p and mass density ρ satisfy the force balance equation $\mathrm{d}p/\mathrm{d}z = -g\rho$, where $\mathbf{g} = -g\ \mathbf{e}_z$ is the (assumed) constant acceleration due to gravity. Wave-like disturbances to this hydrostatic equilibrium state can be investigated by examining the linearized mass, momentum, and energy conservation equations that govern the behavior of the infinitesimal perturbations δp, $\delta\rho$, and $\delta\mathbf{u} = \delta u_y\ \mathbf{e}_y + \delta u_z\ \mathbf{e}_z$ (see, e.g., the treatments given by Turner, 1973; Lighthill, 1978). The linearized equations can be further simplified by applying the Boussinesq approximation, under which the variation in density $\delta\rho$ is neglected in expressions involving the fluid inertia but retained in the buoyant force (see Spiegel & Veronis, 1960, for a more complete discussion). If the vertical velocity fluctuation (from which all other perturbation quantities can be derived) is assumed to have the form of a traveling wave, $\delta u_z = \delta\hat{u}_z(z)\ \exp\left[i(ly - \omega t)\right]$ with l and ω constants, then it can be shown that the amplitude $\delta\hat{u}_z$ satisfies

$$\frac{\mathrm{d}^2\delta\hat{u}_z}{\mathrm{d}z^2} + m^2\delta\hat{u}_z = 0, \tag{1}$$

where

$$m^2 = l^2\left[(N/\omega)^2 - 1\right], \tag{2}$$

and

$$N^2 = -(g/\rho)\ (\mathrm{d}\rho/\mathrm{d}z). \tag{3}$$

The quantity N is the so-called Brunt-Väisälä or buoyancy frequency; an adiabatic fluid element that undergoes a small vertical displacement from its equilibrium position in the stably stratified background will oscillate around that location with angular frequency $\omega = N$. For the case in which N is independent of z and $\omega < N$, equations (1) and (2) indicate that $\delta\hat{u}_z \sim \exp\ (imz)$, and small disturbances in the medium are propagating plane waves with horizontal wavenumber l and vertical wavenumber m. It is also apparent from the above relations that $\omega = N$ is the maximum frequency of an internal wave since, when $\omega > N$, small disturbances decay exponentially.

Equation (2) can be rewritten in the form of a dispersion relation for internal gravity waves,

$$\omega = N\left(\frac{l^2}{l^2 + m^2}\right)^{1/2} = N\ \cos\theta, \tag{4}$$

where θ is the angle between a plane of constant phase and the vertical. According to equation (4), specification of N (a property of the background stratification) and ω (presumably determined by the wave excitation mechanism) determine the direction of propagation of the wave (for experimental verification, see Mowbray & Rarity, 1967). Note that conservation of mass in the Boussinesq approximation requires the wavevector $\mathbf{k} = (0, l, m)$ to be perpendicular to the fluctuating velocity $\delta\mathbf{u}$, so that the fluid motions associated with the wave take place within planes of constant phase. These motions are driven by the net force due to the pressure gradient $-\nabla\, \delta p$ ($\parallel \mathbf{k}$) and buoyancy $-\mathbf{g}\, \delta\rho$ ($\parallel \mathbf{e}_z$). For waves with $\omega \approx N$, it follows from (4) that $\theta \approx 0$, and the phase surfaces are nearly horizontally propagating while the fluid motions are nearly vertical. For waves with $\omega \ll N$, the dispersion relation indicates that $\theta \approx \pi/2$, and the phase propagation is close to vertical while the fluid motions are approximately horizontal. Note that the wave phase travels in the **k**-direction while the wave energy flux, given as an average of the quantity $\delta p\, \delta\mathbf{u}$ (see, e.g., Lighthill, 1978), must be parallel to $\delta\mathbf{u}$. Hence, on the basis of the preceding discussion, the phase velocity

$$\mathbf{v}_p = \omega\mathbf{k}/k^2 = \left(N \mid l \mid l/k^3\right)\, \mathbf{e}_y + \left(N \mid l \mid m/k^3\right)\, \mathbf{e}_z \tag{5}$$

and the group velocity

$$\mathbf{v}_g = \partial\omega/\partial\mathbf{k} = \left(N l m^2/k^3 \mid l \mid\right)\, \mathbf{e}_y - \left(N \mid l \mid m/k^3\right)\, \mathbf{e}_z \tag{6}$$

of hydrodynamic internal gravity waves in a stationary medium are perpendicular, $\mathbf{v}_p \cdot \mathbf{v}_g = 0$.

3. Gravity Wave-Driven Flows in the Tachocline

The focus of the present section is one of several interesting physical effects that can occur when internal gravity waves propagate through a stratified medium in which there is a mean shear flow. In the presence of a fluid velocity $\mathbf{u} = u(z)\, \mathbf{e}_y$, the wave dispersion relation becomes

$$m^2 = l^2\, \left[N^2/(\omega - lu)^2 - 1\right], \tag{7}$$

through which modification the y-components of the phase and group velocities (cf. eqs. [5] and [6]) acquire an advective contribution. For waves with vertical wavelengths that are small in comparison to the length scales over which the properties of the background medium vary (i.e., waves for which the WKB approximation is valid), it can be shown (e.g., Bretherton, 1966) that the Reynolds stress is

$$\rho \langle \delta u_y \, \delta u_z \rangle = l v_{gz} E/(\omega - lu) \equiv l\mathcal{F}, \tag{8}$$

where $\langle \, \rangle$ denotes an average and $E = \frac{1}{2} \langle \delta u^2 + N^2 \delta z^2 \rangle$ is the wave energy density. The quantity $l\mathcal{F}$ given by equation (8) represents a vertical flux of horizontal momentum per unit area, and is constant as a function of z for a fluid in which waves can propagate without dissipation. However, non-zero dissipation provides the means for waves to interact with the mean flow, causing a transfer of momentum to the background medium through the agency of a force density $-l \; (\partial \mathcal{F}/\partial z) \; \mathbf{e}_y$.

The process by which gravity waves can force flows in a dissipative fluid has received much attention, particularly in atmospheric science where it is believed to play a role in producing the so-called quasi-biennial oscillation (QBO), the periodic reversal of the direction of the mean zonal winds in the equatorial stratosphere (see, e.g., Plumb, 1977). Here we consider the consequences of the wave-mean flow interaction for the dynamics of the solar tachocline (Kim & MacGregor, 2001). Specifically, we situate the previously defined Cartesian coordinate system in such a way that the plane $z = 0$ coincides with the base of the convection zone, and adopt as the computational domain a layer extending to a depth $-H_0/2$, where H_0 ($\approx 0.08 \; R_\odot$) is the pressure scale height at the upper boundary. The physical properties of the background medium are specified as functions of depth within the domain according to the solar interior model of Bahcall and Pinsonneault (1995). The lower boundary is assumed to move with horizontal velocity $\mathbf{u}_0 = -10^4 \; \mathbf{e}_y$ cm s^{-1} relative to the stationary upper boundary, consistent with helioseismic inferences regarding the rotational velocity difference across the tachocline at equatorial latitudes. Two internal gravity waves (heareafter designated '+' and '−') with opposite senses of horizontal propagation are continuously emitted from the upper boundary. These waves have identical amplitudes δu_{z0} and frequencies ω, and wavevectors $\mathbf{k}_\pm = \pm \mid l \mid \mathbf{e}_y + m_\pm \mathbf{e}_z$. The waves have $\omega \ll N_0 \approx 2.5 \times 10^{-3}$ s^{-1}; their periods are long in comparison to typical radiative heating/cooling times, so that they are strongly damped.

Kim and MacGregor (2001) have studied the properties of the flows $u(z,t) \; \mathbf{e}_y$ that are produced within the layer when the force arising from radiatively damped waves is counteracted by the force due to a large-scale, turbulent viscosity ν. If the values of ω, $\mid l \mid$, and and δu_{z0} are held constant, they find that there exists a limiting value of ν above which the wave and viscous forces

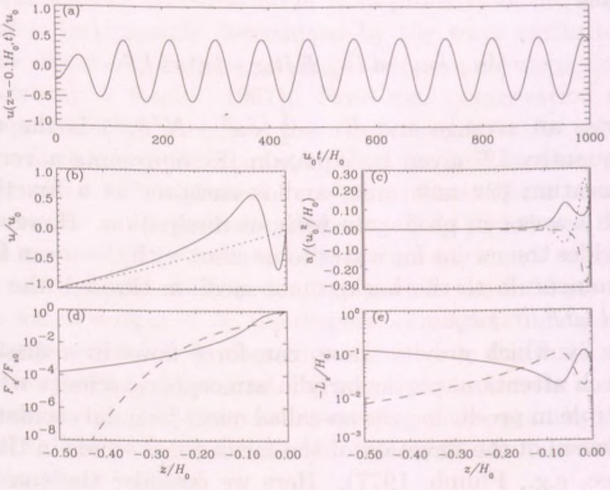

Figure 1: The periodic gravity wave-driven flow obtained for $\omega/N_0 = 2 \times 10^{-3}$, $| l |= H_0^{-1}$, $\delta u_{0z} = 59$ cm s^{-1}, and $\nu = 3 \times 10^9$ cm^2 s^{-1}. (a) The flow velocity as a function of t at $z = -0.1\ H_0$. (b) Profile of u within the layer at $u_0 t/H_0 = 125$ (solid line). The dotted line is the steady viscous flow solution without waves. (c) The accelerations produced by the + wave (solid line), the − wave (dashed line), and visocity (dotted line). (d) The momentum fluxes (cf. eq. [8]) associated with the + and − waves. (e) The radiative damping lengths of the + and − waves.

balance throughout the layer, resulting in shear flows that are time-stationary. Lowering ν from the limiting value by a small amount leads to periodic flow solutions, in which $u(z,t)$ at a given point oscillates in time with a single fixed frequency. An example of this kind of solution, the dynamics of which has much in common with the terrestrial atmospheric QBO, is shown in Figure 1. We note that the characteristic length scales $L_\pm$ over which the waves are radiatively damped vary like $L_\pm \sim (\omega \mp \mid l \mid u)^4$, and that the forces produced by the waves are given by $\pm \mid l \mid \mathcal{F}_\pm / L_\pm$ with $\mathcal{F}_\pm$ as defined in equation (8). As a result of these dependences, the magnitude of the force associated with the wave whose horizontal component of propagation is aligned with the local flow velocity exceeds that due to its oppositely directed counterpart. This behavior leads to flow profiles in which the mean flow direction reverses with increasing depth, thereby creating and accentuating regions of strong shear. The interplay between this process and viscous diffusion within the shear layers that form is responsible for the time dependence of the mean flow.

If the viscosity is continuously reduced to still lower values, the flow evolves through the following sequence of distinct time-dependent behaviors: (i) a second oscillation frequency appears that is incommensurate with the first, marking the onset of quasi-periodic fluid motions; (ii) the two frequencies both continue to decrease with decreasing viscosity until their ratio becomes equal to the ratio of two whole numbers, at which point phase locking occurs and periodic motion resumes; (iii) for a sufficiently small value of the viscosity (e.g., $\nu \approx 10^8$ cm^2 s^{-1} for the solution depicted in Figure 1), the motion becomes non-periodic, indicative of a transition to completely chaotic behavior. The variety of complex, time-dependent shear flows that can be produced by gravity wave interactions under solar interior conditions is of particular interest in light of recent reports of helioseismically detected periodic variability in the rotation rate of a layer located in the vicinity of the tachocline (Howe et al., 2000).

4. Properties and Propagation of MHD Gravity Waves

In the preceding section, we described the kinds of time-dependent flows that might take place in the tachocline region, produced by the interaction between downward propagating, hydrodynamic gravity waves and the mean rotational shear. In fact, several lines of evidence suggest that the tachocline contains a strong ($\approx 10^5$ G), toroidal magnetic field, and that this layer together with its environs is likely to be a principal site of hydromagnetic dynamo activity inside the Sun (see, e.g., the contribution by Petrovay to this conference). The presence of a background field leads to modifications in the properties of internal gravity waves, giving these disturbances an Alfvénic character indicative of the fact that the restoring force for the wave motion arises from both buoyancy and magnetic tension.

Accordingly, we adopt the local Cartesian coordinate system used in the previous analysis, and briefly consider the behavior of internal waves in a stratified medium containing a horizontal (i.e., toroidal) magnetic field $\mathbf{B} = B(z)\ \mathbf{e}_y$. The procedure outlined in section 1 can be straightforwardly extended to treat waves that also have a magnetic fluctuation $\delta\mathbf{B} = \delta B_y\ \mathbf{e}_y + \delta B_z\ \mathbf{e}_z$ in the MHD Boussinesq approximation (Barnes, MacGregor, & Charbonneau, 1998). Application of this approach to the case in which there is no mean flow ($\mathbf{u} = 0$) yields the dispersion relation

$$m^2 = l^2\ \left[N^2/(\omega^2 - l^2 u_A^2) - 1\right], \qquad (9)$$

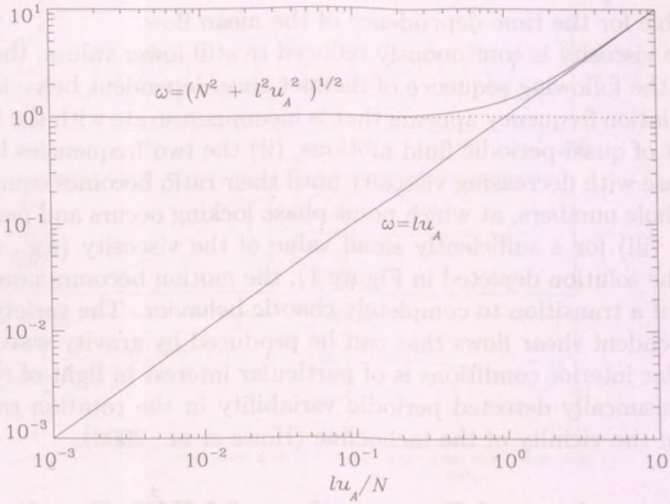

Figure 2: The region in the $l\omega$-plane for which propagating MHD gravity waves are possible, as described in the text. When $\mathbf{B}=0$, hydrodynamic gravity waves are possible for $\omega/N<1$, that is, the region below the dotted line in the figure.

and group velocity

$$\mathbf{v}_g = \left(lu_A^2/\omega\right)\mathbf{e}_y + \left(N^2/k^4\omega\right)\left(lm^2\mathbf{e}_y - l^2m\mathbf{e}_z\right), \tag{10}$$

where $u_A = B/\sqrt{4\pi\rho}$ is the Alfvén speed and the other symbols are as defined in sections 2 and 3.

From equation (9) it is evident that m is real and that MHD internal wave propagation is possible only if $l^2u_A^2 < \omega^2 < N^2 + l^2u_A^2$. For waves with horizontal components of propagation in the $+\mathbf{e}_y$-direction, the portion of the $l\omega$-plane in which these inequalities are simultaneously satisfied is delineated by the two solid lines in Figure 2. Note that for MHD internal waves, $\mathbf{k}\cdot\delta\mathbf{u} = \mathbf{k}\cdot\delta\mathbf{B} = 0$, so that both velocity and magnetic fluctuations are contained in planes perpendicular to $\mathbf{k}$. Near the upper boundary, $\omega \approx N$ for $(lu_A/N) \ll 1$, and the waves are like ordinary hydrodynamic gravity waves with horizontal phase propagation and vertical fluid motions. For $(lu_A/N) \gg 1$, $\omega \approx lu_A$, the magnetic tension force dominates buoyancy, and the waves are like Alfvén waves that propagate along the horizontal magnetic field. On the lower boundary in Figure 2, $\mathbf{k}$ is in the vertical direction, implying that $\delta\mathbf{u}$ and $\delta\mathbf{B}$ are perpendicular to $\mathbf{g}$ and along

B, thereby eliminating buoyancy and magnetic tension as restoring forces for the wave motion. Outside the boundaries indicated in the figure, MHD gravity waves are evanescent. This is unlike the hydrodynamic (i.e., $\mathbf{B} = 0$) case, in which propagating wave solutions are possible for any combination of l and ω below the dotted line in Figure 2.

5. Reflection and Ducting of MHD Gravity Waves

Because of the strong frequency dependence of the radiative damping length noted in section 3, higher frequency waves suffer less attenuation and may therefore be capable of penetrating more deeply into the solar core. However, in crossing the tachocline region, these waves may encounter vertical structure in the background magnetic field or shear flow having a scale sufficient to cause the reflection of a significant fraction of the downward propagating flux. To see how this process might affect MHD gravity waves in the solar interior, consider a stationary ($\mathbf{u} = 0$), stratified medium in which ρ varies continuously with z, but in which the plane $z = 0$ is a current sheet, so that $\mathbf{B} = B_1\,\mathbf{e}_y$ for $z > 0$ and $\mathbf{B} = B_2\,\mathbf{e}_y$ for $z < 0$ where $B_{1,2}$ are constants. A wave with $l > 0$ that travels downward from region 1 into region 2 will experience a discontinuous change in the Alfvén speed, from u_{A1} to u_{A2}, at $z = 0$.

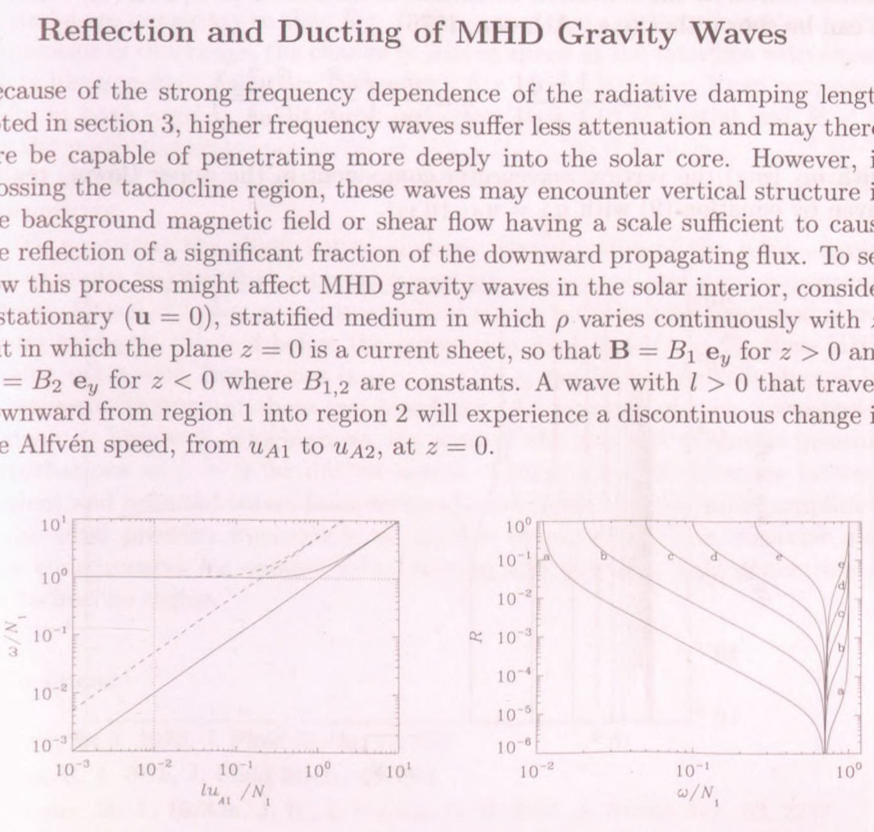

Figure 3: The reflection of MHD gravity waves from a discontinuous horizontal magnetic field. The left-hand panel shows the l and ω values for propagating waves in regions with Alfvén speeds u_{A1} (solid lines) and $u_{A2} = 5\,u_{A1}$ (dashed lines). The right-hand panel shows the reflection coefficient as a function of ω for waves with $(lu_{A1}/N_1) = 10^{-2}$ (i.e., along the vertical dotted line in the left panel). The curves labelled *a*-*e* correspond to Alfvén speed ratios $u_{A2}/u_{A1} = 1.1$, 2.0, 5.0, 10.0, and 25.0, respectively.

The situation outlined above can be readily analyzed by assuming that the solution consists of incident (i) and reflected (r) plane waves in region 1 and a transmitted (t) plane wave in region 2. Imposition of conditions ensuring continuity of the vertical displacement and the total (i.e., gas plus magnetic) pressure across the interface then yields the results $\omega_i = \omega_r = \omega_t$, $l_i = l_r = l_t$, together with expressions for the vertical velocity amplitudes of the reflected and transmitted waves. If the reflection coefficient is defined as $R \equiv \mid \delta\hat{u}_{zr}(0)/\delta\hat{u}_{zi}(0) \mid$, it can be shown that (e.g., Acheson, 1976)

$$R = \frac{\mid 1-q \mid}{\mid 1+q \mid}, \quad q = \frac{m_2}{m_1}\left(\frac{\omega^2 - l^2 u_{A2}^2}{\omega^2 - l^2 u_{A1}^2}\right), \tag{11}$$

with m_1 (m_2) the vertical wavevector component in the upper (lower) region, given by equation (9) with $u_A = u_{A1}$ (u_{A2}).

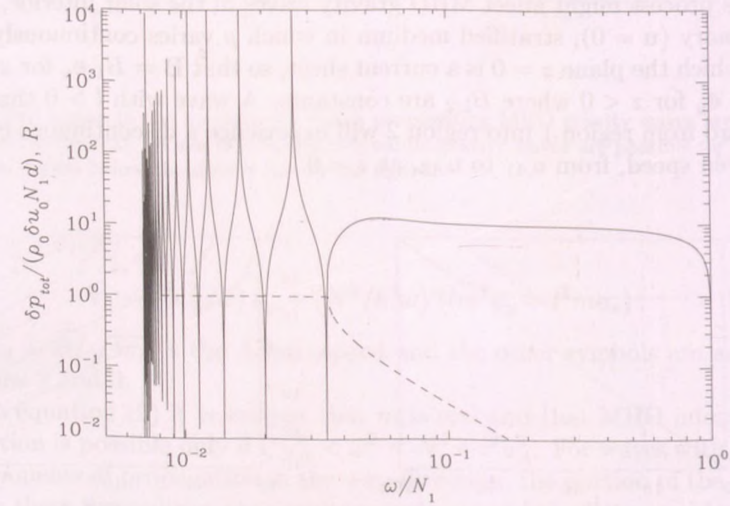

Figure 4: MHD gravity wave modes in a horizontal duct of vertical extent d for a case with $(lu_{A1}/N_1) = 7 \times 10^{-3}$, $u_{A2}/u_{A1} = 5$, and $ld = 0.1$. The solid curve is the total pressure perturbation at $z = 0$, and the dashed curve is the reflection coefficient (see Fig. 3).

The variation of R with ω is shown for $(lu_{A1}/N_1) = 10^{-2}$ and several different values of the ratio u_{A2}/u_{A1} in the right-hand panel of Figure 3. The behavior seen there can be understood by examination of the left-hand side of the figure, which depicts the portions of the $l\omega$-plane in which propagating waves are possible in regions 1 (solid lines) and 2 (dashed lines) for the particular case of $u_{A2}/u_{A1} = 5$ (curve c in the right panel). Proceeding in the direction of higher frequencies along the vertical dotted line, MHD gravity waves cannot propagate in either region 1 or 2 for $\omega/N_1 < 10^{-2}$ (i.e., below the lower solid line in the figure). For $10^{-2} < \omega/N_1 < 5 \times 10^{-2}$ (i.e., between the solid and dashed lines), waves can propagate in region 1 but are evanescent in region 2, implying that m_2 and q are imaginary so that $R = 1$. For waves that originate in region 1 with frequencies in this range, the change in Alfvén speed at the interface with region 2 acts like a perfect reflector. Waves with $5 \times 10^{-2} < \omega/N_1 < 1$ can propagate freely in both regions, so that the reflection at $z = 0$ is partial and $R < 1$. For the particular frequency $\omega/N_1 = \frac{1}{2}\{1 + (lu_{A1}/N_1)^2\ [1 + (u_{A2}/u_{A1})^2\ ]\}^{1/2}$, $q = 1$, so that $R = 0$ and the interface between regions 1 and 2 is perfectly transmitting.

We note that the slight super-adiabatic stratification of the solar convective envelope implies that internal waves are evanescent and non-propagating therein. Hence, if a change in toroidal field strength of the kind described above occurs at depth $z = -d$ below the convection zone base ($z = 0$), then MHD gravity waves with frequencies $lu_{A1} < \omega < lu_{A2}$ can be horizontally ducted by successive reflections at these two interfaces. An example of such a waveguide is given in Figure 4, which shows the sum of the gas and magnetic pressure perturbations at $z = 0$ for ducted waves. Constructive interference between incident and reflected waves leads to significant enhancements in the amplitude of the total pressure fluctuation at discrete frequencies. This behavior may have consequences for compositional mixing and magnetic field generation in the tachocline region.

References

Acheson, D. J. 1976, J. Fluid Mech., 77, 433

Adrian, R. J. 1975, J. Fluid Mech., 69, 753

Alexander, M. J., Holton, J. R., & Durran, D. R. 1995, J. Atmos. Sci., 52, 2212

Bahcall, J., & Pinsonneault, M. 1995, Rev. Mod. Phys., 67, 781

Barnes, G., MacGregor, K. B., Charbonneau, P. 1998, ApJ, 498, L169

Bretherton, F. P. 1966, Quart. J. R. Met. Soc., 92, 466

Charbonneau, P., Christensen-Dalsgaard, J., Henning, R., Larsen, R. M., Schou, J., Thompson, M. J., & Tomczyk, S. 1999, ApJ, 527, 445

Fovell, R., Durran, D., & Holton, J. R. 1992, J. Atmos. Sci., 49, 1427

Fritts, D. C., Vadas, S. L., & Andreassen, O. 1998, A&A, 333, 343

Garcia-Lopez, R. J., & Spruit, H. C. 1991, ApJ, 377, 268

Howe, R., Christensen-Dalsgaard, J. Hill, F., Komm, R. W., Larsen, R. M., Schou, J., Thompson, M. J., & Toomre, J. 2000, Science, 287, 2434

Kim, E. -J., & MacGregor, K. B. 2001, ApJ, 556, L117

Lighthill, J. 1978, Waves in Fluids, Cambridge Univ. Press

Mowbray, D. E., & Rarity, B. S. H. 1967, J. Fluid Mech., 28, 1

Plumb, R. A. 1977, J. Atmos. Sci., 34, 1847

Press, W. H. 1981, ApJ, 245, 286

Schatzman, E. 1996, J. Fluid Mech., 322, 355

Spiegel, E. A., & Veronis, G. 1960, ApJ, 131, 442

Talon, S., Kumar, P., & Zahn, J. -P. 2002, ApJ, 547, L175

Townsend, A. A. 1964, Quart. J. Roy. Met. Soc., 90, 248

Turner, J. S. 1973, Buoyancy Effects in Fuids, Cambridge Univ. Press

INSIGHTS ON TURBULENT FLOWS IN THE SOLAR INTERIOR FROM THE BEHAVIOUR OF DYNAMO GENERATED MAGNETIC FIELDS

Dibyendu Nandy[1,2] **and Arnab Rai Choudhuri**[2]
[1]Department of Physics, Montana State University Bozeman, MT 59717, USA
[2]Department of Physics, Indian Institute of Science Bangalore 560012, India
E-mail: [1]`nandi@mithra.physics.montana.edu`, [2]`arnab@physics.iisc.ernet.in`

Abstract

Turbulent flows in the interior of the Sun, both at small and large scales, are believed to feed and sustain the solar hydromagnetic dynamo that generates the solar cycle. The solar cycle itself strikingly manifests in a 11-year periodic variation in the number of sunspots seen on the solar surface. Sunspots are regions of concentrated magnetic fields, occurring at low latitudes on the solar surface and are believed to be tracers of the underlying dynamo mechanism. An important ingredient in recent models of the dynamo mechanism is the meridional flow of material, which is believed to originate from turbulent stresses in the solar convection zone. This meridional circulation is observed to be poleward in the outer 15% of the Sun and must be balanced by an equatorward counterflow in the interior. The nature and exact location of this counterflow, however, is unknown. We discuss here results from a dynamo model that reproduces the correct latitudinal distribution of sunspots and show that this requires a meridional counterflow of material that penetrates much deeper than hitherto believed – into the radiative layers below the convection zone. We comment on the viability of such a deep counterflow of material and discuss its implications for turbulent convection and elemental abundance in the Sun and related stellar atmospheres.

KEYWORDS: *Sun, MHD, dynamo, turbulence, meridional circulation*

1. Introduction

Understanding the exact nature of the solar dynamo, which involves complex and non-linear interactions between the plasma motions and magnetic fields in the solar interior, remains an elusive problem. In what follows, we briefly outline some of its main features, about which a consensus view has emerged in recent years.

Under the assumption of axisymmetry, the magnetic field in spherical geometry (as appropriate for the Sun) can be expressed as

$$\mathbf{B} = B_\phi \mathbf{e}_\phi + \nabla \times (A \mathbf{e}_\phi). \qquad (1)$$

The first term on the right hand side of the above equation is known as the toroidal component and the second term as the poloidal component of the magnetic field. The toroidal magnetic field is generated in the solar interior by the stretching of the poloidal component by the differential rotation (Parker, 1955). Helioseismology has now mapped the internal rotation of the Sun (Schou et al., 1998) and with the accompanying discovery of the tachocline - a region of substantial radial shear in the rotation, it is now fairly certain that the strong toroidal fields are produced in this tachocline region at the base of the solar convection zone (SCZ).

Due to its buoyancy, the strong toroidal flux tubes rise up radially from the base of the SCZ to the surface, forming sunspots. Simulations of this buoyant rise (Choudhuri and Gilman, 1987; D'Silva and Choudhuri, 1993) and flux storage (Moreno-Insertis, Schüssler and Ferriz-Mas, 1992), have established that the strong "sunspot-forming" toroidal field at the base of the SCZ must be of the order of 10^5 Gauss (G). The strength of the equipartition magnetic field (assuming equipartition between the magnetic and turbulent energies) in the SCZ is only of the order of 10^4 G. The classical α-effect, which involves the twisting of the rising toroidal field by helical turbulence to regenerate the poloidal field (Parker, 1955), cannot work on such strong super-equipartition field. Therefore, alternative mechanisms for the regeneration of the poloidal field are necessary. One of these alternative scenarios which has received considerable attention in the recent past is the Babcock and Leighton (hereafter BL) mechanism for the α-effect – which recognizes that the decay of tilted bipolar sunspot pairs on the solar surface can regenerate the poloidal field (Babcock, 1961; Leighton, 1969).

We may point out here that some questions have been raised recently regarding (solar-like) parity violation by BL models (Dikpati and Gilman, 2001). There are also alternate attempts to build overshoot layer and interface dynamo models. Detailed discussion on these issues are beyond the scope of this short paper and from now on we concentrate on our specific BL type model for the solar dynamo.

2. The Babcock-Leighton Dynamo

We have constructed a solar dynamo model (with helioseismically determined rotation pattern) based on the BL idea by invoking an α-effect that is concentrated in a thin layer near the solar surface (Choudhuri, Schüssler and Dikpati, 1995; Nandy and Choudhuri, 2001). Motivated by results from simulations of flux storage and the buoyant rise of toroidal flux tubes we have implemented a buoyancy algorithm where toroidal fields exceeding 10^5 G are made to erupt (from the base of the SCZ) to the surface layers. The α-effect acts on this erupted toroidal field to produce the poloidal field. The poloidal field thus produced in the surface layers is first transported polewards by a combined action of the poleward meridional flow and diffusivity and then downwards to the high latitude tachocline by the meridional down-flow near the poles.

A poleward meridional flow pervading the outer half of the SCZ is observed (Braun and Fan, 1998). From mass conservation, it follows that there must be an equatorward counterflow somewhere in the solar interior. The exact location of this counterflow has, however, eluded helioseismic detection till date. Using a flow profile that is confined mainly to SCZ and the tachocline (as depicted in Fig. 1, top-left) and our model for the BL dynamo, we generate a Butterfly diagram for the toroidal field at the base of the SCZ (Fig. 1, bottom-left). It is clear from the Butterfly diagram that strong toroidal fields form at high latitudes. The shaded regions, denoting the latitudes at which buoyant eruptions occur with the progress of the cycle, show that these simulated sunspot eruptions are confined to high latitudes, contrary to observations.

In such BL dynamo models the poloidal field is generated only in a thin layer near the solar surface. The only way this poloidal field can be brought down to the tachocline for the re-generation of the toroidal field is by the meridional down-flow near the poles. Thus the sinking poloidal field hits the high latitude tachocline first. Helioseismic inversions show that the radial shear in the tachocline, which is negative at high latitudes and positive at low latitudes, is stronger at high latitudes. This results in the production of very strong toroidal fields at high latitudes, which subsequently diffuse out to the SCZ giving rise to sunspot eruptions there. It may be noted that this difficulty has been faced by many modelers working with BL type dynamo models (Durney, 1997; Dikpati and Charbonneau, 1999, Kuker, Rüediger and Schultz, 2001).

It was proposed recently by Nandy and Choudhuri (2002) that a deep meridional flow penetrating below the tachocline can solve the above problem. In this scenario, the toroidal fields created at high latitudes are dragged down immediately by the penetrating flow (profile shown in Fig. 1, top-right) into the stable

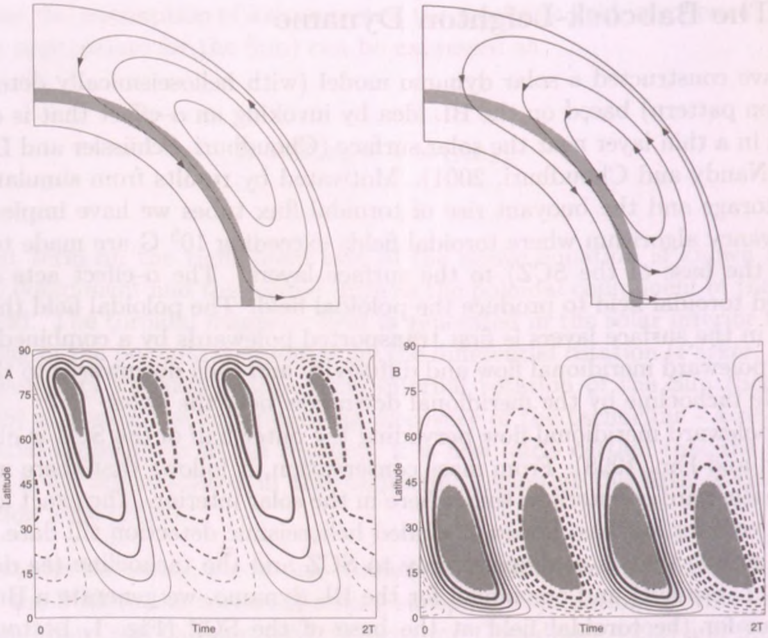

Figure 1: Top left shows a meridional circulation profile that is confined mainly to the SCZ and tachocline (shaded grey region). The arrows mark the direction of the flow. Bottom left shows the corresponding Butterfly diagram with solid lines denoting positive and dashed line negative toroidal field. Shaded regions mark the latitude of eruptions. Top right shows the profile of the penetrating meridional flow and bottom right shows the corresponding Butterfly diagram.

layers beneath the tachocline. A toroidal magnetic field becomes buoyant if it is above the base of the SCZ, but its buoyancy can be suppressed if it is put in the sub-adiabatically stratified upper radiative layer just beneath the tachocline. This belt of toroidal field cannot then diffuse out into the SCZ and can be subsequently brought towards low latitudes through this stable layer by the equatorward meridional counterflow. At low latitudes, the up-flow in the meridional circulation will bring up this toroidal field belt to the unstable SCZ, from where it can buoyantly erupt to form sunspots. Such a flow profile successfully reproduces the latitudinal distribution of sunspots as shown in the Butterfly diagram in Fig. 1, bottom-right.

3. Conclusion: Implications of a Deep Counterflow

According to conventional wisdom, the toroidal field that produces sunspots at low latitudes is generated at the low latitude itself. With the strong rotational shear in the high latitude tachocline, that no longer seems plausible. Our results show that the strong toroidal field is actually generated above 45° latitude, but it is allowed to come out into the SCZ and erupt, only at low latitudes. Such a penetrating flow advects the toroidal field through the low diffusivity region beneath the SCZ for a long time, thus generating very strong super-equipartition magnetic fields in excess of 10^5 G.

Our understanding of the complex plasma motions in the solar interior is still far from complete and it is not immediately obvious what physical mechanism can drive such a deeply penetrating meridional flow. However, recent simulations of solar convection shows that downward directed convective plumes (that presumably make up the meridional circulation) originating in the SCZ tends to penetrate into the stable region below and have a net equatorward motion inside the stable region (Miesch et al., 2000). These downward plumes are capable of pushing the magnetic field into the stable interior (Tobias et al., 2001).

Such a deep flow if it exists, would transport Lithium to depths (at higher temperatures) where this element would be destroyed by nuclear burning. It turns out that Lithium is destroyed at depths of about $\simeq 0.675 R_\odot$ while Beryllium gets destroyed at depths $\simeq 0.575 R_\odot$ (Brun, Turck-Chièze and Zahn, 1999). Our results with a deep flow show that the best solutions are obtained with a penetration depth of $0.6 R_\odot$ for the meridional flow. Lithium is actually found to be depleted in the solar surface with respect to its primordial abundance, while Beryllium remains un-depleted. Thus, such a penetrating flow may also help in explaining the Lithium depletion and its connection to angular momentum loss observed in stars at various phases of stellar evolution (Jones et al., 1997).

Inquiry into the dynamics of the tachocline and in what ways the rotational shear there interacts with magnetic fields have only just begun (Forgács-Dajka and Petrovay, 2002). Such studies, in conjunction with more sophisticated dynamo simulations, hold the promise of unveiling the exact means by which the Sun generates its magnetic cycle.

Acknowledgments

D.N. acknowledges financial support from NATO for his stay in Budapest during the workshop on turbulence and from NASA through SR&T grant NAG5-6110.

References

Babcock, H. W. 1961, ApJ, 133, 572

Braun, D. C., & Fan, Y. 1998, ApJ, 508, L105

Brun, A. S., Turck-Chièze, S., & Zahn, J.-P. 1999, ApJ, 525, 1032

Choudhuri, A. R., & Gilman, P. A. 1987, ApJ, 316, 788

Choudhuri, A. R., Schüssler M., & Dikpati M. 1995, A&A, 303, L29

D'Silva, S., & Choudhuri, A. R. 1993, A&A, 272, 621

Dikpati, M., & Charbonneau, P. 1999, ApJ, 518, 508

Dikpati, M., & Gilman, P. A. 2001, ApJ, 559, 428

Durney, B. R. 1997, ApJ, 486, 1065

Forgács-Dajka, E. & Petrovay, K. 2002, A&A, 389, 629

Jones et al. 1997, AJ, 114, 352

Küker, M., Rüdiger, G. & Schultz, M. 2001, A&A, 374, 301

Leighton, R.B. 1969, ApJ, 156, 1

Miesch et al. 2000, ApJ, 532, 593

Moreno-Insertis, F., Schüssler, M., & Ferriz Mas, A. 1992, A&A, 264, 686

Nandy, D., & Choudhuri, A. R. 2001, ApJ, 551, 576

Nandy, D., & Choudhuri, A. R. 2002, Science, 296, 1671

Parker, E. N. 1955, ApJ, 122, 293

Schou et al. 1998, ApJ, 505, 390

Tobias et al. 2001, ApJ, 549, 1183

WAVES AND INSTABILITIES OF PERIODICAL SHEAR FLOWS

Y. Zhugzhda
IZMIRAN, Troitsk, Russia
Astrophysickalishes Institut Potsdam, Potsdam, Germany
E-mail: `zhu@izmiran.rssi.ru`

Abstract

The exact analytical solution of the extended Rayleigh (ER) equation for the case of the periodical compressible shear flow is found. The dispersion relation of the problem is the infinite Hill determinant. It is found that sound waves in a shear flow have a dispersion and its velocity field contains a solenoidal part. Besides sound waves, new wave modes such as phonon, waveguide and vortex wave modes are revealed. The vortex mode is a singular solenoidal mode. Such modes are negative energy waves for which a dissipative instability is possible. The absolute phonon-vortex instability appears for Mach number $Ma \gtrsim 0.4$.

1. Introduction

The theory of spatially periodic incompressible flows is a topic of active research interest from the time of Kolmogorov, who proposed it as a simple model to study turbulence (see, Meshalkin & Sinai (1961)). For this reason the incompressible periodic flows is used to name Kolmogorov flows. The stability of one- and two-dimensional Kolmogorov flows were explored in very details by theoretical and experimental approach (Beaumont (1981); Bondarenko et al. (1979); Obuchov (1983); Takaoka (1989); Thess (1992); Brevdo et al. (1996)). To our knowledge compressible periodic shear flows have never been explored. This is not particularly surprising since the treatment of compressible flows is more severe problem due to interplay of different wave modes. One of basic methods of the exploration of periodic shear flows is based on Flouque theorem, which was used for the first time by Beaumont (1981). Besides considerable progress toward the understandings of the physics of shear flows has been achieved with the introduction of the concept of negative energy waves and the exploration of the plasma analogy Craik (1985); Ostrovskii et al. (1986); Fabricant & Stepanyants (1998).

The treatment of compressible shear flows has been performed for the first time in Zhugzhda & Stix (1994); Zhugzhda (1998); Zhugzhda. Flouque theorem makes possible to obtain an exact analytical solution for the case of parallel periodical shear flow. First, the method (Flouque theorem) will be outlined. Second, wave modes and instabilities of periodical shear flow will be described.

2. Basic equations

Let us consider an equilibrium atmosphere with vertical hot upflows and cold downflows. The equilibrium pressure p_0 is constant in the entire atmosphere, while the equilibrium values of the temperature T_0, density ρ_0 and vertical velocity $\vec{V} = (0,0,V)$ are arbitrary functions of x. All equilibrium variables are independent of the vertical coordinate z. The problem of linear waves in a structured atmosphere is reduced to the extended Rayleigh (ER) equation, which reads

$$\frac{d^2p}{dx^2} + \left[\frac{d\ln(c_0^2)}{dx} + \frac{2}{V_{ph}-V}\frac{dV}{dx}\right]\frac{dp}{dx} + \left[\frac{k_z^2(V_{ph}-V)^2}{c_0^2} - k_y^2 - k_z^2\right]p = 0, \quad (1)$$

where p is the amplitude of pressure fluctuations, c_0 is the sound speed, $V_{ph} = \omega/k_z$ is the phase velocity. In the limit of a uniform atmosphere, when $V(x) = \text{const}$ and $c_0(x) = \text{const}$, the equation is reduced to the standard dispersion relation for sound waves $\omega^2 = (k_z^2 + k_\perp^2)c_0^2$, where $k_\perp$ is the "horizontal" wavenumber. *In the general case of a structured atmosphere it is assumed that the wave amplitude is bounded at infinity* $x \to \infty$. This condition corresponds to the requirement $k_\perp^2 \geq 0$ for the case of a uniform atmosphere.

The consideration is restricted to the specific case of a periodical shear flow, when temperature, density and vertical velocity are periodic functions of x, with spatial period $2d$:

$$T_0(x+2d) = T_0(x), \; \rho_0(x+2d) = \rho_0(x), \; V(x+2d) = V(x). \quad (2)$$

In this special case, the ER equation (1) belongs to the class of equations with periodic coefficients. The treatment of such equations has been developed especially for the Mathieu and Hill equations, which often appear in physical problems Ince (1944). However, Eq.(1) is an extension of the Mathieu and Hill equations, and a more complicated algebra is needed to solve it.

Let us introduce the dimensionless variables

$$\xi = k_l x, \eta = k_l y, \zeta = k_l z, k_l = \frac{\pi}{2d}, \widetilde{k}_y = \frac{k_y}{k_l}, \widetilde{k}_z = \frac{k_z}{k_l}, \widetilde{\omega} = \frac{\omega}{k_l \widetilde{c}}, \widetilde{V} = \frac{V}{\widetilde{c}},$$

$$\widetilde{V}_{ph} = \frac{V_{ph}}{\widetilde{c}}, \; \widetilde{c}_0^2 = \frac{c_0^2}{\widetilde{c}^2}, \; \widetilde{p} = \frac{p}{p_0}, \; \widetilde{v}_x = \frac{v_x}{\widetilde{c}}, \; \widetilde{v}_z = \frac{v_z}{\widetilde{c}}, \; \widetilde{c}^2 = \langle c_0^2 \rangle, \quad (3)$$

where $\langle c_0^2 \rangle$ is the mean of the sound speed over the space period $2d$. The reason for the unusual definition of the lattice wavenumber k_l is that in this way the solutions of Eq.(1) is reduced to that form, which is used in the theory for the Mathieu and Hill equations Ince (1944).

To obtain an analytical solution of (1) the consideration is restricted to the case, when the x-dependence of the temperature and the flow velocity of the periodical shear flow are given by

$$\tilde{c}_0^2 = 1 + \delta \cos 2\xi, \quad \tilde{V} = V_m + Ma \cos 2\xi, V_m = Ma\, \delta^{-1}(1 - \sqrt{1 - \delta^2}) \tag{4}$$

where Ma is the Mach number. The velocity of the mean flow V_m is defined by the condition of a zero mean mass flux $< \rho_0 V >= 0$. In this case the equation (1) reads

$$A_1 \frac{d^2 p}{d\xi^2} + A_2 \frac{dp}{d\xi} + A_3 p = 0, \tag{5}$$

where

$$\begin{aligned}
A_1 &= a_1 + a_2 \cos 2\xi + a_3 \cos 4\xi, \ A_2 = b_1 \sin 2\xi + b_2 \sin 4\xi, \\
A_3 &= c_1 + c_2 \cos 2\xi + c_3 \cos 4\xi + c_4 \cos 6\xi, a_1 = V_D - 0.5\delta Ma, \\
a_2 &= \delta V_D - Ma, a_3 = -0.5\delta Ma, b_1 = -2(\delta V_D + 2Ma), \\
b_2 &= -\delta Ma, c_1 = V_D(V_D^2 + 1.5Ma^2)k_z^2 - a_1(k_y^2 + k_z^2), \\
c_2 &= -3Ma(V_D^2 + 0.25Ma^2)k_z^2 - a_2(k_y^2 + k_z^2), \\
c_3 &= 1.5V_D k_z^2 Ma^2 - a_3(k_y^2 + k_z^2), c_4 = -0.25Ma^3 k_z^2, V_D = V_{ph} - V_m.
\end{aligned} \tag{6}$$

The mean velocity V_m causes a Doppler shift of the frequency $\omega_D = \omega - k_z V_m$ in the laboratory frame. Here and in the following the tilde is omitted.

The general case of the oblique wave propagation with respect to the flow direction is considered. It is known from the theory of the differential equations with periodical coefficients (Ince 1944), that there are two kinds of bounded solutions of Eq.(5) with either period π $(n = 0)$ or 2π $(n = 1)$:

$$p = e^{ik_\perp \xi} \sum_{-\infty}^{\infty} C_{2m+n} e^{i(2m+n)\xi}, \quad n = 0, 1. \tag{7}$$

The coefficients C_{2m+n} are not arbitrary constants. The solution satisfies the equation (5) only for a special choice of the constants C_{2m+n}. After substitution of the solution (7) in the equation (5) and collecting the terms with the same powers of $\exp i\xi$, the equation is replaced by an expansion in terms of

$\exp i\xi$. Because the solution (7) has to satisfy the equation for all values of ξ, the coefficients of the equation expansion in powers of $\exp i\xi$ shall be equal to zero. This condition provides an infinite set of coupled linear algebraic equations in the coefficients C_{2m+n} of the solution (7). The set of linear algebraic equations has a non-trivial solution, when its determinant equals to zero. This determinant is known in the theory of the differential equations with periodical coefficients as Hill determinant, it is infinite. In the case under consideration the Hill determinant is a dispersion equation for hydrodynamic linear waves in a periodical shear flow. For the solution (7) with $n = 0$ the dispersion equation reads

$$D(\omega) = \begin{vmatrix} \vdots & \vdots & \vdots & \vdots & \vdots & \vdots & \vdots \\ \cdots & q_{-4} & l^{+}_{-2} & r_0 & s & 0 & \cdots \\ \cdots & l^{-}_{-4} & q_{-2} & l^{+}_{0} & r_2 & s & \cdots \\ \cdots & r_{-4} & l^{-}_{-2} & q_0 & l^{+}_{2} & r_4 & \cdots \\ \cdots & s & r_{-2} & l^{-}_{0} & q_2 & l^{+}_{4} & \cdots \\ \cdots & 0 & s & r_0 & l^{-}_{2} & q_4 & \cdots \\ \vdots & \vdots & \vdots & \vdots & \vdots & \vdots & \vdots \end{vmatrix} = 0, \tag{8}$$

where

$$\begin{gathered} k_{\perp,m} = m + k_{\perp}, q_m = -k^2_{\perp,m} a_1 + c_1, l^{\pm}_m = 0.5(-k^2_{\perp,m} a_2 \mp k_{\perp,m} b_1 + c_2), \\ r_m = 0.5(-k^2_{\perp,m} a_3 + k_{\perp,m} b_2 + c_3), s = 0.5 c_4, \\ m = 0, 2, 4 \ldots \text{ for } n = 0, m = 1, 3, 5 \ldots \text{ for } n = 1, \end{gathered} \tag{9}$$

and a_n, b_n, c_n are defined by Eq.(6). In fact the dispersion relation for $n = 1$ is reduced to (8) by the transformations $k_{\perp} \rightarrow k_{\perp} \pm 1$, which follows from the general solution (7). Thus, it is sufficient to explore one of them. The dispersion equations defined by Hill determinants are a polynomials of infinite degree in the variables ω, k_z, $k_{\perp}$. The infinite degree appears due to the infinite number of wave modes in the structured atmosphere. The Hill determinant has to be truncated to consider a finite number of the wave modes.

3. Wave modes

The results of the numerical solution of the truncated Hill determinant (8) are presented in Fig.1 as the (k, ω)-diagrams, where the total wavenumber is $k = (k^2_{\perp} + k^2_y + k^2_z)^{0.5}$. The diagrams are plotted for the Doppler shifted frequency

ω_D. The Doppler shift is small for small values of δ and Ma due to the small mean velocity V_m (6).

The acoustic mode is shown by solid line on (k,ω)-diagrams in Fig.1. The main distinctions between the sound mode in the periodical shear flow and the conventional one in the uniform media are the occurrences of wave dispersion and frequency gaps, where the propagation of waves is inhibited. The dispersion manifests itself as a distinction between the sound curve in the (k,ω)-diagrams of Fig.1 and the straight line. By this is meant that the phase speed of sound waves differs from the mean sound speed (3) as a result of dispersion. The deviation of the phase velocity from the sound speed increases with $k_\perp$. The dispersion appears due to the effects of both velocity and temperature variations in the shear flow. In the case of a transversal propagation of sound waves ($k_z = 0$), the (k,ω)-diagram shown in Fig.1a looks like the conventional Brillouin zone diagram well-known in solid state physics. To be more specific, the curve for the sound waves is not continuous due to avoided crossing with another wave mode, which in the case of crystal lattice is known as phonon mode. It comes as no surprise that the Brillouin diagram appears in the problem, since the shear flow is periodical one. The similarity of (k,ω)-diagram of Fig.1a to the conventional Brillouin zone diagrams appears due to the occurrence of an alternative acoustic-type modes of negative group velocity $\frac{d\omega}{dk} < 0$ and of a finite frequency for $k = 0$. To follow the crystal lattice analogy, this mode is called "phonon" wave mode. The avoided crossing of the sound and the "phonon" modes creates frequency

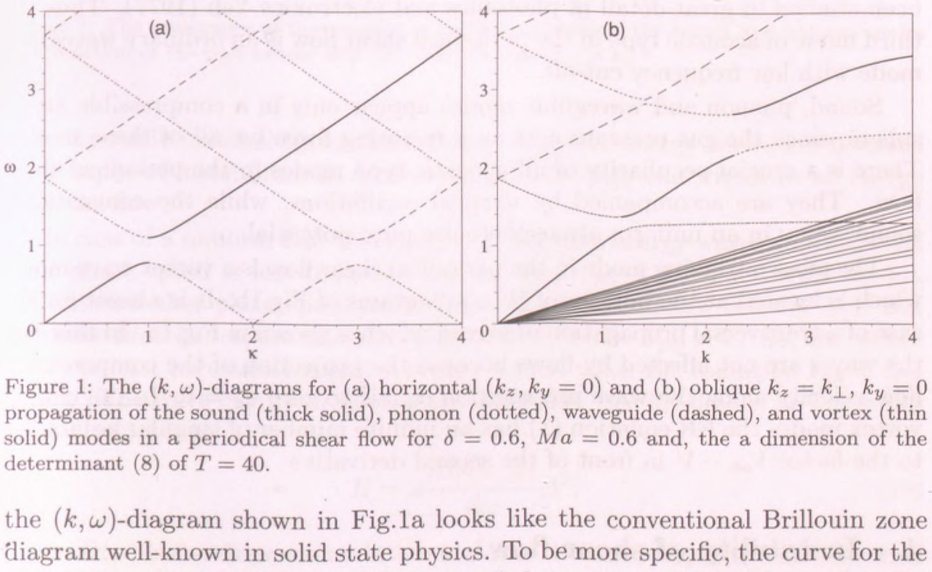

Figure 1: The (k,ω)-diagrams for (a) horizontal $(k_z, k_y = 0)$ and (b) oblique $k_z = k_\perp$, $k_y = 0$ propagation of the sound (thick solid), phonon (dotted), waveguide (dashed), and vortex (thin solid) modes in a periodical shear flow for $\delta = 0.6$, $Ma = 0.6$ and, the a dimension of the determinant (8) of $T = 40$.

gap, where the waves are evanescent. The frequency gap is akin to "forbidden energy gaps" in a crystal lattice. In the special case of a transversal propagation, the frequency gap appears as the result of only temperature variations. But the hydrodynamical "phonons" have nothing to do with the heat transfer. They can only transfer acoustic energy.

Even in the case of a transversal propagation the (k, ω)-diagram of Fig.1a differs from the conventional Brillouin zone, since there is one more acoustic-type mode, which is absent in one-dimensional lattice. The first of these modes starts at the same frequency $\omega = 2$, as the phonon mode, and almost parallel to the sound mode in the case of a transversal propagation $k_z = 0$. The nature of this acoustic mode becomes clear in the case of quasi-longitudinal propagation, when one-dimensional structured atmosphere can be considered as a multilayered waveguide for acoustic waves. The multilayered waveguides have been studied in great detail in photonics and electronics Yeh (1977). Thus the third mode of acoustic type in the periodical shear flow is an ordinary waveguide mode with low frequency cut-off.

Sound, phonon and waveguide modes appear only in a compressible atmosphere, since the gas pressure acts as a restoring force for all of these modes. There is a crucial peculiarity of all acoustic-type modes in the periodical shear flow. They are accompanied by vortical oscillations, while the conventional sound waves in an uniform atmosphere are pure potential.

The most intriguing mode in the periodical shear flow is a vortex wave mode, which is located at the bottom of (k, ω)-diagrams of Fig.1b. It is absent for the case of a transversal propagation of waves, which is shown in Fig.1a. In this case the waves are not affected by flows because the projection of the component of flow velocity along the wave propagation equals to zero $v_z = 0$. In the case of vortex modes the ER equation (1) has an infinite number of singular points due to the factor $V_{ph} - V$ in front of the second derivative.

4. Instability of shear flow

The instability of the periodical shear flow is defined completely by the negative energy waves. The concept of negative energy waves was first proposed for the waves in electron beams and since then it has been broadly used in plasma physics and electronics. Later the negative energy waves were introduced in hydrodynamics in connection with waves in shear flows (detailed discussion of the subject can be found in Craik (1985); Ostrovskii et al. (1986); Fabricant & Stepanyants (1998). The negative energy waves play a significant role in

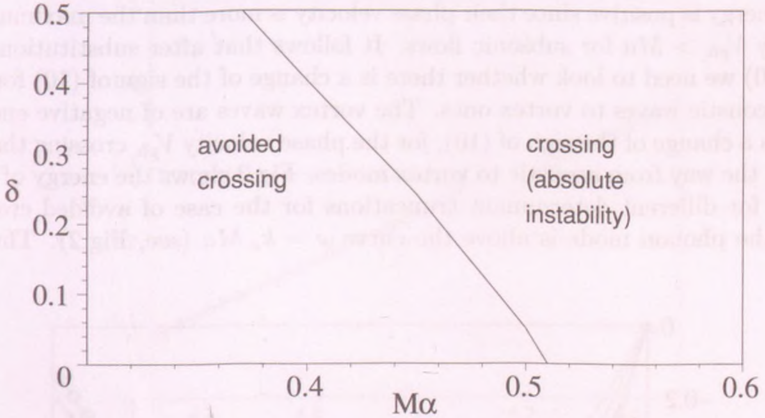

Figure 2: The occurrence of the crossing or avoided crossing of the vortex and phonon modes as a function of the parameters Ma and δ for the case $k_\perp = k_z$.

hydrodynamic instabilities of shear flows. Negative energy waves are involved in all kinds of instabilities in flows, because only they can withdraw an energy from the flow.

In case of a uniform flow $V(x) = const$, negative energy waves appear, when their phase speed is less than the flow velocity $V_{ph} < V$. For vortex modes, the dimensionless phase speed is less than the maximum flow velocity Ma. But the wave function covers also the parts of flow, where $V_{ph} > V$. So, the vortex waves are not necessarily negative energy waves, when the condition $V_{ph} < Ma$ is met. The wave energy in linear approximation (see for details in Ostrovskii et al. (1986)) is to

$$E = \omega \frac{\partial D(k,\,\omega)}{\partial \omega} A^2, \tag{10}$$

where $D(\omega)$ is the dispersion relation and A is the wave amplitude.The essential point is that the expression (10) is obtained as an expansion of the Langrangian in terms of a small wave amplitude A. The question arises whether the dispersion relation (8) can be substituted into (10). Except some factor, dispersion relations have to be the same no matter how they are obtained. Hence, the dispersion relation $D(\omega)$ (8) and one which stands in (10) differ by a factor, which can be either sign. Consequently,only the change of the sign of the wave energy can be found from (10) if the dispersion equation (8) is substituted. Actually, the true sign of the energy of acoustic and waveguide modes is known, namely, their energy is positive since their phase velocity is more than the maximum flow velocity $V_{ph} > Ma$ for subsonic flows. It follows that after substitution of (8) into (10) we need to look whether there is a change of the sign of (10) for going from acoustic waves to vortex ones. The vortex waves are of negative energy, if there is a change of the sign of (10), for the phase velocity V_{ph} crossing the value Ma on the way from acoustic to vortex modes. Fig.3 shows the energy of vortex modes for different determinant truncations for the case of avoided crossings, when the phonon mode is above the curve $\omega = k_z Ma$ (see, Fig.2). Thus, the vortex modes are waves of negative energy waves. The stability of the shear flow depends on whether there is a crossing of phonon and vortex modes. Fig.1b is plotted for $Ma = 0.6$ and $\delta = 0.6$, when there is a crossing. The crossing is replaced by an avoided crossing for smaller values of Ma and δ. In Fig.2 the dependence of the occurrence of crossing on the the choice of flow parameters. Fig.4 shows the part of (k, ω)-diagram of Fig.1b, where the coupling of phonon and vortex modes occurs. This is a typical (k, ω)-diagram for those cases, when there is a coupling between positive and negative energy waves. The frequency turns into a complex one beyond the point, where the phonon mode of positive energy and vortex mode of negative energy merge. The instability appears in

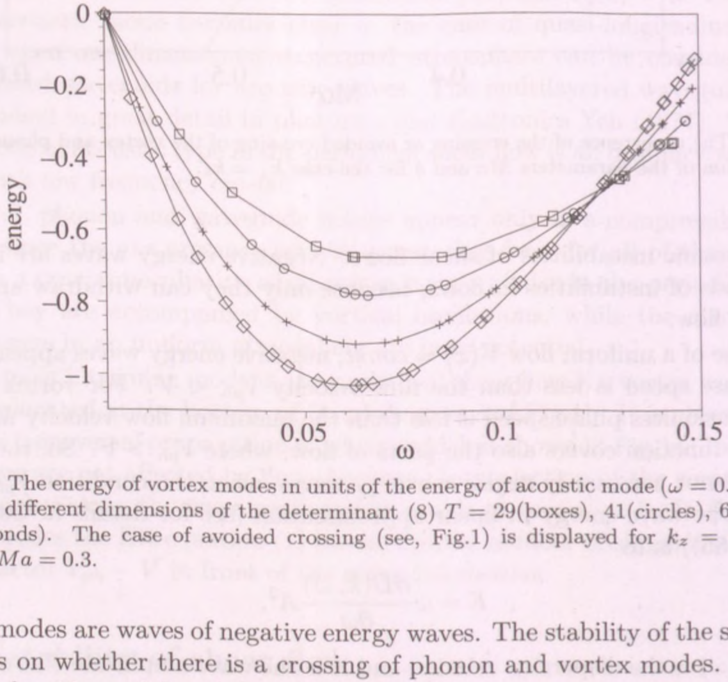

Figure 3: The energy of vortex modes in units of the energy of acoustic mode ($\omega = 0.71$), calculated for different dimensions of the determinant (8) $T = 29$(boxes), 41(circles), 61(crosses), 81(diamonds). The case of avoided crossing (see, Fig.1) is displayed for $k_z = k_\perp = 0.5$, $\delta = 0.3$, $Ma = 0.3$.

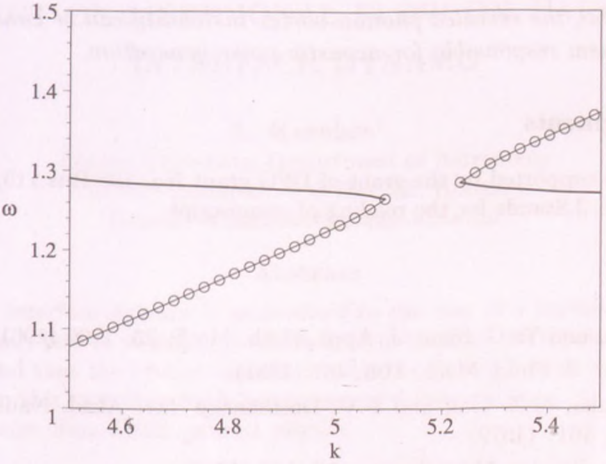

Figure 4: The coupling of the positive energy phonon mode and negative energy vortex mode is shown as an elargement of a small part of the (k, ω)-diagram of Fig.1b. Circles The parts of the mode curves, where the energy is negative, are marked by circles.

that range of wavenumbers between the two branch points of Fig.4, where the frequencies are complex. The instability of coupled waves of this kind is well known in electrodynamics Lifschitz (1981). The Kelvin-Helmholz instability is an example of the such an instability as well. The instabilities of this kind are called as absolute instabilities in order to distinguish them from the convective instabilities, which can just amplify waves. In the limit of an infinite determinant, the coupling of phonon and vortex modes dies out, and the range of unstable wavenumbers shrinks to zero. Thus, the phonon-vortex instability appears only in the case of truncated determinant which is akin to the viscous case. This instability produces pressure fluctuations along with vortical disturbances. *The phonon-vortex instability appears for subsonic flows*, as it can be seen in the diagram of Fig.2, where the region of the mode crossing is shown as a function of the flow parameters Ma and δ. The numerical simulations of a compressible flow Passot & Pouquet (1987) are in good agreement with our results. It is well known, that acoustic-kind instabilities appear in the case of supersonic flows Fabricant & Stepanyants (1998). As far as I know, subsonic acoustic-kind instabilities were not found in shear flows up to now. Up to the present the generation of acoustic noise in turbulent shear flows is considered in the frame of the Lighthill mechanism,which has nothing to do with instabilities of flows. So, *the revealed phonon-vortex instability can be considered as one more mechanism responsible for acoustic noise generation.*

Acknowledgments

The paper was supported by the grant of DFG grant No. 136 Rus 113/689/1-1. I am thankful to Dr. J.Staude for the reading of manuscript.

References

L.D. Meshalkin and Ya.G. Sinai, J. Appl. Math. Mech. **25**, 1700 (1961).

D.N. Beaumont, J. Fluid. Mech. **108**, 461 (1981).

N.F. Bondarenko, M.Z. Gak and F.V. Dolzhansky, Izv. Akad. Nauk (Fiz. Atmos. Okeana) **15**, 1017 (1979).

A.M. Obuchov, Russian Math.Surveys **38**, 113 (1983).

M. Takaoka, J.Phys.Soc.Japan **58**, 2223 (1989).

A. Thess, Phys.Fluid A **4**, 1385 (1992).

L. Brevdo, T.J. Bridges, Phil. Tran. Roy. Soc. London A **354**, 1027 (1996).

A.D.D. Craik, Wave Interactions and Fluid Flows (Cambridge University Press, Cambridge 1985).

L.A. Ostrovskii, S.A. Rybak, I.Sh. Tsimring, Uspechi Fizicheskich Nauk **150**, 417 (1986)

A.L Fabricant and Yu.A. Stepanyants, Propagation of Waves in Shear Flows World Scientific, London 1998).

Y.D. Zhugzhda and M. Stix, A& A **291**, 310 (1994).

Y.D. Zhugzhda, A& A **332**, 314 (1998).

Y.D. Zhugzhda, Physical Review D, 2002, (in press)

E.L. Ince, Ordinary Differential Equations (Dower Publications, New York 1944).

P. Yeh, A. Yariv and Chi-Shain Hong, J. Opt. Soc. Am. **67**, 423 (1977).

T. Passot and A. Pouquet, J. Fluid Mech. **181**, 441 (1987)

Lifschitz, L.P. Pitaevsky Physical kinetics, Amazon Press, 1981

EFFECT OF MERIDIONAL FLOW ON PARKER'S INTERFACE DYNAMO

A. Kerekes[1]
Eötvös University, Department of Astronomy
H-1518 Budapest, P.O.Box 32., Hungary
E-mail: `brunhilda@ludens.elte.hu`

Abstract

Parker's interface dynamo is generalized to the case of a transversal (i.e. meridional) flow of constant speed, limited to the high diffusivity volume. It is found that the Parker-Yoshimura sign law is much more difficult to violate in this case than for a homogeneous velocity field.

KEYWORDS: *S*un, MHD, plasma physics

1. Introduction

Solar activity phenomena are widely thought to originate in a dynamo mechanism operating on the weak large-scale solar magnetic field (see Petrovay, 2000 for a review). While the activity phenomena are related to strong concentrated fields like sunspots, these concentrations arise from the weak large-scale fields and after their decay their magnetic flux is returned to that field (e.g. Petrovay & van Driel-Gesztelyi, 1997). The rotational shear producing strong toroidal fields is concentrated below the bottom of the convective zone in the so-called tachocline layer (Kosovichev, 1996; Forgács-Dajka & Petrovay, 2002). The concentration of magnetic fields to this layer is partly aided by convective transport mechanisms such as pumping (cf. Petrovay, 1990).

2. Model

Parker's analytic, Cartesian interface dynamo model (Parker, 1993) has the assumption that the diffusivity varies by orders of magnitude across a surface. The α-effect operates on the high diffusivity side while the Ω-effect is limited to the low diffusivity side. Under these conditions a surface dynamo wave can be excited whose direction of propagation will be governed by the Parker-Yoshimura sign rule (Charbonneau & MacGregor, 1997; Markiel & Thomas, 1999). The

---

[1] Current address: Space & Atmosphere Research Center, Dept. of Applied Mathematics, University of Sheffield, Hicks Building, Hounsfield Rd, S3 7RH Sheffield, England (UK)

main advantage of the model is that in the case of high diffusivity contrast an arbitrary strong toroidal field can be generated in the shear layer. Instead of appealing to a dynamo wave, the field migration patterns can also be interpreted by meridional circulation (e.g. the recent Babcock-Leighton models, Wang & al., 1991; Dikpati & Gilman, 2001). The aim of the present work is to study how the operation of the Parker-dynamo may be influenced by the presence of a specifically prescribed flow representing the meridional circulation.
Following Parker, consider a Cartesian coordinate system with axes oriented in such a way that the positive x-, y-, and z-directions coincide with the directions of increasing θ, ϕ, and r. The $z = 0$ surface is the upper boundary of the shear layer (shear defined as $G = \mathrm{d}v_y/\mathrm{d}z$), and the lower boundary of the convective region. The parameters are homogenously distributed in each layer while they change discontinuously at the interface. The large-scale flow has the form $\mathbf{u}(z) = UH(z)\mathbf{e}_x + v_y(z)(1 - H(z))\mathbf{e}_y$, where H is the Heaviside function.

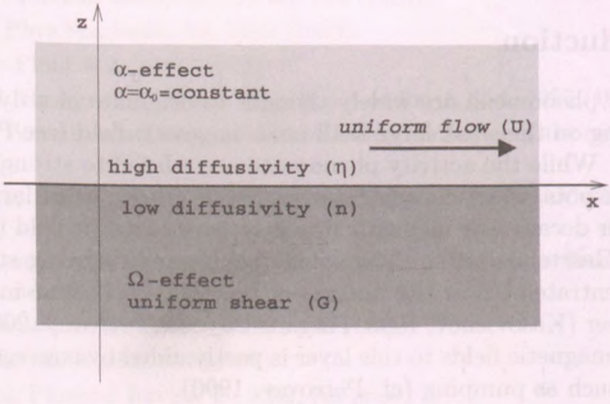

Figure 1: *Sketch of the model*

Represent the magnetic field $\mathbf{B}(x, z, t)$ as the sum of the poloidal and toroidal components: $\mathbf{B} = \mathbf{B}_P + B_y(x, z, t)\mathbf{e}_y$, where $\mathbf{B}_P = \nabla \times \mathbf{A}$ and $\mathbf{A} = A(x, z, t)\mathbf{e}_y$. Denote the toroidal field and vector potential by $B(x, z, t)$, $A(x, z, t)$ in $z > 0$, and by $b(x, z, t)$, $a(x, z, t)$ in $z < 0$. The mean-field dynamo equations are

$$[\partial_t - \eta(\partial_x^2 + \partial_z^2) + U\partial_x]B = 0\,, \tag{1}$$

$$[\partial_t - \eta(\partial_x^2 + \partial_z^2) + U\partial_x]A = \alpha_0 B\,, \tag{2}$$

at $z > 0$, and

$$[\partial_t - \eta(\partial_x^2 + \partial_z^2)]b = G\partial_x a\,, \tag{3}$$

$$[\partial_t - \eta(\partial_x^2 + \partial_z^2)]a = 0\,, \tag{4}$$

in $z < 0$. The boundary conditions in $z = 0$ are
$a = A$, $b = B$, $\partial_z a = \partial_z a$, $n\partial_z b = \eta\partial_z B$. The dynamo equations and the boundary conditions are linear, so the solutions are sought in the form

$$B = C\exp(\sigma t - Sz)\exp i(\omega t + kx - Qz)\,, \tag{5}$$

$$A = (D + Ez)\exp(\sigma t - Sz)\exp i(\omega t + kx - Qz)\,, \tag{6}$$

$$b = (L + Mz)\exp(\sigma t + sz)\exp i(\omega t + kx + qz)\,, \tag{7}$$

$$a = J\exp(\sigma t + sz)\exp i(\omega t + kx + qz)\,. \tag{8}$$

The corresponding dispersion relation reads as

$$\begin{aligned}
&-Z^8(\mu^2-1)^2 - 2Z^6(\mu^2-1)^2(\mu^2-1-iR)\\
&-Z^4[(1-3\mu^2+\mu^4)(\mu^2-1-iR)^2 - (1/2)i(1+\mu^2)\mu^2 N]\\
&+Z^2\mu^2[(\mu^2-1-iR)^3 + (1/2)i(1+\mu^2)(\mu^2-1-iR)N]\\
&+(1/16)\mu^4 N^2 = 0\,,
\end{aligned} \tag{9}$$

where $Z^2 = \beta + i(\nu + R)$, $\nu = \omega/\eta k$ is the dimensionless frequency, $\beta - 1 = \sigma/\eta k^2$ is the dimensionless growth rate, $R = U/\eta k$ is the Reynolds number, $N = \alpha_0 G/\eta^3 k^2$ is the dynamo number, and $\mu^2 = n/\eta$ is the diffusivity contrast. The complex dispersion equation provides two relations between the four quantities ν, β, N, and R so that ν and R can be expressed in terms of N and R. Instead of examining the general case (where μ^2 is arbitrary), it is expedient to consider the limiting case of small μ^2, which can be relevant to the Sun.

3. Limiting case, $\mu^2 \ll 1$

Consider the limit $\mu^2 \to 0$ while $\tilde{N} = \mu^2 N$ remains finite. For unstable modes $\beta - 1 > 0$, so assume that $\mu^2 \ll 1$. The applicability of the approximation is restricted to a limited range in R, where R_{min} and R_{max} can be determined by the condition $\beta(R) \gg \mu^2$.

In this case the real and imaginary parts of the dispersion relation are

$$\begin{aligned}
&(\nu+R)^4 - 2R(\nu+R)^3 - (\nu+R)^2(6\beta^2 - 6\beta + 1 - R^2)\\
&(\nu+R)[2\beta R(3\beta-2) + \tilde{N}(\beta - 1/2)]
\end{aligned}$$

$$+\beta^2(\beta-1)^2-\beta R(\beta R+(1/2)\tilde{N})-(1/16)\tilde{N}^2=0\,, \tag{10}$$

and

$$[(\nu+R)^2-\beta(\beta-1)-(\nu+R)R][\tilde{N}-8(\nu+R)(\beta-1/2)+4\beta R]=0\,. \tag{11}$$

From the imaginary part it is clear that either

$$\nu=(1/2)[-R\pm(R^2+4\beta(\beta-1))^{1/2}]\,, \tag{12}$$

or

$$\tilde{N}=8(\nu+R)(\beta-1/2)-4\beta R\,. \tag{13}$$

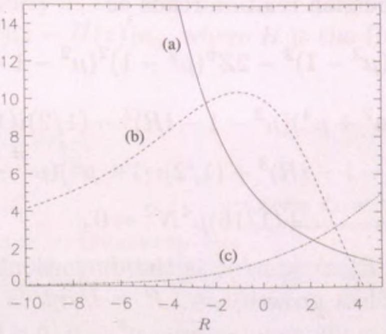

Figure 2: *Dynamo wave period* $P=2\pi/|\nu|$ *(a), dimensionless phase speed* $-\nu$ *(b), and growth rate* $\beta-1$ *(c), as functions of the flow speed in the limit of small* μ^2*, where* $\mu^2=0.01$ *(diffusivity contrast), and* $\tilde{N}=-12\sqrt{2}$ *(dynamo number).*

For the dimensionless growth rate we have the implicit relation

$$\tilde{N}=-2R\pm4[R^2+4\beta(\beta-1)]^{1/2}(\beta-1/2)\,, \tag{14}$$

where for $\tilde{N}>0$ the + sign, while for $\tilde{N}<0$ the − sign corresponds to growing modes.

4. Conclusions

The analysis of the equations above indicates that Parker-Yoshimura sign rule holds unconditionally, so in the limit considered here an anti-parallel flow cannot reverse the direction of propagation of the dynamo wave.

References

Charbonneau, P. & MacGregor, K. B. 1997, *ApJ*, 486, 484

Dikpati, M. & Gilman, P. A. 2001, *ApJ*, 559, 428

Forgács-Dajka, E. & Petrovay, K. 2002, *A&A*, 383, 629

Kosovichev, A. G. 1996, *ApJ*, 469, 61

Markiel, J. A. & Thomas, J. H. 1999, *ApJ*, 523, 827

Parker, E. N. 1993, *ApJ*, 408, 707

Petrovay, K. 1990, *ApJ*, 362, 722

Petrovay, K. & van Driel-Gesztelyi, L. 1997, *Sol. Phys.*, 176, 249

Petrovay, K. 2000, ESA SP-493 3-14

Wang, Y. M. et al. 1991, *ApJ*, 383, 431

A NEW MODEL FOR THE LOWER OVERSHOOT LAYER IN THE SUN

D. Marik[1] and K. Petrovay[2]
Eötvös University, Department of Astronomy
H-1518 Budapest, P.O.Box 32., Hungary
E-mail: [1]`D.Marik@astro.elte.hu`, [2]`K.Petrovay@astro.elte.hu`

Abstract

We present a model for the lower overshoot layer of the Sun, based on the realistic solar stratification, without the use of a "mixing-length" parameter, by solving the system of Reynolds momentum equations using the closure formalism of Canuto & Dubovikov (1997, 1998). A fixed value of velocity anisotropy is assumed, and the local convection model is assumed to be valid for the convectively unstable layer. In accordance with seismic constraints, overshoot (defined as the amount by which the convectively mixed zone extends beyond its boundary in local theory) is found to be as low as about 6 percent of the pressure scale height, and it is not bounded by a discontinuity from below.

KEYWORDS: *Sun, MHD, plasma physics*

1. Introduction

The most promising way to model the overshooting layer is the Reynolds stress method, based on the well known Reynolds momentum hierarchy of the hydrodynamical equations for a turbulent medium. Our aim in such a model is to determine the radial distribution of the turbulent kinetic energy k, the mean square relative temperature fluctuation q, the normalized energy flux J and the energy dissipation rate ε under the convectively unstable region.

The Reynolds moment equations for k, q and J were solved for the lower overshoot layer by Unno & Kondo (1989), Xiong & Chen (1992), and Xiong & Deng (2001), resulting in significant non-adiabatic overshoot. However, in those calculations the mixing length l was treated as a free parameter, arbitrarily set to be equal to H_P. The use of an equation for ε to get rid of the free parameter was suggested by Canuto (1993) and it has been applied in a simplified k–ε model by Petrovay (1998).

In this paper we will employ a formalism basically identical to that of Canuto & Dubovikov (1997, 1998). By solving the momentum equations for the realistic solar stratification, here we present the first model of the lower overshoot layer without an assumed mixing length parameter.

2. Equations and closure

We will use the following notations. Any variable f is split into a mean and a fluctuating part as $f = \overline{f} + f'$. The velocity $\mathbf{v}$ has only a fluctuating part. We assume plane parallel geometry and the depth z is measured from $\Delta\nabla = 0$, so the gravity acceleration g is positive. Beside ϱ for density, we also introduce the notations $q = \overline{(T'/T)^2}$, $J = \overline{w(T'/T)}$, $w = v_z$, $k = \overline{v^2}/2 = \overline{w^2}/f_a$ where f_a is an anisotropy parameter.

We make the following assumptions:

- $\varrho'/\varrho \ll 1$
- The Reynolds number $Re \gg 1$, while the Prandtl number $\nu/\chi \ll 1$
- The extent of the overshoot layer $d \ll H_P$, where H_P is the pressure scale height.
- The turbulent flow field is characterized by a mild and fixed value of the anisotropy $f_a \in \mathcal{O}(1)$. This aasumption is made for simplicity only.

With these assumptions we can use the Boussinesq approximation $\varrho'/\varrho = -\delta_P \cdot (T'/T)$ where δ_P is an order of unity factor ($\delta_P = 1$ for full ionization). Following standard practice, we will also neglect the $\overline{\mathbf{v}\nabla P'}$ term in the equation for k.

The detailed derivation of the Reynolds momentum equations was given by many authors (Xiong, 1980; Canuto, 1993; Grossman et al., 1993). With the assumptions and notations mentioned above, and after customary dimensional modelling of some terms, they read

$$\partial_t k = -\partial_z F_k + \delta_p g J - \varepsilon \tag{1}$$

$$\begin{aligned}\partial_t J = -\partial_z F_J - C_{qJ}\delta_p g q \quad &+ C_{kJ} f_a \frac{\Delta\nabla}{H_P} k - \frac{J}{\tau_{p\theta}} \\ &+ \frac{1}{2}\frac{\chi}{T}\partial_z^2 (JT)\end{aligned} \tag{2}$$

$$\partial_t q = -\partial_z F_q + 2\frac{\Delta\nabla}{H_P} J - \frac{q}{\tau_p} + \frac{1}{2}\frac{\chi}{T^2}\partial_z^2 (qT^2) \tag{3}$$

$$\partial_t \varepsilon = -\partial_z F_\varepsilon + C_{J\varepsilon}\delta_p g \frac{\varepsilon}{k} J - C_\varepsilon \frac{\varepsilon^2}{k} \tag{4}$$

where the non-local fluxes are

$$\begin{array}{ll} F_k = \overline{wv^2/2}, & F_q = \overline{w(T'/T)^2} \\ F_J = \overline{w^2T'/T}, & F_\varepsilon = \overline{w\varepsilon_l} \end{array} \tag{5}$$

ε_l being the local dissipation rate. For the coefficients we use the following values: $C_{kJ} = 1.0$, $C_{qJ} = 1$, $f_a = 1$, $C_\varepsilon = 1.92$, $C_{J\varepsilon} = 1.44$, $\delta_P = 1$. In order to close the system we used the closure assumption of Canuto & Dubovikov (1997). Finally, the timescales $\tau_{p\theta}$ and τ_p were calculated using formulae (34) of Canuto & Dubovikov (1998).

3. Numerical solution

A relaxation method was used to solve this nonlinear, coupled system of differential equations. The condition of flux equilibrium ($F_c + F_k + F_r = F_\odot = \mathrm{const}$) must also be coupled to the problem, where $F_\odot$ is the total spolar flux, F_c is the total convective heat flux, F_k is the kinetic energy flux, and F_r is the radiative flux. The iteration process of relaxation is repeated until it converges to a stationary state.

4. Results

Our stationary solution is presented in Fig 1. The turbulent length and time scales in Fig. 1 b are defined as $l = k^{3/2}/\varepsilon$ and $\tau = k/\varepsilon$. The thickness of the overshoot layer is small, below six percent of H_P, and the $\Delta\nabla$ curve does not show a particularly sharp discontinuity. This is compatible with the available helioseismic evidence (Basu & Antia, 2001). It must be stressed that, by design, our models can only yield the extent of overshoot *in the helioseismic sense* (i.e. the amount by which the convective zone extends beyond its boundary in local theory).

It is interesting to note that the "mixing length" l is found to decrease continuously towards the bottom of the overshoot layer. This underlines the incorrectness of the assumption l =const. in those models that use a free length parameter.

Yet we do not claim that our model is the final word concerning overshoot in the Sun. Further work is also needed to include a consistent treatment of the anisotropy (Petrovay (1992)) and to extend the domain of calculation to the unstable layer.

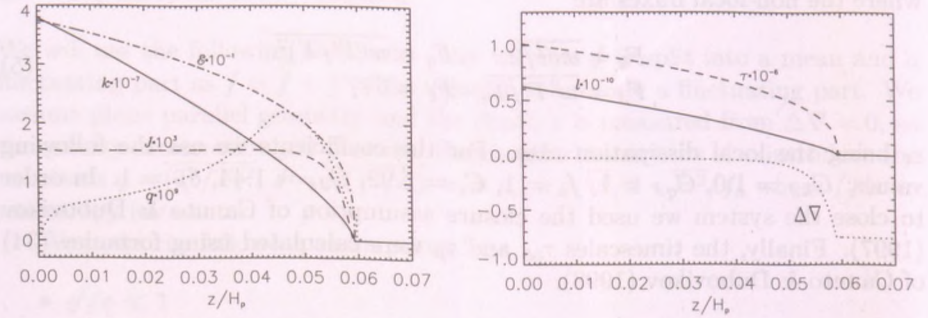

Figure 1: Left is the distribution of k, q, J, and ε vs. depth below the convectively unstable layer. Right is the distribution of l, τ and $\Delta\nabla$. All dimensional variable are given in CGS units.

Acknowledgments

This work was funded by the OTKA under grants no. T032462 and T034998.

References

Basu, S., & Antia, H. M. 2001, *Monthly Notices Roy. Astron. Soc.* , 324, 498

Canuto, V. M. 1993, *Astrophys. J.* , 416, 331

Canuto, V. M., & Dubovikov, M. 1997, *Astrophys. J.* , 484, L161

—. 1998, *Astrophys. J.* , 493, 834

Grossman, S. A., Narayan, R., & Arnett, D. 1993, *Astrophys. J.* , 407, 284

Kupka, F. 1999, *Astrophys. J.* , 526, L45

Petrovay, K. 1990, *Astrophys. J.* , 899, 722

Petrovay, K. 1992, Geophys. Astrophys. Fluid Dyn., 65, 183

Petrovay, K. 1998, IAU Symp. 185, 121–122

Petrovay, K. 2000, ESA SP-463, 3

Unno, W., & Kondo, M. 1989, *PASJ* , 41, 197

Xiong, D. R. 1980, Chinese Astron. Astrophys., 4, 234

Xiong, D. R., & Chen, Q. L. 1992, *Astron. Astrophys.* , 254, 362

Xiong, D. R., & Deng, L. 2001, *Monthly Notices Roy. Astron. Soc.* , 327, 1137

PART TWO

TURBULENCE IN THE CONVECTIVE ZONE AND PHOTOSPHERE

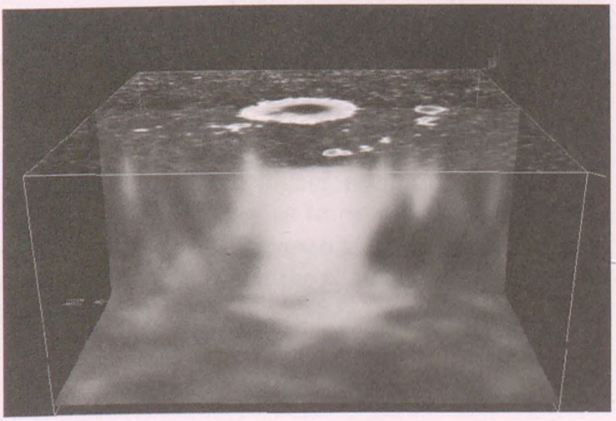

PART TWO

TURBULENCE IN THE CONVECTIVE ZONE AND PHOTOSPHERE

TURBULENCE IN ROTATING CONVECTION

Kwing L. Chan
The Hong Kong University of Science and Technology,
Department of Mathematics
Clear Water Bay, Kowloon, Hong Kong, China
E-mail: `maklchan@ust.hk`

Abstract

Rotation plays vital roles in a great number of solar phenomena. Here we discuss results of a large eddy simulation study that illustrates the behavior of convective turbulence spanning over a wide range of Coriolis numbers.

KEYWORDS: *Sun, rotation, convection, turbulence*

1. Introduction

Rotation has dominant effect on the convective turbulence in most of the solar convection zone. So far, a comprehensive understanding of the effect has not been achieved, and due to the complexity of the problem, realistic progress has to rely on numerical simulation. In an earlier paper (Chan, 2001), we have reported on an f-box study that covered the parameter space with a rather dense distribution of cases, so that trends can be clearly identified in the changing behavior of convection as the Coriolis number (Co = 1/ Rossby number) increases from 0 to some moderate value (≈ 7). For a review of the literature, the readers are referred to the paper by Brummell et al. (1996).

In the last couple of years, we have made higher resolution calculations ($70 \times 70 \times 80$ *vs* $35 \times 35 \times 39$ meshes) that allow us to extend the range of Co to higher values (since the sizes of large eddies decrease with increasing Co; see later discussion). Here the discussion is focused on the changing behavior of the turbulence across the different values of Co (≈ 0 to 15.6); the latitude is fixed at 22.5°.

2. The Model

A 'f-box' is a three-dimensional, rectangular, horizontally periodic, region that approximates a small piece of the global rotating convection zone. In this region, the angle between the rotation vector and the vertical direction is considered to be constant (the colatitude). In our Cartesian system, the x-, y-, z- axes are north-to-south, west-to-east, and radially outward, respectively (a right-handed system). The gas is ideal and the total stratification is about 5 pressure scale heights. The units are chosen so that the total depth, the pressure, density, and pressure at the top are all equal to 1 (in these units, sound speed = $\sqrt{\gamma} \approx 1.29$). The top of the convection zone is at the height 0.95, above which lies a marginally stable layer to soften the impact of the turbulence with the upper boundary. Further details of the model can be found in Chan's paper.

In this short article, we consider eight cases which have rotation rates Ω sequentially chosen at 0, 1/8, 1/4, 1/2, 1, 3/2, 2, and 3. Correspondingly, the Coriolis number, defined to be $\Omega \int dz / \int v'' dz$ where v'' is the rms velocity (with contribution of the mean already subtracted), takes on the approximate values 0, 0.7, 1.3, 2.6, 5.4, 8.3, 11.1, and 15.6. The resolution may not be sufficient for the fastest rotating case, but we include it here for comparison.

3. Dependence of the Turbulence on Rotation Rate

3.1. Flow patterns

Figure 1 shows horizontal cuts of instances of the vertical velocity field v_z at a number of depths for the different cases. The dark lanes show downflow regions. Roll structures are prominent, and there is a transition in the roll alignment from north-south to west-east between $\Omega = 1/8$ and $1/4$. The east-west alignment can be explained by the linear analysis of Hathaway et al. (1979), and the transition to the north-south alignment can be understood as the growing dominance of the Taylor-Proudman effect at higher Co. The separation of the downflow lanes decreases with increasing Co.

Figure 2 shows the vertical component of the vorticity $\zeta'_z = (\vec{\nabla} \times \vec{v}')_z$. Note that $()'$ denotes that the fluctuating quantity already has the mean subtracted. Both positive and negative vorticities concentrate along the downflow lanes, but the positive kind is more prominent. Figure 3 shows the vertical contribution to the helicity, $v_z \zeta'_z$. This part of the helicity also shows a tendency to concentrate in the downflow lanes, but its distribution is more spotty than the vertical vorticity. The spots are primarily negative and prominent only near the top of the convection zone.

Figure 4 illustrates that the rolls are tilted from the horizontal direction. The roll axes are more or less in alignment with the rotation vector. Before the stream lines are generated, the horizontal mean flows have been subtracted from the velocity field.

3.2. Statistics of the velocity field

Figures 5 and 6 show the horizontal and temporal mean of the meridional (north-south) and zonal (west-east) velocities, respectively. For small Co, the mean velocities have shear-like distributions. As Co gets larger, the shear region shrinks towards the top. The senses of the shears below the top of the convection zone are negative (velocities dropping outward). The depth extent of the shear region is related to the local Coriolis number ($\equiv \Omega H_p/v''$ where H_p is the local pressure scale height) whose distributions are plotted in Figure 7. The shears are confined to regions with the local Coriolis number below 1. The vertical averaging of the local Coriolis number defined here yields the values 0, 0.19, 0.35, 0.73, 1.6, 2.5, 3.4, 4.6 for the eight sequential cases. They are different from the Co defined earlier; there is arbitrariness in the choice of the characteristic velocity and length scales.

The symmetric Reynolds stress tensor contains six independent components. The diagonal ones are the mean square velocities, and the off-diagonal ones are covariances of different velocity components. Dynamically the diagonal stress components act as turbulence pressure along different directions, and the off-diagonal ones produce momentum transport. One interesting result in the f-box configuration is that the mean zonal flow is driven only by the vertical-meridional component of the Reynolds stress; components that carry the zonal momentum do not participate in the averaged momentum balance. Figure 8 shows the distributions of the rms vertical velocity. Higher rotation rates tend to suppress this component of velocity. Figure 9 shows the rms meridional velocity, the rms zonal velocity behaves similarly (except in the fastest rotating case whose results may not be reliable).

Figure 10 shows the correlation coefficient of the two horizontal velocities (remember that the means have been subtracted). Between the Co values 0.7 and 2.6, there is a change of sign in the correlation, almost at all depths. At the Co value 1.3, the situation is transitional. Figure 11 shows the correlation coefficient of the vertical and meridional velocity fluctuations. Note the general presence of positive peaks near the top of the convection zone in all of distributions; they are responsible for producing the negative dips in the zonal velocity near the top, through the meridional momentum equation. Figure 12 shows the correlation of the vertical and zonal velocity fluctuations. Though negative (as expected) when the Co is small, the correlation drops in magnitude when Co gets large, and eventually regions of positive correlation show up.

4. Summary

Results of the higher resolution calculations presented here are generally in agreement with those obtained by the low resolution calculations presented in the earlier paper. The higher resolution allows us to view the flow fields more clearly. That also makes possible the pushing of Co to higher values, further consequences of which are to be explored in a later paper.

Acknowledgments

I would like to thank the SOC/LOC of this NATO Workshop for the support of local expenses. The research is supported by the RGC of Hong Kong.

References

Brummell, N. H., Hurlburt, N. E., & Toomre, J. 1996, *Astrophys. J.* , 473, 494
Chan, K. L. 2001, *Astrophys. J.* , 548, 1102
Hatherway, D. H., Gilman, P. A., & Toomre, J. 1979, Geophys. Astrophys. Fluid Dyn., 13, 289

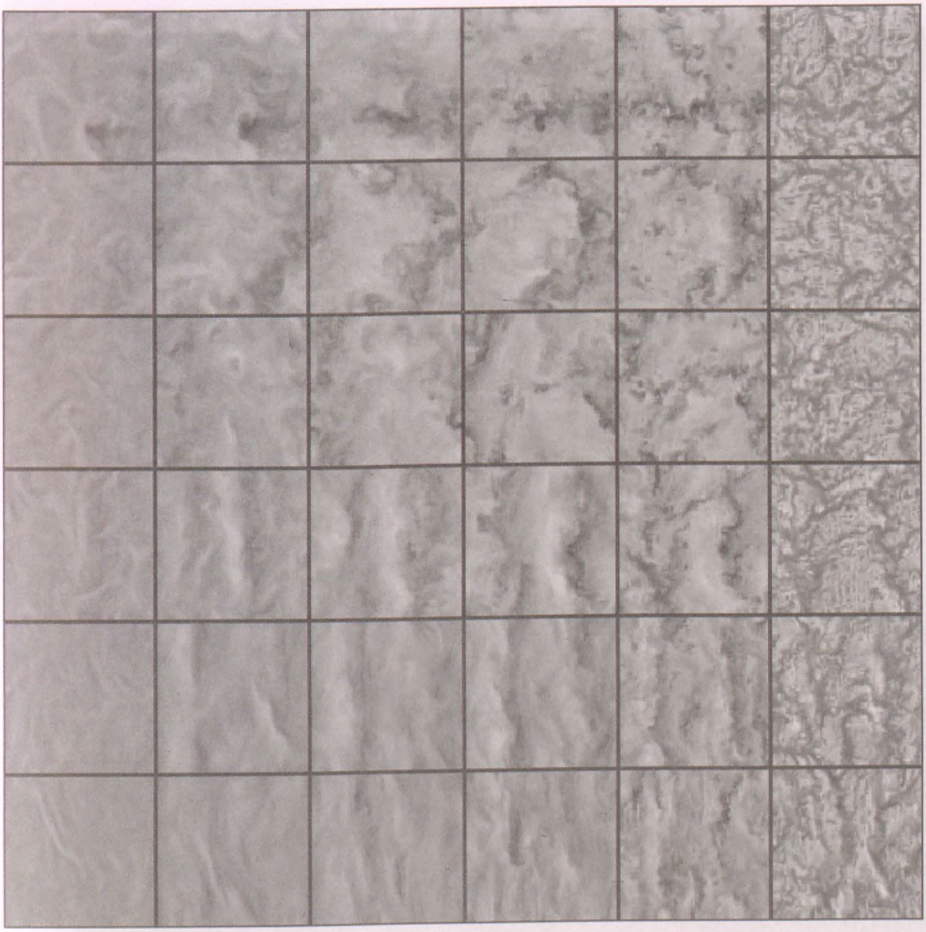

Figure 1: From top to bottom, the rows show instances of the vertical velocity field for the cases with $\Omega = 1/8$, $1/4$, $1/2$, 1, 2, 3, respectively. Each column shows horizontal cuts of the fields at a fixed depth. From left to right, the depths go from deeper to shallower. The vertical and horizontal directions represent the north-south and east-west orientations, respectively.

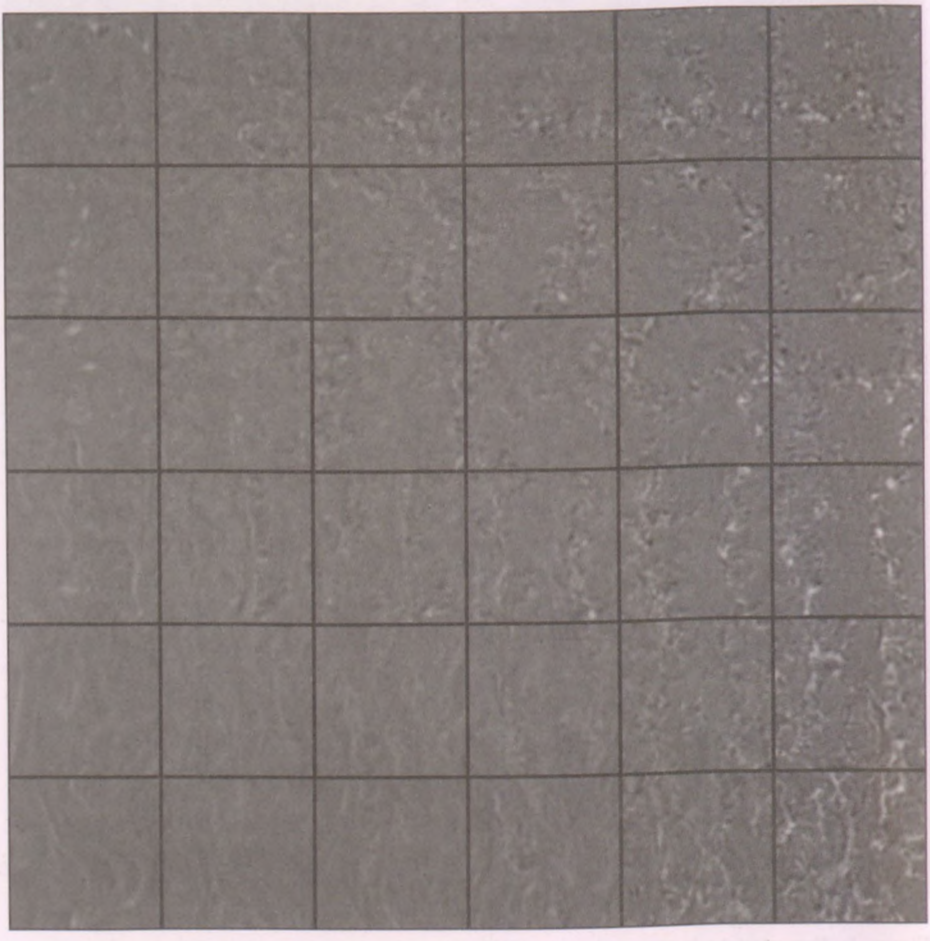

Figure 2: Horizontal cuts of the vertical vorticity field (i.e. $(\vec{\nabla} \times \vec{v}')_z$) for the same instances and cases as those in Figure 1.

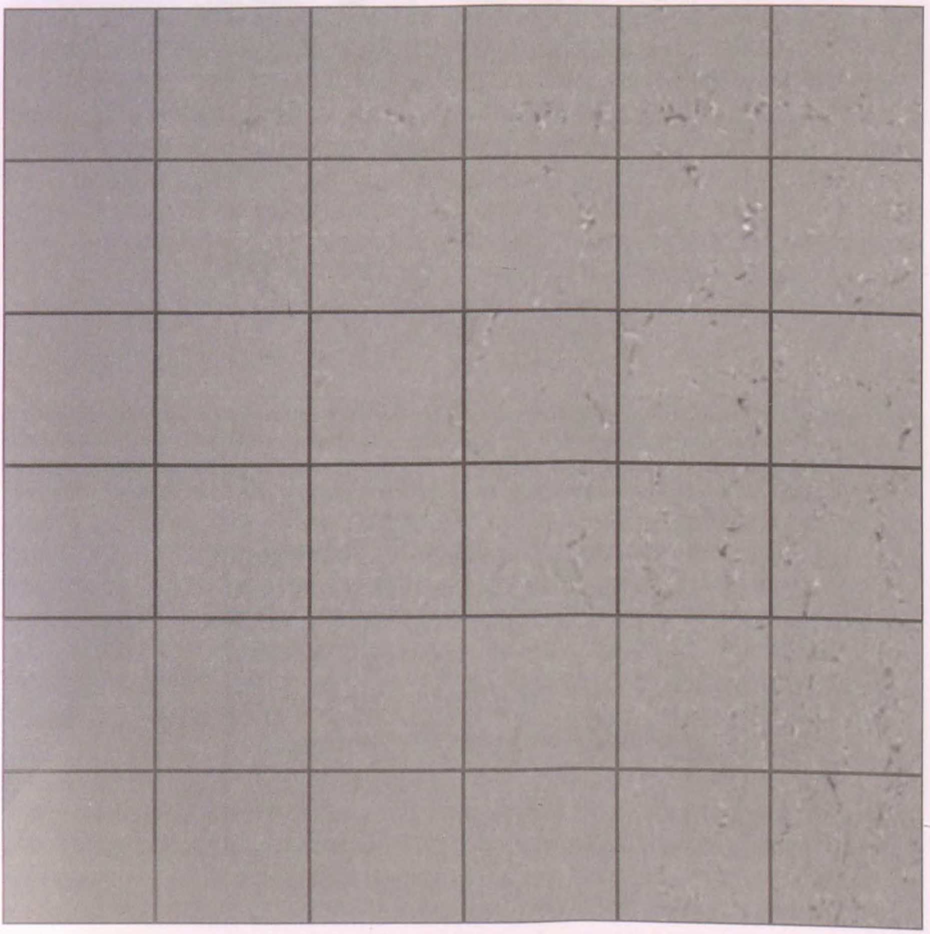

Figure 3: Horizontal cuts of the vertical contribution to the helicity field (i.e. $v_z(\vec{\nabla} \times \vec{v}')_z$) for the same instances and cases as those in Figure 1.

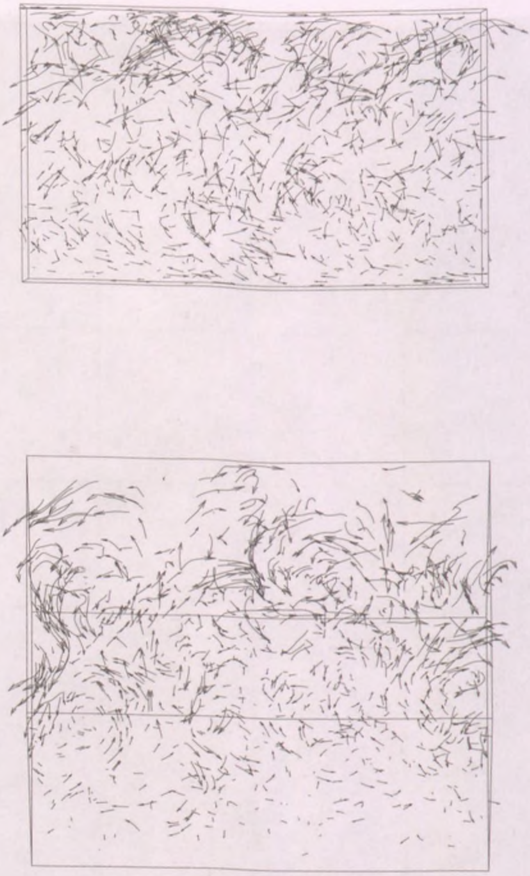

Figure 4: Streamlines of the turbulence velocity field (mean flows eliminated) in an instance of the $\Omega = 2$ case. *Upper panel*: A view taken from the west side of the box towards east. *Lower panel*: A view taken from the south side and 22° below the horizon, towards the north and at an angle 68° from the vertical direction; the projected streamlines indicate circular roll motions.

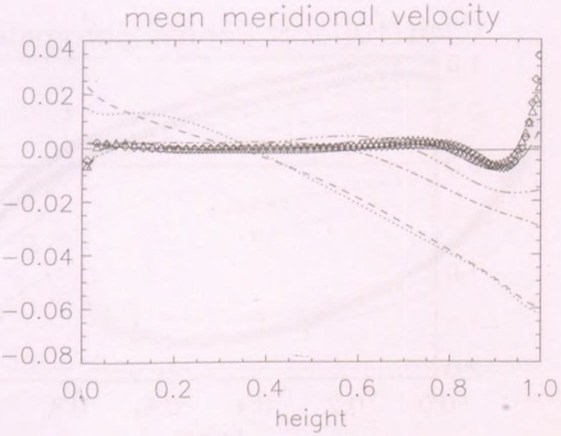

Figure 5: Vertical distributions (profiles) of the horizontally and temporally averaged mean meridional flow. The $\Omega = 0$, 1/8, 1/4, 1/2, 1, 3/2, 2, 3 cases are represented by the solid, dotted, short dashed, dot-dashed, triple-dot-dashed, long dashed lines, the triangles, and rhombus, respectively. All later figures use the same symbols to identify the cases.

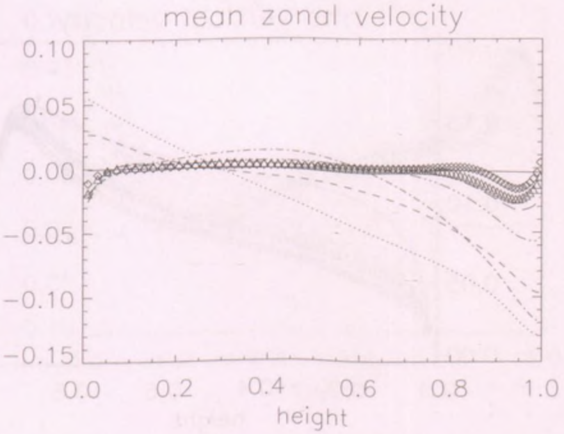

Figure 6: Profiles of the horizontally and temporally averaged mean zonal flow. All show dips near the top of the convection zone.

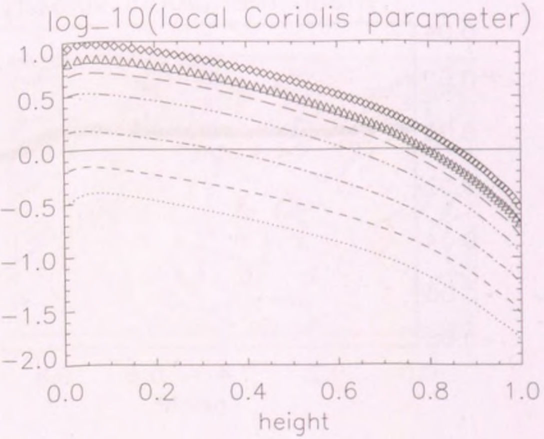

Figure 7: log_{10} of the local Coriolis number, defined as $\Omega H_p/v''$. The characteristic length scale is chosen to be the local pressure height H_p.

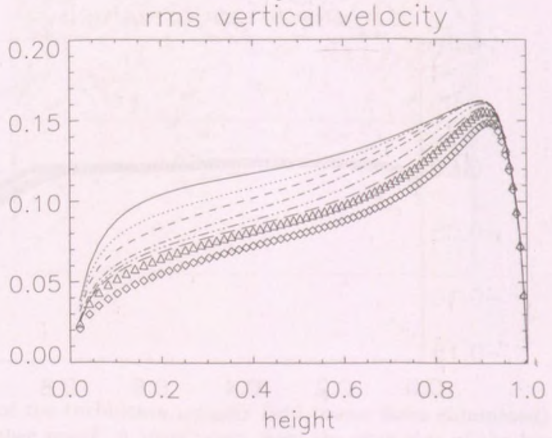

Figure 8: Profiles of the rms vertical velocity. Rotation tends to suppress this velocity.

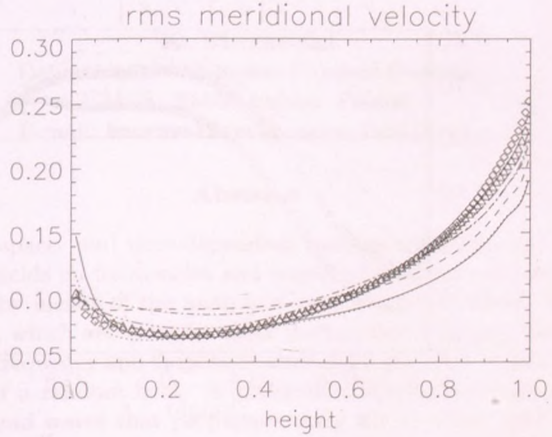

Figure 9: Profiles of the rms meridional velocity.

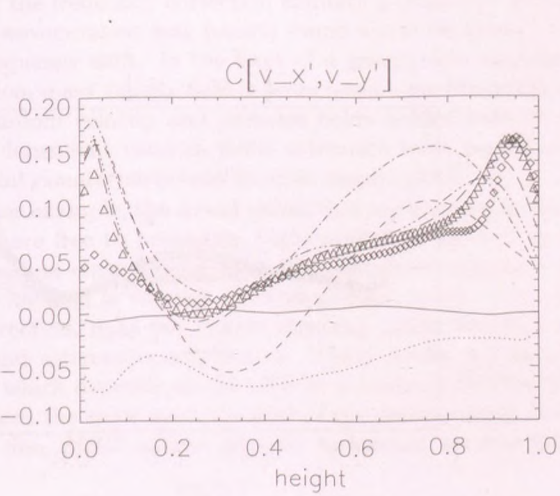

Figure 10: Profiles of the correlation coefficient of the two horizontal velocity fluctuations. There is a change of sign between the distributions for the low and the high Co values.

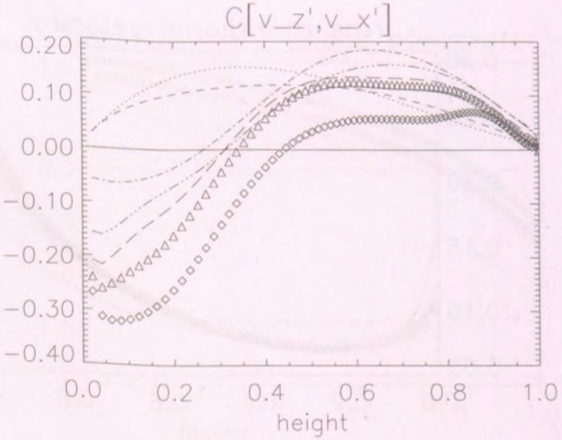

Figure 11: Profiles of the correlation coefficient of the vertical and meridional velocity fluctuations. Note the general presence of a positive peak in the upper region of the convection zone.

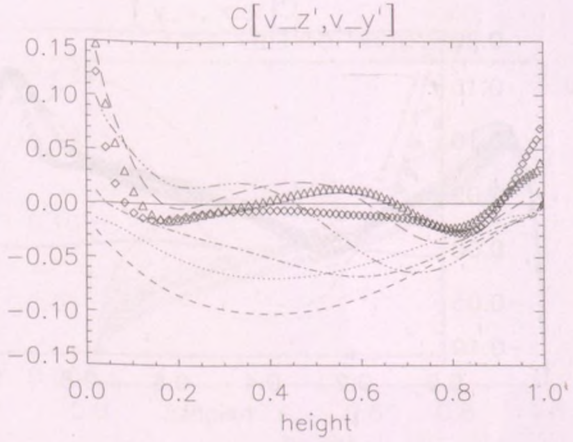

Figure 12: Profiles of the correlation coefficient of the vertical and zonal velocity fluctuations. Its value is not always negative.

TURBULENT EFFECTS ON SOLAR ACOUSTIC WAVES

K. Murawski
Department of Complex Physical Systems
UMCS, 20-031 Lublin, Poland
E-mail: `kmurawsk@tytan.umcs.lublin.pl`

Abstract

The effect of space- and time-dependent random mass density, velocity, and pressure fields on frequencies and amplitudes of solar acoustic waves is considered by means of the analytical perturbative method. The analytical results, which are valid for weak fluctuations and long wavelength waves, reveal frequency and amplitude alteration, the effect which depends on the type of a random field. In particular, short-wavelength frequencies of the sound waves that propagate along the constant gravity in an isothermal atmosphere are lifted up (reduced) by a space-dependent random mass density (pressure) field. Higher values of the acoustic cut-off frequency result in an increase of wave frequencies. This effect is stronger for longer waves. As a consequence of that in the case of the random pressure field the frequency correction exhibits a cross-over at intermediate values of wavenumber; long (short) sound waves experience a positive (negative) frequency shift. In the limit of a gravity-free medium, the effect of a random mass density field is to increase wave frequencies. Space-dependent random velocity and pressure fields reduce wave frequencies. While space-dependent random fields attenuate wave amplitudes, their time-dependent counterparts lead to wave amplification.

In the other example, the sound waves that are trapped in the vertical direction but are free to propagate horizontally are effected by a space-dependent random mass density field. This effect depends on a direction along which this field is varying. A random field, which varies along the horizontal direction, does not couple standing modes but increase their frequencies and attenuates amplitudes. These modes are coupled by a random field which depends on the vertical coordinate but the dispersion relation remains the same as in the case of the deterministic medium.

KEYWORDS: *Sun, MHD, plasma physics, turbulence, random fields*

1. Introduction

This paper is devoted to isolate some important effects related to influence of turbulence on frequencies and amplitudes of solar acoustic waves. The problem is vast and we do not claim to be comprehensive. Indeed, random wave propagation in the solar atmosphere has been a subject of recent intensive studies (e.g., Murawski 2002, Murawski et al. 2002). This subject stems from our wish to understand the complex physical phenomena which occur in the solar atmosphere and their influence on the solar oscillations. From this point of view simple models acquire much attention as they allow to separate and quantify effects of various stochastic fields on frequencies and amplitudes of these oscillations. Indeed, the study of sound waves in a space-dependent random mass density field reveals that these waves are accelerated and attenuated (Nocera et al. 2001). On the other hand, the effect of a time-dependent random mass density field is to accelerate and amplify the sound waves (Murawski et al. 2001a). These phenomena have a simple physical explanation in terms of scattering and parametric instabilities which lead to energy transfer between coherent and random fields (Murawski et al. 2001a). As a consequence of that the imaginary part of the wave frequency can attain negative or positive signs which correspond respectively to wave damping or amplification. A combined effect of a space- and time-dependent random mass density field that is represented in the form of the wave noise leads to resonance at which the phase speed of the random noise is equal to the wave phase speed (Murawski et al. 2001a). At this resonance the wave frequency tends to infinity.

The above studies have been carried out for a random mass density field and gravity-free plasma. It is natural then to enquire about influence of other random fields on spectral properties of sound waves which propagate in a gravitationally stratified atmosphere either freely or are trapped in a cavity. Understanding this influence is essential in developing theories of random p-modes which are essentially sound waves trapped in the solar interior by the temperature gradient (e.g., Roberts 1989).

As the problem of random sound wave propagation is complex, our strategy is to discuss simple structures first and then building on them construct more realistic models. Guiding by this strategy we consider first sound waves in simple random fields of a gravity-free plasma. Then, we generalize the theory by developing a model of sound waves which propagate along a gravity field in a random mass density field. At this stage we will show up the effect of gravity field on random sound waves. Using the knowledge gained from earlier models we discuss the effect of random fields on trapped sound waves. Extension of the latter problem on p-modes will be then straightforward although computationally expensive.

This paper is organized as follows. A simple model of sound waves is developed in Sec. 2. which presents the hydrodynamic equations and dispersion relation for the coherent sound waves. In Sec. 3. we derive the dispersion relations for a random flow. In this section, we summarize the influence of various space- and time-dependent random fields on frequencies and amplitudes of the solar sound waves. Sec. 4. discusses effects of random mass density and pressure fields on sound waves that propagate along a gravity field. The sound waves that are settled in a plasma cavity which contains a random mass density field are considered in Sec. 5.. This paper is concluded by the presentation and discussion of the main results in Sec. 6..

2. Hydrodynamic equations

We limit our discussion to magnetic-free plasma which is described by hydrodynamic equations:

$$\begin{aligned} \varrho_{,t} + \nabla \cdot (\varrho \mathbf{V}) &= 0, & (1)\\ \varrho \left[\mathbf{V}_{,t} + (\mathbf{V} \cdot \nabla) \mathbf{V} \right] &= -\nabla p + \varrho \mathbf{g}, & (2)\\ p_{,t} + \nabla \cdot (p \mathbf{V}) &= (1-\gamma) p \nabla \cdot \mathbf{V}. & (3) \end{aligned}$$

Here the symbol $_{,t}$ denotes a partial derivative with respect to time t, ϱ is the mass density, $\mathbf{V} = [u, 0, v]$ is the flow velocity, p is the pressure, γ is the adiabatic index, and $\mathbf{g}$ is the acceleration of a gravity field.

3. Sound waves in a random velocity field

It has been shown that flows can affect solar waves, modifying dispersion relations and changing line widths (Nakariakov and Roberts 1995, Nakariakov et al. 1998, Murawski 2000, Pintér et al. 2001a,b). In particular, Nakariakov et al. (1998) have found that even very weak flows, but with sufficiently sharp gradients, can dramatically affect propagation of the waves, causing enhanced coupling of different modes. In the other context it has been found by Murawski (2000) and Pintér et al. (2001a,b) that solar f- and p-modes are effected by a coherent flow. Thus, it is believed that the wave-flow interactions play a very important role in the dynamics of the solar atmosphere.

We consider the one-dimensional ($\partial/\partial y = \partial/\partial z = 0$) equilibrium:

$$\varrho_{\mathrm{e}} = \varrho_0 = const, \quad u_{\mathrm{e}} = u_{\mathrm{r}}(x,t), \quad p_{\mathrm{e}} = p_0 = const, \tag{4}$$

where the index r denotes random fields such that their ensemble averages are equal to zero,

$$\langle u_{\mathrm{r}}(x,t) \rangle = 0. \tag{5}$$

Using the perturbation technique (e.g., Murawski and Roberts 1993), we obtain the following dispersion relation:

$$\omega^2 - c_0^2k^2 = 4k\omega \int_{-\infty}^{\infty}\int_{-\infty}^{\infty} \frac{\hat{\omega}\hat{k}E(\hat{k}-k,\hat{\omega}-\omega)d\hat{k}d\hat{\omega}}{\hat{\omega}^2 - c_0^2\hat{k}^2}, \tag{6}$$

where E is the Fourier transform of the correlation function

$$R(x-X, t-T) = \langle u_{\mathrm{r}}(x,t)u_{\mathrm{r}}(X,T)\rangle. \tag{7}$$

From the dispersion relation of Eq. (6) it follows that the random sound waves are no longer dispersionless. We will see in the forthcoming part of this paper that sound waves experience not only frequency shift but also amplitude alteration due to a presence of the random field.

3.1. A space-dependent random flow

In this part of the paper we consider the case of a frozen random velocity field for which

$$u_{\mathrm{r}} = u_{\mathrm{r}}(x). \tag{8}$$

Then, Eq. (6) simplifies to

$$\omega^2 - c_0^2k^2 = 4k\omega^2 \int_{-\infty}^{\infty} \frac{\hat{k}E(\hat{k}-k)\,d\hat{k}}{\omega^2 - c_0^2\hat{k}^2}. \tag{9}$$

3.1.1. Approximate solution

We use the Gaussian spectrum

$$E(k) = \frac{\sigma^2 l_{\mathrm{x}}}{\pi} e^{-k^2 l_{\mathrm{x}}^2} \tag{10}$$

and the expansion

$$\omega = c_0k + \sigma^2\omega_2 + \cdots. \tag{11}$$

Here σ^2 is the variance of the random field and l_{x} is the correlation length. From Eq. (9) we obtain then

$$\omega_2\frac{l_{\mathrm{x}}}{c_0} = -\frac{2}{\sqrt{\pi}}k^2l_{\mathrm{x}}^2D(2kl_{\mathrm{x}}) - ik^2l_{\mathrm{x}}^2\left(1 - e^{-4k^2l_{\mathrm{x}}^2}\right), \tag{12}$$

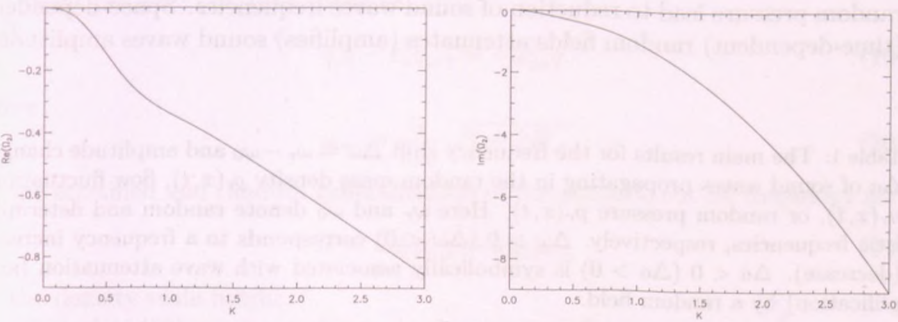

Figure 1: Real (left panel) and imaginary (right panel) parts of the frequency correction $\Omega_2 = \omega_2 \frac{l_x}{c_0}$ vs normalized wavenumber $K = kl_x$ for the sound waves in the space-dependent random velocity field of a Gaussian correlation function. As the real and imaginary parts of Ω_2 are negative for overall values of K we claim that the sound waves experience frequency reduction and amplitude attenuation in a weak space-dependent random velocity field.

where the function

$$D(\xi) = e^{-\xi^2} \int_0^{\xi} e^{t^2} \mathrm{d}t \tag{13}$$

is Dawson's integral (Press et al. 1992).

From Eq. (12) it follows that the real and imaginary parts of ω_2 are lower than zero. As $\sigma^2\omega_2$ consists the lowest-order random correction to the frequency we claim that a space-dependent random flow of the Gaussian correlation function reduces frequencies and attenuates sound waves. Indeed, Fig. 1 confirms these claims. The effect of random field grows with the normalized wavenumber $K = kl_x$.

We conclude that space-dependent random flows exert a similar effect on sound waves and the solar f-mode (Murawski 2000, Pinter et al. 2001a,b), reducing their frequencies and attenuates amplitudes.

3.2. Various random fields

An influence of various random fields on sound waves frequencies and amplitudes can be studied in a similar way as in Sec. 3.1.. Table 1 summarizes the corresponding results. Frequencies of the sound waves are increased by a random mass density (Nocera et al. 2001, Murawski et al. 2001a) and a time-dependent random velocity (Murawski et al. 2001b). A space-dependent random flow and random pressure lead to reduction of sound waves frequencies. Space-dependent (time-dependent) random fields attenuates (amplifies) sound waves amplitudes.

Table 1: The main results for the frequency shift $\Delta\omega = \omega_r - \omega_0$ and amplitude changes Δa of sound waves propagating in the random mass density $\varrho_\mathrm{r}(x,t)$, flow fluctuations $u_\mathrm{r}(x,t)$, or random pressure $p_r(x,t)$. Here ω_r and ω_0 denote random and deterministic frequencies, respectively. $\Delta\omega > 0$ ($\Delta\omega < 0$) corresponds to a frequency increase (decrease). $\Delta a < 0$ ($\Delta a > 0$) is symbolically associated with wave attenuation (amplification) by a random field.

	$\varrho_\mathrm{r}(x)$	$\varrho_\mathrm{r}(t)$	$u_\mathrm{r}(x)$	$u_\mathrm{r}(t)$	$p_r(x)$	$p_r(t)$
$\Delta\omega$	>0	>0	<0	>0	<0	<0
Δa	<0	>0	<0	>0	<0	>0

4. Random sound waves in a gravitationally stratified atmosphere

The above models of random sound propagation can be extended to the case of a gravitationally stratified atmosphere for which we consider the frozen equilibrium of random mass density ϱ_r and pressure p_r fields which overlay their coherent counterparts ϱ_0 and p_0:

$$\varrho_\mathrm{e}(z) = \varrho_0(z) + \varrho_\mathrm{r}(z) \equiv \varrho_0(1+\varepsilon_\varrho), \quad <\varrho_\mathrm{e}>=\varrho_0, \tag{14}$$

$$p_\mathrm{e}(z) = p_0(z) + p_\mathrm{r}(z) \equiv p_0(1+\varepsilon_p), \quad <p_\mathrm{e}>=p_0. \tag{15}$$

Small amplitude perturbations of this equilibrium satisfy the wave equation

$$\varrho_\mathrm{e} V_{,tt} - (\varrho_\mathrm{e} c_\mathrm{e}^2 V_{,z})_{,z} = 0, \tag{16}$$

where the equilibrium sound speed c_e is given as

$$c_\mathrm{e}^2 = \frac{\gamma p_\mathrm{e}}{\varrho_\mathrm{e}}. \tag{17}$$

Following Roberts (1989) it is convenient to introduce the new variable

$$q(z,t) = \sqrt{\varrho_\mathrm{e}} c_\mathrm{e}^2 V_{,z} \tag{18}$$

in which Eq. (16) can be written as

$$q_{,tt} - c_{\mathrm{e}}^2 q_{,zz} = -\omega_{\mathrm{ae}}^2 q. \tag{19}$$

Here

$$\omega_{\mathrm{ae}} = \frac{c_{\mathrm{e}}}{2H}\sqrt{1+2H_{,z}} \tag{20}$$

is the stratified and random generalization of the acoustic cut-off frequency and

$$H = \log \varrho_{\mathrm{e},z} \simeq \log \varrho_{0,z} \tag{21}$$

is the density scale height.

Equation (19) can be rewritten in the operator form as

$$L_0 q + Mq = 0 \tag{22}$$

with

$$L_0 = \frac{\partial^2}{\partial t^2} - c_0^2 \frac{\partial^2}{\partial z^2} + \omega_{\mathrm{a}}^2 (1 + 2H_{,z}), \tag{23}$$

$$M = \varepsilon_\varrho \frac{\partial^2}{\partial t^2} - \varepsilon_{\mathrm{p}} c_0^2 \frac{\partial^2}{\partial z^2} + \varepsilon_{\mathrm{p}} \omega_{\mathrm{a}}^2 (1 + 2H_{,z}). \tag{24}$$

Here

$$\omega_{\mathrm{a}} = \frac{c_0}{2H} \tag{25}$$

is the coherent acoustic cut-off frequency.

4.1. The case of the isothermal atmosphere

In the case of the isothermal atmosphere

$$H = \mathrm{const}, \quad c_0 = \mathrm{const}, \quad \omega_{\mathrm{a}} = \frac{\gamma g}{2c_0} = \mathrm{const}. \tag{26}$$

4.1.1. Non-random dispersion relation

In the non-random atmosphere the operator $M = 0$. Then, from Eq. (22) it follows that a sound wave of

$$q \sim e^{i(kz - \omega_0 t)}$$

satisfies the following dispersion relation:

$$\omega_0^2 = \omega_{\mathrm{a}}^2 + c_0^2 k^2. \tag{27}$$

4.1.2. Random dispersion relation

Now, we adopt a weak random field approximation as in the method by Nocera et al. (2001). The random correction to the above dispersion relation is

$$\omega^2 - \omega_0^2 = \int_{-\infty}^{\infty} \frac{f(k,\hat{k},\omega)\,d\hat{k}}{\omega^2 - c_0^2\hat{k}^2 - \omega_{\mathrm{a}}^2}, \tag{28}$$

where

$$f(k,\hat{k},\omega) = \omega^4 E_{\varrho\varrho} - (c_0^2k^2\omega^2 + 2\omega_{\mathrm{a}}^2\omega^2 + c_0^2\hat{k}^2\omega^2)E_{\varrho p} + (c_0^4k^2\hat{k}^2 + c_0^2\hat{k}^2\omega_{\mathrm{a}}^2 + \omega_{\mathrm{a}}^2c_0^2k^2 + \omega_{\mathrm{a}}^4)E_{pp}. \tag{29}$$

Here $E_{\varrho\varrho}$ and E_{pp} are the correlation functions of the random mass density and pressure, respectively. The quantity $E_{\varrho p}$ is the cross-correlation function.

We assume the Gaussian profiles for the correlation functions of the type

$$E_{\mathrm{ij}} = \frac{\sigma_{\mathrm{i}}\sigma_{\mathrm{j}}l_{\mathrm{z}}}{\pi}e^{-k^2l_{\mathrm{z}}^2}, \tag{30}$$

where the indices i and j correspond to ϱ and p. For such correlation functions we can evaluate the integrals

$$I_{ij} \equiv \int_{-\infty}^{\infty} \frac{E_{\mathrm{ij}}(\hat{k}-k)\,d\hat{k}}{\hat{k}^2 - k^2} = \frac{\sigma_{\mathrm{i}}\sigma_{\mathrm{j}}l_{\mathrm{z}}}{2\sqrt{\pi}k}\Big[-2D(2kl_{\mathrm{z}}) + i\sqrt{\pi}\left(1 + e^{-4k^2l_{\mathrm{z}}^2}\right)\Big] \tag{31}$$

and

$$J_{ij} \equiv \int_{-\infty}^{\infty} \frac{\hat{k}^2E_{\mathrm{ij}}(\hat{k}-k)\,d\hat{k}}{\hat{k}^2 - k^2} = \frac{\sigma_{\mathrm{i}}\sigma_{\mathrm{j}}}{\sqrt{\pi}}\left[1 - kl_{\mathrm{z}}D(2kl_{\mathrm{z}}) + i\frac{\sqrt{\pi}}{2}kl_{\mathrm{z}}\left(1 + e^{-4k^2l_{\mathrm{z}}^2}\right)\right]. \tag{32}$$

Substituting Eqs. (31) and (32) into Eq. (28) with a use of the expansion of Eq. (11), we obtain

$$2c_0^2\sigma^2\omega_2 = -\omega_0^3I_{\varrho\varrho} + \omega_0(\omega_0^2 + \omega_a^2)I_{\varrho p} + c_0^2\omega_0J_{\varrho p} - c_0^2\omega_0J_{pp} - \omega_a^2\omega_0I_{pp}. \tag{33}$$

4.1.3. Random mass density fluctuations

To realize the case of random mass density fluctuations alone we set in Eq. (33) $\sigma_p = 0$. Rearranging the corresponding terms we have

$$\omega_2 = \frac{1}{2\sqrt{\pi}}\frac{l_z\omega_0^3}{c_0^2k}D(2kl_z) - \frac{i}{4}\frac{l_z\omega_0^3}{c_0^2k}(1 + e^{-4k^2l_z^2}). \tag{34}$$

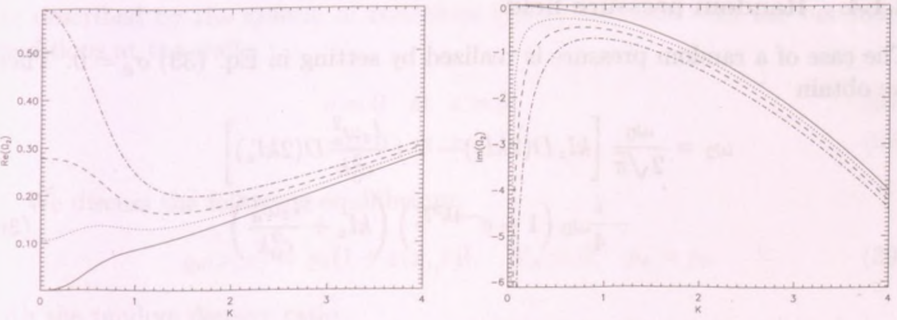

Figure 2: Real (left panel) and imaginary (right panel) parts of the frequency correction $\Omega_2 = \frac{l_z}{c_0}\omega_2$ vs normalized wavenumber $K = kl_z$ for the sound waves in the random mass density field. The solid, dashed, dotted, and dashed-dotted curves (from the bottom to the top of the left panel) correspond respectively to the sound speed $c_0 = 100$ km/s, $c_0 = 20$ km/s, $c_0 = 17$ km/s, and $c_0 = 15$ km/s. The other parameters are chosen as: the correlation length $l_z = 10^3$ km, the solar surface gravitational acceleration $g = 274$ m/s^2, and the ratio of specific heats $\gamma = 5/3$.

Fig. 2 shows the results which are obtained from Eq. (34) for various values of the sound speed c_0. According to Eq. (26) a higher value of c_0 corresponds to a lower value of the acoustic cut-off frequency. The effect of a lower (higher) value of sound speed (acoustic cut-off frequency) is to lift up the real part of the frequency correction ω_2 which attains finite values for long waves. These waves are much attenuated as the imaginary part of ω_2 is infinite at $k = 0$. Obviously in the limit of $k = 0$ the pertubative method fails as it corresponds to small corrections.

The case of $c_0 = 100$ km/s is very close to the gravity-free medium for which $\omega_a = 0$ and $\omega_0 = kc_0$. Then,

$$\frac{l_z}{c_0}\omega_2 = \frac{k^2 l_z^2}{2\sqrt{\pi}} D(2kl_z) - \frac{i}{4} k^2 l_z^2 \left(1 + e^{-4k^2 l_z^2}\right) . \qquad (35)$$

This result converges with the findings of Nocera et al. (2001).

In summary, the effect of random mass density field is to shift up the frequency and attenuate the sound waves. This effect is higher for shorter waves and higher values of the acoustic cut-off frequency.

4.1.4. Random pressure field

The case of a random pressure is realized by setting in Eq. (33) $\sigma_\varrho = 0$. Then, we obtain

$$\omega_2 = \frac{\omega_0}{2\sqrt{\pi}} \left[k l_z D(2kl_z) - 1 + \frac{l_z \omega_a^2}{c_0^2 k} D(2kl_z) \right] - \frac{i}{4}\omega_0 \left(1 + e^{-4k^2 l_z^2}\right) \left(k l_z + \frac{l_z \omega_a^2}{c_0^2 k} \right). \tag{36}$$

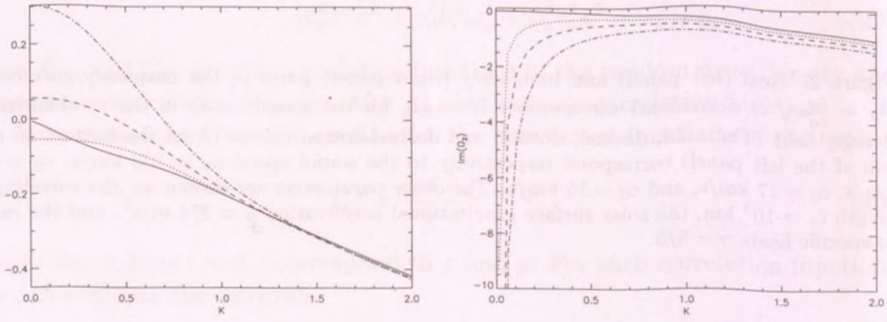

Figure 3: Real (left panel) and imaginary (right panel) parts of the frequency correction $\Omega_2 = \frac{l_z}{c_0}\omega_2$ vs normalized wavenumber $K = kl_z$ for the sound waves in the random pressure field. The parameters are chosen as in Fig. 2.

Fig. 3 displays the results of Eq. (36) for the same set of parameters as in Fig. 2. We conclude that the random pressure acting alone lead to wave attenuation in the whole range of wavenumbers k. For high (low) values of sound speed (cut-off frequency) sound waves experience frequency reduction by the random pressure field. As lower (higher) values of sound speed (cut-off frequency) lifts us ω_2 at $k = 0$ the sound waves increase there frequency for low k but their frequencies are reduced at high values of k. The cross-over at which $\omega_2 = 0$ occurs at intermediate values of k.

5. Trapped sound waves in random mass density fields

It is very instructive to envisage the sound waves which are trapped by two horizontal walls which bound gravity-free plasma at $z = 0$ and $z = h$. These waves are described by the system of equations (1)-(3) together with the boundary conditions at the walls:

$$v = 0 \quad \text{at} \quad z = 0, \tag{37}$$

$$v = 0 \quad \text{at} \quad z = h. \tag{38}$$

We discuss the following equilibrium:

$$\varrho_e(x,z) = \varrho_0(1+\varepsilon(x,z)), \quad \mathbf{V}_e = 0, \quad p_e = p_0 \tag{39}$$

with the random density ratio

$$\varepsilon(x,z) = \frac{\varrho_r(x,z)}{\varrho_0}. \tag{40}$$

In the above formulae the indices e and 0 denote respectively equilibrium and constant coherent quantities, and ϱ_r is a random mass density field that depends both on the horizontal x and vertical z coordinates.

Linear perturbations of the above equilibrium satisfy the set of equations

$$(1+\varepsilon(x,z))u_{,tt} = c_0^2(u_{,xx} + v_{,xz}), \tag{41}$$

$$(1+\varepsilon(x,z))v_{,tt} = c_0^2(u_{,xz} + v_{,zz}). \tag{42}$$

5.1. Non-random dispersion relation

From equations (41), (42) in the limit of a coherent medium ($\varepsilon = 0$) we get that a Fourier component of a vertical component of the flow velocity

$$v \sim e^{i(kx-\omega t)}$$

satisfy the wave equation

$$v_{,zz} + \kappa^2 v = 0, \quad \kappa^2 = \frac{\omega^2}{c_0^2}\left(1 - \frac{k^2 c_0^2}{\omega^2}\right). \tag{43}$$

This equation together with the boundary conditions of equations (37), (38) is solved by

$$v(z) = v_n(z) \sim \sin(\kappa_n z), \tag{44}$$

where

$$\kappa_n = \frac{\omega_n}{c_0}\sqrt{1 - \frac{k^2 c_0^2}{\omega_n^2}} = \frac{n\pi}{h}, \quad n = 1, 2, \cdots. \tag{45}$$

Here the index n which denotes the mode number has been added to point out discrete values of κ.

Rearranging equation (45) we obtain the dispersion relation

$$\omega_n^2 = c_0^2(\kappa_n^2 + k^2). \tag{46}$$

In this equation $\kappa_n c_0$ plays a role of a cut-off frequency.

It is noteworthy that in the limit of a homogeneous medium $h \to \infty$ leads to $\omega^2 = c_0^2 k^2$.

5.2. Random mass density field along the vertical direction

We consider now the case of the random mass density field which depends on the vertical coordinate z,

$$\varrho_r = \varrho_r(z). \tag{47}$$

Expanding the wave field v in terms of the coherent $< v >$ and random v' components we derive from Eqs. (41) and (42) that

$$< v >_{,zz} + \kappa^2 < v > = -\kappa^2 < \varepsilon v' > - \frac{k^2}{\kappa^2} < \varepsilon v'_{,zz} > - \frac{k^2}{\kappa^2} < \varepsilon_{,z} v'_{,z} >, \tag{48}$$

$$v'_{,zz} + \kappa^2 v' = -\kappa^2 \varepsilon < v > - \frac{k^2}{\kappa^2} \varepsilon < v >_{,zz} - \frac{k^2}{\kappa^2} \varepsilon_{,z} < v >_{,z} . \tag{49}$$

Equations (48) and (49) can be solved with a use of the expansions

$$< v > = \sum_{n=1} a_n \sin(\kappa_n z), \quad v' = \sum_{n=1} a'_n \sin(\kappa_n z), \quad \varrho(z) = \sum_{n=1} \varepsilon_n \cos(\kappa_n z). \tag{50}$$

Substituting these equations into Eq. (49) we find that the coefficient a' is expressed in terms of the set of coefficients $\{a_n\}$, $n = 1, 2, \cdots$. Eq. (48) consists then an algebraic equation for the set of the coefficients $\{a_n\}$.

From the above analysis it follows that any random field which depends on the vertical coordinate z leads to modes coupling but it does not alter frequencies of the horizontally propagating waves.

5.3. Random mass density field along the horizontal direction

We discuss now the case of the random mass density field

$$\varrho_r = \varrho_r(x). \tag{51}$$

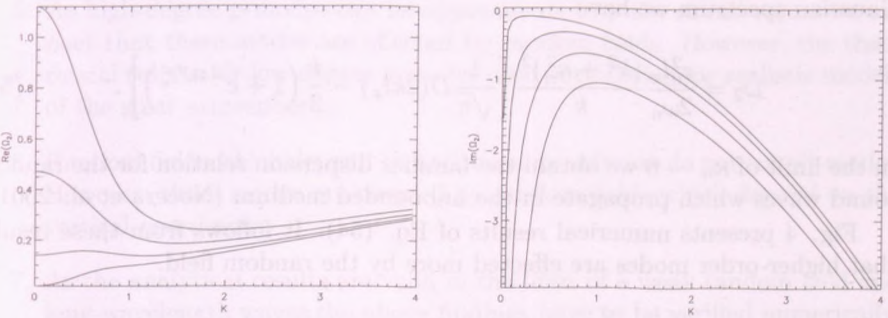

Figure 4: Real (left panel) and imaginary (right panel) parts of the frequency correction $\Omega_2 = \omega_2 l_x / c_0$ vs normalized wavenumber $K = k l_x$ for the sound waves that are trapped between two horizontal walls in the case of the random mass density field $\varrho_r(x)$. The curves from the bottom (top) to the top (bottom) of the left (right) panel correspond respectively to the mode number $n = 1$, $n = 2$, $n = 3$, and $n = 4$. The other parameters are chosen as: the correlation length $l_x = 10^3$ km and the distance between walls $h = 10^4$ km. Higher modes are effected more by the random field.

When deriving the random dispersion relation we have followed the method described in the above sections. The difference here is that only the coherent $< v >$ and random v' fields are expanded in terms of the set of the basic functions $\sin(\kappa_n z)$, $n = 1, 2, \cdots$, while $\varrho(x)$ is left alone. See Eq. (50). Using the orthogonal properties of these functions we end up with the random dispersion equation

$$\kappa^2 - \kappa_n^2 = \int_{-\infty}^{\infty} \frac{\left(\frac{k^2}{\kappa^2}\kappa_n^2 + \kappa^2\right)^2}{\hat{\kappa}^2 - \kappa_n^2} E(\hat{k} - k) d\hat{k}. \tag{52}$$

In the limit of $\kappa_n \to 0$ we obtain the dispersion relation which was already derived by Nocera et al. (2001). From this equation it follows that the standing modes are not coupled by the random field. However, their frequencies and amplitudes are effected by this field.

We get the approximate solution of equation (52) with the use of the expansion

$$\omega = \omega_n + \sigma^2 \omega_2 \tag{53}$$

and the replacement κ^2 by κ_n^2 in the expression under the integral. For the

Gaussian spectrum we have

$$\omega_2 = \frac{c_0^2 l_x}{2\omega_n} \frac{(k^2+\kappa_n^2)^2}{k} \left[\frac{1}{\sqrt{\pi}} D(2kl_x) - \frac{i}{2} \left(1 + e^{-4k^2 l_x^2} \right) \right] . \qquad (54)$$

In the limit of $\kappa_n \to 0$ we obtain the familiar dispersion relation for the random sound waves which propagate in the unbounded medium (Nocera et al. 2001).

Fig. 4 presents numerical results of Eq. (54). It follows from these results that higher-order modes are effected more by the random field.

6. Summary

The above presented results for sound waves have been discussed for various random fields and the Gaussian correlation function. These results can be summarized as follows:

1. Random fields influence spectral properties of sound waves: reduce or increase their frequencies and attenuates or amplifies their amplitudes. These effects depend on a character of the random fields. However, generally space-dependent (time-dependent) random fields attenuates (amplifies) sound waves amplitudes. Sound waves experience a frequency decrease by a space-dependent random velocity field and pressure field. In the latter case the effect is similar for space- and time-dependent fields. Wave frequencies are increased by a time-dependent random velocity field and space- and time-dependent mass density fields;

2. Random effects are stronger for stronger random fields and shorter waves;

3. A space-dependent random pressure field in a gravity-free atmosphere works similarly as a space-dependent random flow field, reducing waves frequencies and attenuating their amplitudes;

4. Trapped modes are not coupled by random fields which vary in the direction along which these modes propagate. However, such fields alter both their frequencies and amplitudes. These modes are coupled by random fields which depend on the coordinate perpendicular to the direction of modes propagation. In the latter case the dispersion relation remains the same as in the case of deterministic medium;

5. As high-degree p-modes can be approximated by the sound waves we expect that these modes are affected by random fields. However, the theoretical results for low-degree p-modes need verification for realistic models of the solar atmosphere;

6. Random fields which depend on horizontal coordinate do not couple modes. However, these modes are coupled by random fields which depend on the vertical coordinate;

7. As the analytical results are valid in the limit of a weak random field and long-wavelength waves the above findings have to be verified numerically. Already an effort into this direction has been made by Mędrek et al. (2000), Nocera et al. (2001) and Murawski et al. (2001a,b) who have verified the analytical results for space- and time-dependent random mass density fields.

Acknowledgments

The author expresses his thanks to Dr. L. Nocera and Prof. E. Pelinovsky for stimulating discussions. A part of this work was financially supported by the State Committee for Scientific Research in Poland, KBN grant no. 2 PO3D 017 17 and it was also made in the frame of NATO grant no. PST.CLG.976135.

References

Christensen-Dalsgaard J.: 1998, Lecture notes on stellar oscillations, fourth edition, Aarhus Univ. (http://www.obs.aau.dk/~ jcd/oscilnotes/)

Mędrek M., Michalczyk J., Murawski K., Nocera L.: 2000, *Waves in Random Media* **12**, 211

Murawski K.: 2000, *ApJ* **537**, 495

Murawski K., Roberts B.: 1993, *Astron. Astrophys.* **272**, 595

Murawski K., Nocera L., Mędrek M.: 2001a, *Astron. Astrophys.* **376**, 708

Murawski K., Mędrek M., Ostrowski M.: 2001b, in Proceed. of the INTAS Workshop on MHD waves in Astrophysical Plasmas, eds. J.L. Ballester & B. Roberts, p. 179

Murawski K., Nocera L., Pelinovsky E.N.: 2002, *Astron. Astrophys.* **387**, 335

Nakariakov V.M., Roberts B.: 1995, *Solar Phys.* **159**, 213

Nakariakov V.M., Roberts B., Murawski K. 1998, *Astron. Astrophys.* **332**, 795

Nocera L., Medręk M., Murawski K.: 2001, *Astron. Astrophys.* **373**, 303

Pintér B., Erdélyi R., New R.: 2001a, *Astron. Astrophys.* **372**, L17

Pintér B., New R., Erdélyi R.: 2001b, *Astron. Astrophys.* **378**, L1

Roberts B., 1989, Magnetohydrodynamic waves in stratified atmospheres, in L. Tanovic, N. Konjevic, and N. Tanovic, editors, *Physics of Ionized Gases*, pages 687–717, Commack, NY, Nova Science, Proceedings of the 1988 SPIG, 15-19 Aug. 1988, Sarajevo, YU

ABSOLUTE AND CONVECTIVE INSTABILITIES IN OPEN SHEAR FLOW LAYERS

M. Terra Homem[1] **and R. Erdélyi**[2]
Univ. of Sheffield, SPARC, Dept. of Applied Maths.
Hicks Bldg., Hounsfield Rd., Sheffield S3 7RH, England
E-mail: [1]`m.homem@sheffield.ac.uk`, [2]`robertus@sheffield.ac.uk`

Abstract

In the present paper we study the absolute and convective nature of instabilities in open shear flows by carrying out fully non-linear adiabatic 2-D hydrodynamic numerical simulations. We found the value of mean flow for which perturbations change from absolute to convective unstable. We fully recover the results of a previous analytic solution. We found that (i) an inviscid incompressible fluid is the most unstable configuration; (b) compressibility and viscosity decrease the value of mean flow necessary for the transition from absolute to convective instability; (c) even a viscosity has dominant influence over compressibility.

KEYWORDS: *Instability, Absolute, Convective*

1. Introduction

Shear flows are present in most solar-terrestrial applications and it is of fundamental importance to understand their stability. To analyze the stability of shear flows with respect to perturbations finite in space one has to solve an initial-value problem. When a shear flow is unstable there can be two different scenarios. In the first scenario the initial finite perturbation grows exponentially at any spatial position (i.e. the instability is called absolute). In the second scenario the initial perturbation also grows exponentially, but it is swept away by the flow so fast that perturbations decay at any fixed spatial position (i.e. the instability is called convective) eventually leaving the flow unperturbed. The classification of these instabilities is important for the understanding of the physical processes in solar plasmas and space weather, in particular for the interpretation of in-situ satellite observations.

To investigate the problem of initially perturbed open shear flows numerically VAC (Versatile Advection Code) has been used. A detailed description of VAC can be found in e.g., Tóth (1996); Tóth (1997). A fully non-linear 2-D hydrodynamic simulation of the adiabatic approximation in a 400×800 uniform mesh was carried out using a Flux Corrected Transport (FCT) method. The equilibrium is prescribed by a uniform density throughout the whole domain and there is no vertical component of equilibrium velocity, i.e. ($v_y = 0$). For the v_x component of the velocity the shear profile is defined as $U = U_0 + \frac{1}{2}\tanh(y)$. Here velocity is normalised by the difference in the two streams ΔU and spatial coordinates are normalised by half the momentum thickness of the shear layer, h_0.

2. Numerical Simulations

In order to study the transition from an absolute to convective instability the mean flow shall be varied. We shall find the critical (or threshold) value of mean flow, (U_c), for which the transition from absolute to convective instability occurs.

Because the non-dimensionalisation used here is slightly different from the one used by Huerre & Monkewitz (1985) in their analytic work, a simple transformation must be carried out to compare the two approaches. Huerre & Monkewitz (1985) derived in their analytic studies a threshold, $R_{th} = 1.3$, above that of a velocity shear perturbations were absolutely unstable. By their definition $R = \frac{\Delta U}{2\bar{U}}$; if ΔU is considered to be unity and $R = 1.3$, then $\bar{U}_c = 0.38$. This means for mean flows below 0.38 the shear layer is absolutely unstable.

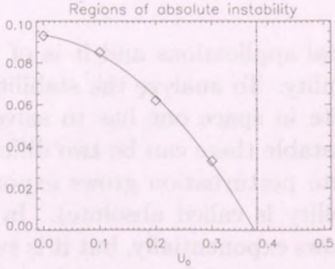

Figure 1: Variation of the growth rates with U_0 for an incompressible fluid. The dot-dashed line represents the threshold found by Huerre & Monkewitz (1985).

To test our simulations the asymptotic solution found by Huerre & Monkewitz (1985) must be recovered. Fig. 2. compares the results of our numerical and the analytical approach by Huerre & Monkewitz (1985). The results of the two approaches coincide perfectly, i.e. $U_c = 0.38$.

Detailed response of an incompressible and inviscid fluid to an initial perturbation at various snapshots is shown in Fig. 2. for two cases: (i) absolutely unstable ($U_0 = 0 < U_c$) and (ii) convectevely unstable ($U_0 = 0.4 > U_c$).

Let us now introduce compressibility in the open shear layer. The comparison of the compressible and incompressible limit is shown in Fig. 2..

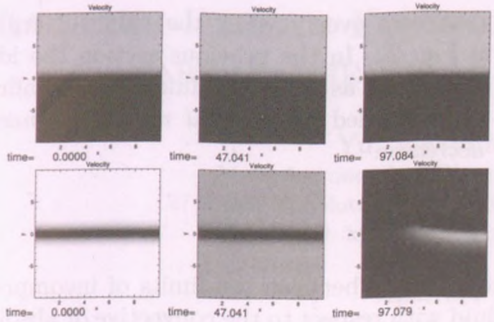

Figure 2: Response of an incompressible flow to an initial perturbation at various snapshots. Streamlines are plotted for two physically distinct behaviours: (a) convectively unstable $U_0 = 0.4$ (top row), (b) and absolutely unstable $U_0 = 0.0$ (bottom row).

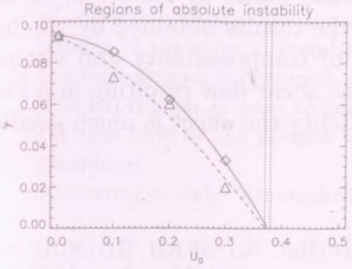

Figure 3: Variation of the growth rates with U_0 for a compressible fluid (dashed line) and for an incompressible fluid (solid line).

Fig. 2. shows that compressibility *decreases* the value of critical mean flow velocity from $U_c = 0.38$ to $U_c = 0.37$. Less mean flow is needed to sweep away an initial perturbation which also means the growth rate of the perturbation is smaller due to compressibility. It is known that an increase in Mach number reduces the range of angles of propagation of unstable modes and at supersonic speeds parallel propagating modes are stable (Baranov et al., 1992).

Finally let us move to study the absolute and convective instability of open shear flows when there is (a week) viscosity present. Comparison of the inviscid incompressible and viscous compressible cases is shown in Fig 2..

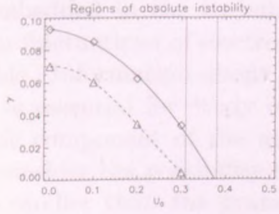

Figure 4: Variation of the growth rates as a function of mean flow U_0 for a viscous compressible fluid with Reynolds number $Re = 10^3$ (dashed line) and for an inviscid incompressible fluid (solid line).

The introduction of viscosity decreases even further the value of critical mean flow as it is clearly shown in Fig. 2.. In the previous section the ideal compressible flow can actually be considered as a viscous fluid with an infinite Reynolds number. It may then be concluded the *critical mean flow needed decreases as the Reynolds number decreases.*

3. Conclusions

This study has allowed a direct comparison between the limits of incompressible and compressible open shear fluid with respect to the convective or absolute nature of its perturbation. The analytic threshold found by Huerre & Monkewitz (1985) is in an excellent agreement with the results obtained by the fully nonlinear numerical simulations. The effects of compressibility and viscosity are similar. Both have a stabilising effect on the shear flow resulting in a lower value of U_c. However, in the case of compressibility the effect is much smaller.

Acknowledgments

MTH thanks FCT, Portugal, for its financial support (Ref. No. SFRH/BD/8076/2002). RE acknowledges M. Kéray for patient encouragement and is grateful to NSF Hungary, (OTKA, Ref. No. TO32462). We also acknowledge Drs M.S Ruderman for the many useful discussions and comments and G. Tóth the principal author of VAC.

References

Baranov, V. B., Fahr, H. J., Ruderman, M. S. 1992, *Astron. Astrophys.* , 261, 341

Huerre, P., Monkewitz, P. 1985, J. Fluid Mech., 159, 151

Tóth, G. 1996, Astrophys. Letters & Comm., 34, 245

Tóth, G. 1997, in High Performance Computing and Networking Europe, 1225, Springer-Verlag, 253

ELECTRON-DENSITY FLUCTUATIONS IN THE LOWER PART OF THE SOLAR ATMOSPHERE

Yu. Kyzyurov
Main Astronomical Observatory NASU
27 Akad. Zabolotnogo Str., 03680 Kiev, Ukraine
E-mail: `kyzyurov@mao.kiev.ua`

Abstract

On the basis of quasi-hydrodynamic equations we consider formation of electron-density fluctuations by turbulent mixing of weakly-ionized plasma in the solar atmosphere. An expression for the power spectrum of the fluctuations is obtained, assuming quasi-neutrality and isothermality. The expression is used to predict the shape of the spatial spectrum and the rms level of the plasma fluctuations in the lower part of the solar atmosphere.

KEYWORDS: *solar atmosphere, turbulence, plasma fluctuations*

1. Introduction

Studies of motions and magnetic fields on the photosphere are very important for understanding basic solar phenomena, such as atmospheric energy transport, turbulent diffusion of magnetic fields or chaotic excitation of solar oscillations (e.g., see Cadavid et al., 1998; Norton & Ulrich, 2000). Data of observations indicate that photospheric flows include both organized and stochastic motions (Cadavid et al., 1998). Spectra associated with the stochastic velocity fields obey power laws, which are consistent with the spectrum of Kolmogorov turbulence. Plasma in the lower part of solar atmosphere is only weakly ionized (Krinberg, 1971): the charged components are a minor species and have no influence on both the average motion and turbulent pulsations of neutral gas (at least outside the active regions of solar atmosphere). It may be said that the ion-electron plasma is embedded in the turbulent flow of neutral gas. Such a situation may result in fluctuations of electron density, even though the gas motions are incompressible. Information about the velocity fields and the electron-density fluctuations is essential for study of the contribution of solar photosphere to the stochastic component of the magnetic field of the Sun. The aim of this report is to consider the possibility of formation of electron density fluctuations (with scales smaller than the granular scale $l < L_g$) by turbulent mixing of weakly-ionized plasma in the solar atmosphere and to obtain the spectrum of the fluctuations.

2. Small-scale electron-density fluctuations in turbulent weakly-ionized plasma of the solar atmosphere

For description of slow processes in the weakly-ionized plasma, when the time-scale is larger than inverse value of ion-neutral collision frequency $t \gg \nu_i^{-1}$, and the length-scale of the processes is larger than the ion mean free path, $l \gg \Lambda_i$, and if the motion of neutral gas is known and is unchanged by interaction with charged components ($\mathbf{u}$ is the velocity of neutral gas) a simplified system of macroscopic (quasi-hydrodynamic) equations can be used (Gurevich & Tsedilina, 1967). In this set of equations, the variables are chosen as density N_s and velocity $\mathbf{v}_s$ for each species ($s = i, e$):

$$\partial N_s/\partial t + \vec{\nabla}(N_s \mathbf{v}_s) = 0, \tag{1}$$

$$\nu_s(\mathbf{v}_s - \mathbf{u}) = q_s m_s^{-1}\mathbf{E} + \omega_{Bs}(\mathbf{v}_s \times \mathbf{b}) - v_{Ts}\vec{\nabla} N_s/N_s, \tag{2}$$

where $\nu_s =$ the charged particle neutral collision frequency, q_s the particle charge ($q_i = -q_e = -e$), $m_s =$ mass of the particle, $\omega_{Bs} =$ the gyrofrequency, $\mathbf{b} = \mathbf{B}/B$ is the unit vector along the magnetic field $\mathbf{B}$, $v_{Ts} =$ the thermal velocity, $\mathbf{E} =$ the electric field.

In the lower part of solar atmosphere (a quiet area) (a) $\nu_i \gg \omega_{Bi}$, assumptions of (b) isothermality, $T_e \approx T_i \approx T_n = T$, and (c) quasi-neutrality, $N_e \approx N_i = N$, are valid; if (d) we consider the only electric field, which is required to prevent charge separation (due to $\mathbf{E}$ electrons tend to follow ions); (e) the velocity and electron-density fields may be separated into mean and fluctuating parts: $\mathbf{u} = \mathbf{u}_0 + \mathbf{u}_1$ ($\mathbf{u}_1$ is the turbulent velocity field, $\mathbf{u}_1 < \mathbf{u}_0$, $\langle \mathbf{u}_1 \rangle = 0$), $N = N_0 + N_1$ ($N_1 < N_0$, $\langle N_1 \rangle = 0$); when (f) the flow of neutral gas is incompressible, $\vec{\nabla} \cdot \mathbf{u} = \vec{\nabla} \cdot \mathbf{u}_1 = 0$, (g) length-scales of the random ingradients $\mathbf{u}_1$ and N_1 are small compared with the scales, L_g, L_N, of variation of mean quantities $\mathbf{u}_0$, N_0, respectively ($l < L_N = (|\vec{\nabla} N_0|/N_0)^{-1} \sim L_g$), and the same may be said about time-scales, the following equation describing generation of relative plasma-density fluctuations, $\delta N = N_1/N_0$, in the turbulent flow of weakly-ionized gas can be derived from the set of equations (1), (2):

$$\partial \delta N/\partial t - D_A \nabla^2 \delta N + \vec{\nabla}(\delta N \mathbf{u}_1) = -L_N^{-1}(\mathbf{u}_1 \cdot \mathbf{n}) - \beta_i \vec{\nabla}(\mathbf{u}_1 \times \mathbf{b}), \tag{3}$$

where $\beta_i = \omega_{Bi}/\nu_i$, D_A is the ambipolar diffusion coefficient, $\mathbf{n} = L_N(\vec{\nabla} N_0/N_0)$, is the unit vector along the gradient of N_0.

The process in which the neutral gas turbulence in conjunction with a background electron-density gradient produce plasma irregularities by mixing regions of high and low density is described by the first term on the RHS of (3), this term is more important at larger scales, $l > \beta_i L_N$; the second dominates at smaller ones, $l < \beta_i L_N$, and represents the interaction of the plasma embedded in the turbulent motions of neutral gas with the magnetic field.

Under the assumption of statistical homogeneity and stationarity of the random fields $\mathbf{u}_1(\mathbf{x},t)$ and $\delta N(\mathbf{x},t)$, the Fourier transform of (3) is

$$(D_A k^2 - \mathrm{i}\omega)\delta N(\mathbf{k},\omega) + \mathrm{i}k_j \int \mathrm{d}\mathbf{k}'\mathrm{d}\omega' \delta N(\mathbf{k}',\omega') u_{1j}(\mathbf{k}-\mathbf{k}',\omega-\omega') = -L_N^{-1}(\mathbf{n}\cdot\mathbf{u}_1(\mathbf{k},\omega)) - \mathrm{i}\beta_i \mathbf{k}(\mathbf{u}_1\times\mathbf{b}). \qquad (4)$$

The convolution term on the LHS of (4) represents the contribution of mode interactions in the process of plasma fluctuation generation. If we take it into account phenomenologically through the coefficient of turbulent diffusion D_t, then (4) becomes

$$\delta N(\mathbf{k},\omega) = (-L_N^{-1}\mathbf{n} - \mathrm{i}\beta_i(\mathbf{b}\times\mathbf{k}))\,(\tau_d^{-1} + \tau_t^{-1} - \mathrm{i}\omega)^{-1}\cdot\mathbf{u}_1(\mathbf{k},\omega), \qquad (5)$$

where $\tau_d^{-1} = D_A k^2$, $\tau_t^{-1} = D_t k^2$.

Using relations: $\langle u_{1i}(\mathbf{k},\omega)\, u_{1j}^*(\mathbf{k}',\omega')\rangle = \Phi_{ij}(\mathbf{k},\omega)\,\delta(\mathbf{k}-\mathbf{k}')\delta(\omega-\omega')$, and $\langle \delta N(\mathbf{k},\omega)\,\delta N^*(\mathbf{k}',\omega')\rangle = \Psi(\mathbf{k},\omega)\,\delta(\mathbf{k}-\mathbf{k}')\delta(\omega-\omega')$, known for statistically homogeneous and stationary random fields, and the spectrum tensor of the turbulent velocity field in the form

$$\Phi_{ij}(\mathbf{k},\omega) = (\delta_{ij} - k_i k_j/k^2)\,[4\pi^2 k^2 \tau_k(\omega^2 + \tau_k^2)]^{-1} E(k) \qquad (6)$$

($E(k) = C_1 \varepsilon^{2/3} k^{-5/3}$, the energy spectrum function in the inertial range of wavenumbers, $k_0 < k < k_\mu$, k_0^{-1} is the basic energy input scale, $k_\mu^{-1} \approx (\mu_n^3 \varepsilon^{-1})^{1/4}$ is a viscous length-scale at which viscous dissipation is adequate to dissipate the energy at the rate ε, μ_n is the kinematic viscosity of neutral gas; $\tau_k^{-1} = \tau_t^{-1} + \tau_\mu^{-1}$, in the inertial range $\tau_t^{-1} \approx \varepsilon^{1/3} k^{2/3}$, $\tau_\mu^{-1} = \mu_n k^2 \approx \tau_d^{-1}$, because in our case $D_A \approx \mu_n$), and taking (5) into account, we obtain an expression for the space-time fluctuation spectrum:

$$\Psi(\mathbf{k},\omega) = \frac{(L_N^{-2} k^{-2} (\mathbf{n}\times\mathbf{k})^2 + \beta_i^2 (\mathbf{b}\times\mathbf{k})^2)\tau_k^{-1} E(k)}{(\omega^2 + (\tau_d^{-1} + \tau_t^{-1})^2)(\omega^2 + \tau_k^{-2}) 4\pi^2 k^2}. \qquad (7)$$

The spatial spectrum of plasma fluctuations $S(\mathbf{k})$ is related with $\Psi(\mathbf{k},\omega)$ as $S(\mathbf{k}) = \int_{-\infty}^{\infty} \mathrm{d}\omega\, \Psi(\mathbf{k},\omega)$. After integration, we have

$$S(\mathbf{k}) = (L_N^{-2} k^{-2} (\mathbf{n}\times\mathbf{k})^2 + \beta_i^2 (\mathbf{b}\times\mathbf{k})^2)(4\pi k^2 \Omega_k)^{-1} E(k), \qquad (8)$$

where $\Omega_k = (\tau_d^{-1} + \tau_t^{-1})(\tau_d^{-1} + \tau_t^{-1} + \tau_k^{-1})$. Using (8) we may obtain the rms level of plasma fluctuations: $\langle(\delta N)^2\rangle^{1/2} = \langle(N_1/N_0)^2\rangle^{1/2} = (\int \mathrm{d}\mathbf{k}\, S(\mathbf{k}))^{1/2}$, the integration over the surface of the sphere of radius k in **k**-space then gives

$$\langle(\delta N)^2\rangle = \int_{k_1}^{k_2} S_0(k)\,\mathrm{d}k, \tag{9}$$

where

$$S_0(k) = \frac{2}{3}\,(L_N^{-2} + \beta_i^2 k^2)\,\Omega_k^{-1} E(k) \tag{10}$$

($S_0(k)$ is the 1D omnidirectional spectrum of the fluctuations).

To estimate the level of relative fluctuations in plasma density (9) and the shape of the spectrum (10) expected in the lower atmosphere, we take the following values of parameters: B= 2 gauss, $L_N \approx L_g \sim 10^6$ m, $\varepsilon \approx u_g^3/L_g \sim 10^3\,\mathrm{m^2 s^{-3}}$ ($u_g \sim 10^3\mathrm{m\,s^{-1}}$ is the velocity associated with granulation of the scale L_g), other relevant values are listed in Table 1.

Table 1: Height dependence of D_A, β_i, k_μ^{-1}, and $\langle(\delta N)^2\rangle^{1/2}$

h, km	$D_A \approx \mu_n$, $\mathrm{m^2s^{-1}}$	$\beta_i = \omega_{Bi}/\nu_i$	k_μ^{-1}, m	$\langle(\delta N)^2\rangle^{1/2}$, %
250	2.4	3.5×10^{-5}	0.34	~ 4.1
515	24.5	4.4×10^{-4}	2	~ 4.1
705	194.6	6.9×10^{-3}	9.3	~ 4.2

The calculations of β_i and D_A were based on the books by Dungey (1958) and Lifshitz & Pitaevskii (1979) as well as on the model data for the solar atmosphere of Krinberg (1971) and Vernazza et al. (1981). The level of the fluctuations, $\langle(\delta N)^2\rangle^{1/2}$, was estimated for wavenumber range $k_m \le k \le k_\mu$ ($k_m = 10^{-5}\,\mathrm{m^{-1}}$).

It is seen from Table 1 that the level of electron-density fluctuations induced by turbulent mixing of weakly-ionized plasma in the solar atmosphere has to be almost unchanged with increasing the height. Figure 1 represents normalized 1D spectra of the fluctuations, $S_0(k)/S_0(k_m)$, obtained with the use of (10), for 3 levels in the atmosphere: 250 km, 515 km, 705 km; the dashed line shows the slope of the Kolmogorov spectrum, $k^{-5/3}$. The spectral form predicted by (10) changes with changing the altitude. These changes result from the height dependence of the ratio ω_{Bi}/ν_i, and of values of the coefficients μ_n and D_A.

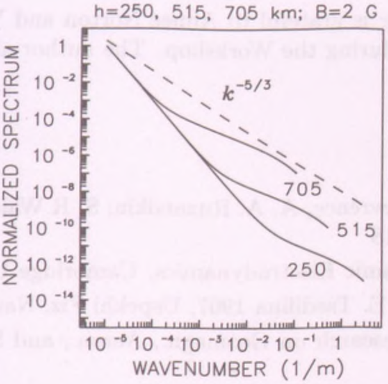

Figure 1: Normalized 1D spectra of plasma fluctuations expected in the solar atmosphere at heights: 250, 515, 705 km.

3. Conclusions

In this work an expression for the spectrum of small-scale electron-density fluctuations, which may be generated in the turbulent flow of weakly-ionized gas in the solar atmosphere has been obtained. The expression shows that the spatial 1D spectrum is close to the power-law dependence, but some its departures from a simple power law may exist. An expected rms level of relative plasma fluctuations was estimated. Under the usual conditions for the quiet atmosphere this level is about 4% for wavenumbers, $k_m \leq k \leq k_\mu$, corresponding to the inertial range of turbulence. If the intensity of turbulence and the length-scale of mean plasma-density gradient is height independent, then the fluctuation level must be nearly unchanged with altitude. However, because of changes in the ratio of the ion gyrofrequency to the ion-neutral collision frequency and in the coefficients of the ambipolar diffusion and kinematic viscosity with height, the shape of the 1D spectrum has to vary with a change in the height.

Acknowledgments

Presentation of this work at the NATO Advanced Research Workshop "Turbulence, Waves, and Instabilities in the Solar Plasma" in Budapest, 16-20 September 2002, was possible due to the support kindly given by the Organizing Committee of the Workshop. The author would like to thank Co-Directors of the Workshop, Robert von Fay-Siebenburgen and Kristof Petrovay, and the Organizing Committee for the help and support. The author is grateful to Aimee Norton and Yuriy Voitenko for useful and fruitful discussions during the Workshop. The author also thanks the referee for helpful comments.

References

Cadavid, A. C., J. K. Lawrence, A. A. Ruzmaikin, S. R.Walton, and T. Tarbell 1998, *Astrophys. J.* , 509, 918

Dungey, J. W. 1958, Cosmic Electrodynamics, Cambridge Univ. Press, Cambridge

Gurevich, A. V., and E. E. Tsedilina 1967, Uspekhi Fiz. Nauk (in Russian), 91, 609

Krinberg, I. A. 1971, Research on Geomagn., Aeron., and Solar Phys. (in Russian), 16, 141

Lifshitz, E. M., and L. P. Pitaevskii 1979, Course of Theoretical Physics, Vol.10. Physical Kinetics, Nauka, Moscow

Norton, A. A., and R. K. Ulrich 2000, Solar Phys., 192, 403

Vernazza, J. E., E. H. Avrett, and R. Loeser 1981, *ApJS* , 45, 635

PART THREE

PARKER INSTABILITY AND FLUX TUBE DYNAMICS

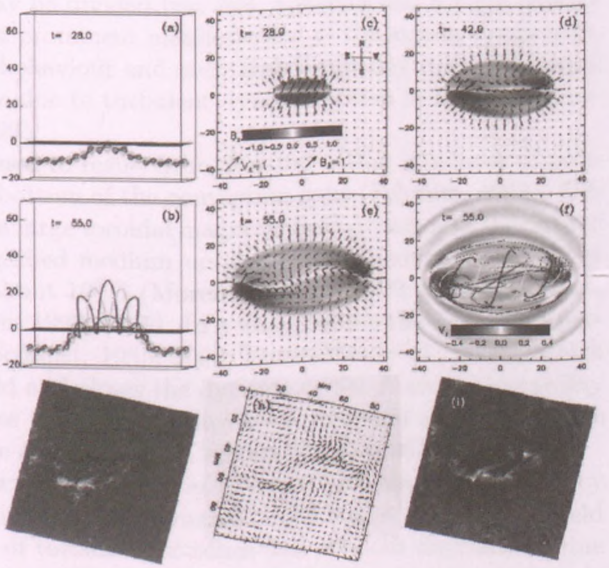

VARIABLE SOLAR AND STELLAR ACTIVITY BY A FLUX TUBE DYNAMO

D. Schmitt[1] **and A. Ferriz-Mas**[2]
[1]Max-Planck-Institut für Aeronomie
D-37191 Katlenburg-Lindau, Germany
[2]Universidad de Vigo
Facultad de Ciencias de Orense, E-32004 Orense, Spain
E-mail: [1]`schmitt@linmpi.mpg.de`, [2]`antonio.ferriz@oulu.fi`

Abstract

The dynamo action of unstable magnetic flux tubes due to magnetic buoyancy in a rotating stellar convection zone is summarized and the implications of a flux tube dynamo with a threshold in field strength for dynamo action is discussed in connection with the observed variability of solar and stellar magnetic activity.

KEYWORDS: *Sun, stars, magnetic activity, dynamo, stability, MHD*

1. Introduction

The solar magnetic field may be divided into two, a strong and a weak component. Sunspots are the most prominent manifestation of the strong component. They show a regular cyclic behaviour and obey Hale's polarity rules. The weak field is irregular and may be due to turbulent dynamo action in the upper convection zone (Cattaneo, 1999).

The strong field is assumed to result from dynamo action in a layer of overshooting convection at the bottom of the convection zone (Schmitt, 1993). Differential rotation builds up a large toroidal magnetic field, which is stably stored in the subadiabatically stratified medium until magnetic buoyancy instability sets in for strong fields of about 10^5 G (Moreno-Insertis, 1992; Schüssler et al., 1994; Ferriz-Mas & Schüssler, 1993, 1995). In a weak regime the instability provides a dynamic α-effect (Schmitt, 1985, 2003; Ferriz-Mas et al., 1994), which regenerates the poloidal field and closes the dynamo cycle. A strong instability leads to the rise of flux tubes through the convection zone and accounts for the bipolar active regions at the solar surface (Caligari et al., 1995).

In the following we discuss the dynamo effect of the magnetic buoyancy instability and its implications for the dynamo. The lower threshold in field strength for the instability of toroidal flux tubes and random fluctuations due to magnetic fields from the turbulent convection zone leads to strong amplitude

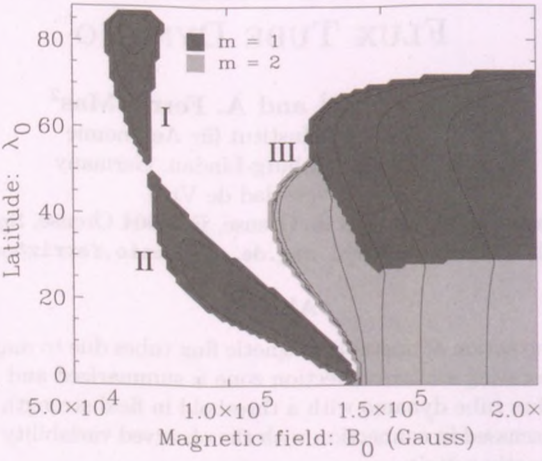

Figure 1: Stability diagram for toroidal flux tubes in the solar overshoot region. The shaded regions denote instability; the degree of shading indicates the azimuthal wavenumber of the mode with the largest growth rate.

variations and the appearance of grand minima (Schmitt et al., 1996; Schüssler et al., 1997; Schmitt et al., 1998), resembling the long-term behaviour of solar and the various kinds of stellar magnetic activity.

2. Dynamo action of magnetic buoyancy

Intense magnetic flux tubes can be stored in mechanical equilibrium in the stably stratified overshoot region at the bottom of the convection zone, while their field strength is increased by differential rotation (the overshoot region is a layer of strong shear) or by other mechanisms (Moreno-Insertis et al., 1995; Rempel & Schüssler, 2001). Once the field strength exceeds a critical value, which depends on stratification, latitude and angular velocity distribution, a buoyancy instability sets in. For details see Ferriz-Mas & Schüssler (1993, 1995). In Figure 1 a stability diagram is shown for flux tubes originating within the overshoot region.

The weak instability of region II of Figure 1, with growth times larger than 1 year, results from the combined effect of buoyancy instability and Coriolis force. This instability gives rise to helical waves of growing amplitude, which

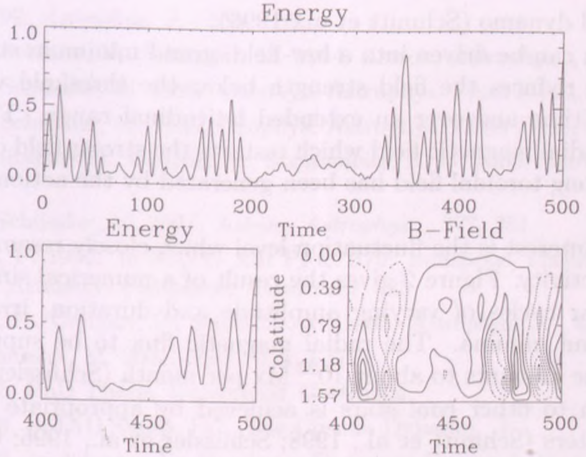

Figure 2: Long term evolution of dynamo activity. The top panel shows the total magnetic energy (in arbitrary units) as a function of time (in years). The lower panel shows a 100-year interval together with the corresponding butterfly diagram.

propagate along the tube and produce an inductive effect (α-effect) regenerating poloidal field from toroidal field. For flux tubes the dynamo effect is discussed in detail in Ferriz-Mas et al. (1994), for a continuous magnetic field details are given in Schmitt (2003). Since only nonaxisymmetric and unstable modes yield a net α-effect, strong magnetic fields are required, for below a threshold the toroidal flux tubes are stable.

Once the field becomes even larger, a second regime of instability is reached (region III on the diagram), with much smaller growth times. This instability drives the flux tubes into the convection zone proper and leads to the rise of unstable loops to the photosphere within about 1 month (Caligari et al., 1995).

3. Dynamo model and results

We propose a model of a strong-field dynamo working in the overshoot region with super-equipartition fields which is responsible for the activity cycle of bipolar regions. This dynamo is modelled with a simple 1D $\alpha\Omega$-mean field approach (Schmitt & Schüssler, 1989). The α-effect is due to tube instability and works only in the range $B_1 \leq B \leq B_2$. Convective downdrafts transport threads of magnetic flux, originating from a turbulent convection zone dynamo, into the overshoot layer. This effect is described as a stochastically varying source for the strong-field dynamo (Schmitt et al., 1996).

The system can be driven into a low-field, grand minimum state if the fluctuating source reduces the field strength below the threshold value B_1 for a sufficient long time and over an extended latitudinal range. The source also provides the radial magnetic field which restarts the strong-field dynamo once a sufficiently strong toroidal field has been generated by the action of differential rotation.

Of special interest is the fluctuation level which closely resembles the variation of solar activity. Figure 2 gives the result of a numerical simulation which exhibits regular cycles of varying amplitude and duration, irregularly interrupted by grand minima. The radial magnetic flux to be supplied from the convection zone amounts to about 10^{22} Mx per month (Schüssler et al., 1997).

Application to other cool stars is achieved by appropriate change of the stellar parameters (Schmitt et al., 1998; Schüssler et al., 1996; Granzer et al., 2000; Holzwarth & Schüssler, 2001).

4. Discussion

The picture of two mutually interacting hydromagnetic dynamos, a strong-field dynamo in the overshoot region based on the dynamo action of unstable magnetic flux tubes and a turbulent weak-field dynamo in the convection zone, leads to solar activity cycles with strong amplitude variations and the occasional appearance of grand minima, in qualitative agreement with the long-term record of solar magnetic activity.

Stronger fluctuations may destroy the cyclic behaviour of the overshoot layer dynamo and lead to increased but irregular activity (Schmitt et al., 1998), as is observed in fast rotating cool stars. On the other hand, stars with low and nonvariable magnetic activity may be in a state with only the turbulent convection zone dynamo active.

Acknowledgments

The work of A. Ferriz-Mas has been supported by the Spanish *Ministerio de Ciencia y Tecnología* under Project **AYA 2000-1691**.

References

Caligari, P., Moreno-Insertis, F., Schüssler, M. 1995, *Astrophys. J.* , 441, 886

Cattaneo, F. 1999, *Astrophys. J.* , 515, L39

Ferriz-Mas, A., Schmitt, D., Schüssler, M. 1994, *Astron. Astrophys.* , 289, 949

Ferriz-Mas, A., Schüssler, M. 1993, Geophys. Astrophys. Fluid Dyn., 72, 209

Ferriz-Mas, A., Schüssler, M. 1995, Geophys. Astrophys. Fluid Dyn., 81, 233

Granzer, T., Schüssler, M., Caligari, P., Strassmeier, K. G. 2000, *Astron. Astrophys.* , 355, 1087

Holzwarth, V., Schüssler, M. 2001, *Astron. Astrophys.* , 377, 251

Moreno-Insertis, F. 1992, in NATO ASI Proc. 375: Sunspots. Theory and Observations, Kluwer Academic Publishers, Dordrecht, 385

Moreno-Insertis, F., Caligari, P., Schüssler, M. 1995, *Astrophys. J.* , 452, 894

Rempel, M., Schüssler, M. 2001, *ApJ* , 552, L171

Schmitt, D. 1985, PhD Thesis, Universität Göttingen

Schmitt, D. 1993, in IAU Symp. 157: The Cosmic Dynamo, 1

Schmitt, D. 2003, in Advances in Nonlinear Dynamos, Taylor & Francis, 83

Schmitt, D., Schüssler, M. 1989, *Astron. Astrophys.* , 223, 343

Schmitt, D., Schüssler, M., Ferriz-Mas, A. 1996, *Astron. Astrophys.* , 311, L1

Schmitt, D., Schüssler, M., Ferriz-Mas, A. 1998, in ASP Conf. Ser. 154: Cool Stars, Stellar Systems, and the Sun, Vol. 10, 1324

Schüssler, M., Caligari, P., Ferriz-Mas, A., Moreno-Insertis, F. 1994, *Astron. Astrophys.* , 281, L69

Schüssler, M., Caligari, P., Ferriz-Mas, A., Solanki, S. K., Stix, M. 1996, *Astron. Astrophys.* , 314, 503

Schüssler, M., Schmitt, D., Ferriz-Mas, A. 1997, in ASP Conf. Ser. 118: 1st Advances in Solar Physics Euroconference. Advances in Physics of Sunspots, 39

ON THE ORIENTATIONAL RELAXATION OF BIPOLAR ACTIVE REGIONS

L. Tóth[1] and O. Gerlei[2]
Heliophysical Observatory of the Hungarian Academy of Sciences
H-4010 Debrecen, P.O.Box 30., Hungary
E-mail: [1]`tothla@tigris.klte.hu`, [2]`gerlei@fenyi.sci.klte.hu`

Abstract

Our work on the basis of selected regular bipolar magnetic regions (BMRs) strengthens the assumption that the scatter of tilt angles of BMRs around Joy's law is determined by the convective turbulence. Furthermore, regular BMRs grouped by age do not show the phenomenon of toroidal relaxation, which may probably mean the disconnection of Ω-loops from the bottom of the convection zone.

KEYWORDS: *Sun, Ω-loop, convective turbulence, dinamic disconnection, tilt angle*

1. Introduction

It is assumed that the solar magnetic field originates in the dynamo operating in a stable layer at the base of the convection zone. According to dynamo models (Parker, 1955; Babcock, 1961; Leighton, 1964; Leighton, 1969) the initial poloidal field turns into toroidal because of differential rotation. The toroidal strands of this subjacent magnetic flux locally may come out of this stable layer and would rise through the convection zone as an Ω-loop. It is one of the possible phenomena that is responsible for the formation of BMRs.

The emerged flux tubes show Joy's law that means, in general, that the preceding (p) spots of BMRs are closer to the equator than the following ones (f). Thus the BMRs are inclined to the local latitudinal line by an angle, which increases with latitude (Hale et al., 1919) and is called tilt. One of the explanations for this phenomenon is to take the Coriolis force into account (Schmidt, 1968) that can twist the ascending flux loops so that it finally emerges at the surface with a tilt to the local latitudinal line (Wang & Sheely, 1989; Wang & Sheely, 1991; Howard, 1991; Howard, 1996a; Howard, 1996b; Sivaraman et al., 1999).

Later on, in the theoretical descriptions (D'Silva & Choudhuri, 1993; Longcope & Choudhuri, 2002) further effects, namely the role of convective turbulence and dynamic disconnection have been taken into account, which influence the rising flux loop. In the present article we investigate observational signatures of these processes.

2. Method of investigations

In our investigations we applied the data of Greenwich Photo-Heliographic Results (GPHR) concerning the 14^{th} solar cycle from 1901 to 1913 from which only those clearly aligned active regions (ARs) were taken into account of which longitudinal co-ordinates were not farther from the central meridian than 60 degree. The selection of the regular ARs was made on the basis of photospheric observations of the Haynald Observatory (Tóth et al., 2002) and it resulted in 3754 BMRs.

The tilt angle (γ) is, by convention, positive for BMRs where p-spots are equatorward and negative if they are poleward of f-spots. Furthermore, this angle was calculated as the bend of a straight line to the local latitudinal line from which the first one was fitted by area weighted least-squares method to the spots of the given BMR. In accordance with Howard (1991) we applied latitudinal correction as well.

3. The distribution of tilt angle and its rotation

The distribution of tilt angles (γ) of BMRs over 5 degree increments is shown and compared with other results (Howard, 1996b; Sivaraman et al., 1999) in Figure 1 where the Kodaikanal and the Mount-Wilson data are basically the same but differ from our result. Due to the above-mentioned selection of regular BMRs our peak is more narrow than the others and apart from the small differences at it's wings follow the Gaussian distribution well.

Further information is obtainable from the distribution of the daily tilt angle changes of BMRs, which according to Howard (1994) were determined as simple day to day differences ($\omega = \Delta\gamma/\Delta\text{day}$). The distribution of them over 2 degree increments is shown in Figure 1, which is for the same reason as mentioned before narrower than that of the others'. Of special interest is the fact that it follows the Lorentzian distribution well.

The peak positions and the half-widths of our fitted Gaussian (γ_0, σ) and Lorentzian (ω_0, Γ) curves for the whole and the different age BMRs are compared with the theoretical results of Longcope & Choudhuri (2002) in Table 1. Our results show that the average tilt (γ_0) of BMRs is close to the mean angle determined by Joy's law and it slightly decreases as the BMRs are growing old.

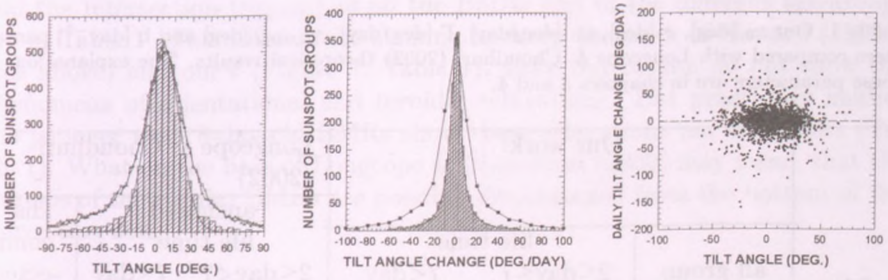

Figure 1: *Left:* The distribution of tilt angles (γ). The striped columns show our results that are based on the selected regular BMRs of the 14^{th} solar cycle (1901-1913). The solid line is a Gaussian curve fitted by the least-squares method applied to our data. The open circles represent the Kodaikanal (1906-1987) while triangles the Mount Wilson data (1917-1985) (Sivaraman et al., 1999) normalised to our results. *Center:* The distribution of the daily tilt angle changes (ω). The striped columns show our result and the solid line is a Lorentzian curve fitted by the least-squares method applied to our data. The black squares with solid line represent the Mount Wilson data (Howard, 1994) normalised to our result. *Right:* The plot ω versus γ of our selected regular BMRs and the straight line fitted by the least-squares method to its points (dashed line)

Moreover, the average rotational velocity (ω_0), though to a less degree, but is larger than zero, but tends to disappear as BMRs are growing old.

4. The role of dynamic disconnection

Howard (1996a) made first a plot of ω against γ that shows a relation between the tilt angle and its change, and fitted them with a straight line as ω = a+b$*\gamma$. This fitting (Howard, 1996a) resulted in the slope as b = -0.229±0.004 and the location of the intersection of the γ axis at $\gamma_{(\omega=0)}$ = 5.65±0.32 degree that is close to the angle γ_0 determined by Howard (1996b) (γ_0= 4.28±0.19), Sivaraman et al. (1999) (γ_0= 4.2) and this article (γ_0= 5.8±0.3, Table 1). This lead to the conclusion that the bipoles relax from their orientation toward the angle γ_0 specified by Joy's law. This phenomenon is called orientational relaxation. On the bases of Howard (1996a) work Longcope & Choudhuri (2002) gives an overall theoretical description of this phenomenon. In their theories they took into account the effect of the Coriolis force on the rising flux tube as the origin of Joy's law, and the effect of the convective turbulence as being responsible for the random scatter of tilts around the systemic ones determined by Joy's law. This assumption is proved by our results since the measured tilt angles follow

Table 1: Our γ_0 [deg], σ [deg], ω_0 [deg/day], Γ [deg/day], $\gamma_{(\omega=0)}$ [deg] and b [day^{-1}] parameters compared with Longcope & Choudhuri (2002) theoretical results. The explanations of these parameters are in chapters 3 and 4.

	Our work:			Longcope & Choudhuri (2002)		
		life time:		anchored life time:		dis-conn-ected
	all group	2≤day≤7	7<day	2≤day<7	7≤day	
γ_0	5.8±0.3	5.5±0.3	4.8±0.4	3.71	2.43	4.05
σ	13.5±0.3	13.0±0.3	12.2±0.4	-	-	-
ω_0	0.32±0.06	0.35±0.06	0.12±0.09	-	-	-
Γ	11.0±0.2	11.4±0.2	8.3±0.3	-	-	-
$\gamma_{(\omega=0)}$	21±30	18±18	9±16	3.3	-0.03	2.12
b	-0.02±0.02	-0.03±0.02	0.07±0.07	-0.302	-0.097	-0.024

Gaussian distribution (Figure 1), which seems to describe the distribution of random observations. Consequently, we assume that there must be a connection between the half-with of the tilt angle distribution (σ in Table 1) and the scale of convective turbulence as well.

Furthermore, there is a question, which gains importance, whether the rising Ω-loop is connected to the bottom of the convection zone or not. The last case is called dynamic disconnection. Namely, if the flux tube is connected to the strong toroidal magnetic field at the bottom of the convection zone then following the emergence, the magnetic tension with the progress of time may force to align the bipolar magnetic region toward the east-west direction. That is, the above-mentioned slope (b) and the intersection ($\gamma_{(\omega=0)}$) with the progress of time may keep to 0, that kind of behavior is called toroidal relaxation. But if the flux tube were dynamically disconnected, this relaxation to zero tilt would stop. Considering this Longcope & Choudhuri (2002) calculated artificial ω-γ plots for the younger and the older than 7-day-old Ω-loops, in cases when they are connected to or disconnected at 75 Mm below the solar surface from the bottom of the convection zone. The parameters of the straight lines fitted to these artificial plots are visible in Table 1.

Based on our selected, clearly aligned BMRs, we have investigated the distributions of the related ω and γ pairs for all and for BMRs of different age-groups as well. The plot of all selected BMRs with the fitted straight line to its points is in Figure 1. The parameters of the fitted straight lines, namely the slope (b), and the intersection ($\gamma_{(\omega=0)}$) of all the BMRs and of the different age-groups are in Table 1. The difference is striking between the work of Howard (1996a) (see above) and our's (Figure 1, Table 1), since our results do not show the phenomena of orientational and toroidal relaxations. But practically neither the younger than 8-day-old BMRs show these relaxations nor the olders (Table 1). What on the base of Longcope & Choudhuri (2002) may mean, that the Ω-loops of the regular BMRs are possibly disconnected from the bottom of the convection zone.

5. Conclusions

First of all, we can claim that the selection of the clearly aligned BMRs lead to the reduction of several error sources and gave new results.

The distributions of the tilt angles of BMRs and their rotations agree with other results well, and show that the average alignment (γ_0) determined by Joy's law just as its near zero average rotational velocity (ω_0) slightly decreasing as the active regions are growing old.

The Gaussian shape of the tilt angle distribution is in agreement with the assumption that the scattering of the tilt around the Joy's law determined systemic ones is caused by random-like convective turbulence.

Furthermore, the regular, clearly aligned active regions do not show the phenomenon of toroidal relaxation, which may mean that the Ω-loops are presumably disconnected from the bottom of the convection zone.

Acknowledgments

We would like to say thank to Pascal Demoulin and Lidia van Driel-Gesztelyi for their creative remarks and for the encouragement coming from Arnab Rai Chudhuri and Valentine I. Makarov. This work was supported by the Hungarian National Science Foundation (OTKA: F030957).

References

Babcock, H. W. 1961, *Astrophys. J.* , 133, 572

D'Silva, S., Choudhuri, A. R. 1993, A&A, 272, 621

Hale, G. E., Ellerman, F., Nicolson, S. B., Joy, A. H. 1919, *Astrophys. J.* , 49, 153

Howard, R. F. 1991, Solar Phys., 132, 49

Howard, R. F. 1994, Solar Phys., 149, 23

Howard, R. F. 1996a, Solar Phys., 167, 95

Howard, R. F. 1996b, Solar Phys., 169, 213

Leighton, R. B. 1964, *Astrophys. J.* , 140, 1547

Leighton, R. B. 1969, *Astrophys. J.* , 156, 1

Longcope, D., Choudhuri, A. R. 2002, Solar Phys., 205, 63

Parker, E. N. 1955, *Astrophys. J.* , 122, 293

Schmidt, H. U. 1968, in K. O. Kiepenheuer (ed.), Sructure and Development of Solar Active Regions, D. Reider Publ. Comp., p. 95

Sivaraman, K. R., Gupta, S. S., Howard, R. F. 1999, Solar Phys., 189, 69

Tóth, L., Mező, G., Gerlei, O. 2002, J. Hist. Astr., 33, 278

Wang, Y. M., Sheely, N. R. 1989, Solar Phys., 124, 81

Wang, Y. M., Sheely, N. R. 1991, *Astrophys. J.* , 375, 761

DYNAMICS OF THIN FLUX TUBES IN SUNSPOT PENUMBRAE

K. Jahn
Warsaw University Observatory
Al. Ujazdowskie 4, 00-478 Warsaw, Poland
E-mail: `crj@astrouw.edu.pl`

Abstract

A model for the fine structure of a sunspot penumbra can be constructed in a form of an ensemble of magnetic flux tubes moving in their own background. As a first step the evolution of a single flux tube in a penumbra of the magnetostatic sunspot model is studied numerically. Properties of such solutions are briefly recalled and some of new results are presented with a qualitative discussion of dynamic features of emerging tubes as compared with the observed behaviour of bright penumbral grains. Limitations of the model and problems related to a quantitative comparison with observations are also commented.

KEYWORDS: *Sunspots, penumbrae, magnetic flux tubes*

1. Introduction

Sunspot penumbrae observed at high spatial resolution exhibit a very complex filamentary structure which changes continuously on dynamical time scales. Short living bright and dark fibrils together with bright penumbral grains migrating inwards and outwards are responsible for azimuthal inhomogeneity of all measured parameters, i.e. field strength, its inclination, light intensity, and velocity field. For exhaustive discussion of the penumbral structure and its dynamics see the reviews of Thomas & Weiss (1992) and Maltby (1997).

The known picture of the penumbrae strongly suggests that their fine structure and dynamics are a manifestation of a convective process occurring in an inclined magnetic field which extends deep below the photosphere. Theoretical modelling of such a process is required to understand both: complex behaviour of the fine structure at the surface, and a global nature of a penumbra with the energy transport which is responsible for a very small (of 5% only) variation of the mean brightness between the inner and the outer edge. Direct numerical simulations of penumbral convection are very demanding because they should describe not only deep layers but also the photosphere, which is a shallow layer of transition from adiabatic to radiative regime in which plasma β is close to unity. Moreover, it seems impossible at present to cover the full range of scales which are necessary to describe the fine structure of the penumbra. Note, that recent observations indicate extreme narrowness of bright filaments (about 0.″35 or less), and most probably the true structure of magnetic elements has not yet been resolved (e.g. Sütterlin, 2001). Nevertheless, such attempts have been made and the obtained results shed some light on properties of magnetoconvection in an inclined magnetic field (Hurlburt & Rucklidge, 2000; see also Hurlburt, this conference).

Here, I would like to discuss another approach to describe the penumbral structure. The approach based on the concept of interchange convection – a conjecture proposed on the basis of high resolution observations of penumbral fine structure and its dynamics confronted with global models of sunspots (Jahn & Schmidt, 1994). In this picture bright penumbral filaments are inclined magnetic flux tubes or rather narrow flux sheets that emerge in the photosphere bringing to the surface hot material from deep layers. The following Section contains: a brief summary of properties of computed models, qualitative discussion of dynamics of flux tubes emerging in the penumbra, and a few comments on limitations of the model and on some problems related to a quantitative comparison with observations.

2. Evolution of a flux tube in the penumbra

The description of the model and physical properties of evolving flux tubes was discussed in detail by Schlichenmaier, Jahn & Schmidt (1998), hereafter SJS. Below, I briefly comment the main features of the model.

We study the evolution and properties of a single convective element which is initially a part of the penumbra in the global magnetostatic model of a sunspot. We use a *simplifying* assumptions and approximate the structure of such a magnetic flux element by a 1-D thin flux tube (TFT), and neglect the magnetic diffusion assuming and ideal MHD. That limits the range of size (or magnetic flux) of tubes which can be modelled. On one side, the size of the tube should be smaller than the local pressure height scale, which is of the order of 100 km in the photosphere. Otherwise the TFT breaks down. On the other side, due to a finite value of magnetic diffusivity η in the photosphere too narrow flux tubes are not described properly by the ideal MHD. Still acceptable would be a tube with a diameter of 5 km, for which the diffusion time scale is close to 5 hours and the magnetic Reynolds number is somewhat more than 3000 for the velocity of 1 km/s (the coefficient η is estimated according to Lang, 1999, for the temperature 6000K and the electron density 3×10^{13} cm^{-3}). It should be stated clearly that our models correspond to elements which cannot be observed directly on the Sun. Therefore, a quantitative comparison of physical parameters with observations is not trivial, but that concerns any model as long the true magnetic structure of the penumbra remains unresolved.

The main feature of our model is that the tube of the size of about 50 km, initially positioned at the magnetopause, rises through the deep penumbra and emerges in the photosphere, where it forms a horizontal channel containing an outflowing gas, i.e. the Evershed flow. The intersection of the tube with the photosphere migrates towards the umbra and contains an upflowing hot matter which gradually cools down as it flows outwards, which makes the tube more and more transparent. This picture closely resembles a bright penumbral grain (PG) with a "head" and a "cometary tail". It is also tempting to identify the extended tail of such a tube (one or more) with a single bright filament. Detailed analysis of properties of the tube shows the model is consistent with observations even when the velocities of the flow reach up to 14 km/s (see SJS).

It is worth-while to recall here another solution for a very thin flux tube, with a diameter of 10 km, which forms an arch above the photosphere of the penumbra (Jahn, Schlichenmaier & Schmidt, 1996). This "wave" migrates towards the umbra and the flow along the submerging part of the tube becomes supersonic at some stage of evolution. Perhaps, an ensemble of such tubes could account for the feature observed by del Toro Iniesta, Bellot Rubio & Collados (2001), i.e. a presence of supersonic downflow in the outer penumbra.

In recent years Schlichenmaier and coworkers carefully confronted the model with the observed properties of penumbral fine structure and flows. Summary of those findings together with an extensive discussion of observational peculiarities of the penumbra in the context of emerging flux tubes can be found in the review of Schlichenmaier (2002). Here, I would like to present a preliminary comment on some new simulations and concentrate the discussion on the dynamic features of the flux tubes evolving in the penumbra. Those features can be compared (at present, qualitatively only) with statistical properties of PGs studied by Sobotka, Brandt & Simon (1999) and Sobotka & Sütterlin (2001). Their analysis gives an additional possibility of verifying our model.

The simulations were performed with a code that slightly differs from the one used previously. The main difference is the description of the radiative heat exchange, which takes into account the fact that an optically thick flux tube loses or gains energy not with a whole volume but rather with a surface layer of a thickness depending on local opacity. The resulting heat exchange rate for the finite temperature difference lies between the inefficient Newton's cooling

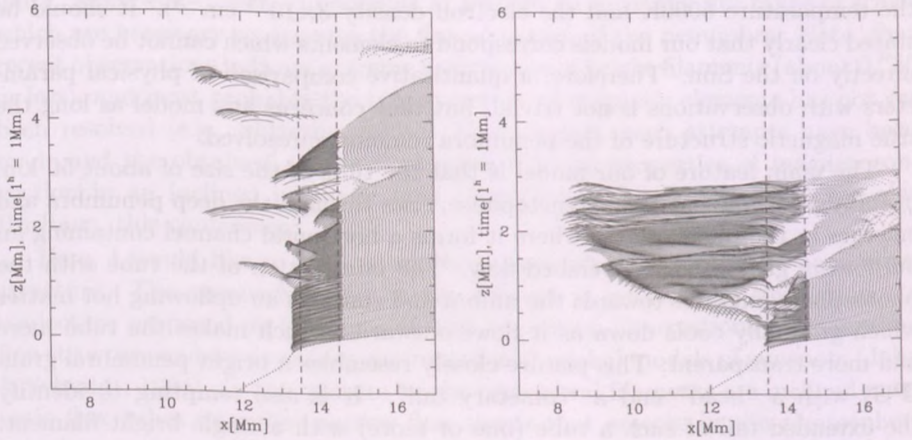

Figure 1: Shapes of tubes above the photosphere are plotted with 30^s cadence and a vertical shift such that 1 Mm corresponds to 1^h of evolution. Left – $\Phi = 10^{15}$Mx, right – $\Phi = 10^{16}$Mx. See text for details.

rate and the overestimated rate based on the difference between the bolometric Planck functions (see e.g. Kalkofen & Ulmschneider, 1977). More details will be published elsewhere (in preparation).

From a series of models two have been selected and shown in the Fig. 1. The magnetic flux Φ of the tubes is equal to 10^{15} and 10^{16} Mx (left and right plot respectively), so that the models correspond to the ones recalled above. Figure 1 shows the shape of flux tube only above the photosphere. It is drawn with continuous (dotted) line above the penumbra (quiet Sun). Curves are plotted with a 30^s cadence and shifted vertically so, that 1 Mm on the vertical scale corresponds to 1^h of the evolution. The initial shape of the tube (or a fragment of the magnetopause) is drawn down to -1 Mm. The transition from the penumbra to the quiet Sun is marked with the vertical dashed lines. This is the region of a "naked wall" (see Jahn & Schmidt, 1994).

The thinner flux tubes tube emerges in the photosphere several times. Each time it forms a PG which migrates initially inwards, but sometimes the phase of sinking proceeds in such a way that the grain moves outwards. Near, and in the region of the "naked wall" PGs move mostly toward the photosphere. Thus, most probably outward moving PGs correspond to the phase of sinking of flux tubes. In all computed models the grain is accompanied by a tail directed outwards. Therefore, it is not mysterious (as noted by Sobotka, Brandt & Simon, 1999) that also PGs moving outwards may have such a feature. It is rather the opposite direction of the tail (toward the umbra) that cannot be explained in this way. Velocities of migration of flux tubes (0.5–3 km/s) and the time they appear above the photosphere (10–30 min.) compare well with observations. Such an appearance of the tube at the surface may probably account for a transitory character of the Evershed effect (e.g. Shine et al., 1994). Note also, that the tube sinks outside the penumbra and forms a moving magnetic element in the quiet photosphere (MMF in the moat?). The behaviour of the thicker tube is similar to the model of SJS. Because of larger crossection it cools down less efficiently and penetrate further towards the umbra. However, there are here phases of the evolution when the tube dives below the surface in the outer penumbra. It is also difficult to find a longer time period during which the horizontal flow would become stationary.

The important feature of PGs, i.e. the dominating type of motion (inward and outward) in the inner and outer penumbra, cannot be discussed with a present set of models. We have no solution in which the tube would reach the umbra. The reason is most probably related to the initial conditions. The primary source of perturbation that sets the tube in motion is an abrupt heat exchange at the "naked wall". Thus, the grain starts the migration always at the magnetopause near the surface, and the larger the tube the further it moves inwards. The size of a tube that would survive a travel across the whole penumbra should be larger than allowed by the TFT. However, there is another type of natural perturbation in our model – part of the magnetopause at depth of 5-6 Mm is unstable to interchange. Some experiments indicate that tubes perturbed at those depths (with the upper perturbation artificially suppressed) have a tendency to appear first in the middle penumbra. Perhaps there exist two families of emerging tubes originating from different depths, but this possibility has not yet been studied in detail.

Somewhat surprising but also attractive consequence is suggested by our model: dark filaments do not exist *per se*. They would rather appear as a view of a darker background obscured by bright parts of emerging flux sheets. Then, the penumbral background would be almost the same as that of the umbra. Therefore, it would be interesting to investigate features of emerging tubes in a sunspot model surrounded by a single current sheet, or in a model of a pore.

The extreme narrowness of the single flux tubes models makes a quantitative comparison with observations rather difficult. An observable should be constructed, for instance a synthetic profile of a spectral line emitted from a region of a size corresponding to the observational resolution, and forming in an inhomogeneous volume which contains the tube(s) and the background with different temperatures, velocities, and the magnetic field. That requires a model of a penumbra with a fine structure. It can be constructed as an ensemble of evolving flux tubes of different sizes and in different phases of evolution, which is the main goal of the investigations presented here.

Acknowledgments

This work was supported by the KBN grant 5 P03D 00621.

References

del Toro Iniesta, J. C., Bellot Rubio, L. R & Collados, M. 2001, *Astrophys. J.* , 549, L139

Hurlburt, N. E. & Rucklidge, A. M. 2000, *Monthly Notices Roy. Astron. Soc.*, 314, 793

Jahn, K. & Schmidt, H. U. 1994, *Astron. Astrophys.* , 290, 295

Jahn, K., Schlichenmaier, R. & Schmidt, H. U. 1996, Ast. Lett. & Comm., 34, 59

Kalkofen, W. & Ulmschneider, P. 1977, *Astron. Astrophys.* , 57, 193

Lang, K. R. 1999, Astrophysical Formulae Vol. I, p. 210, Springer-Verlag

Maltby, P. 1997, in Advances in Physics of Sunspots, ASP Conf. Ser. 118, B. Schmieder, J. C. del Toro Iniesta & M. Vazquez (eds.), p. 91

Schlichenmaier, R. 2002, in Current Theoretical Models and Future High Res. Solar Observations, ASP Conf. Ser., A. A. Pevtson & H. Uitenbroek, in print

Schlichenmaier, R., Jahn, K. & Schmidt, H. U. 1998, *Astron. Astrophys.* , 337, 897

Shine, R. A., Title, A. M., Tarbell T. D., Smith, K., Frank, Z. A., & Scharmer G. 1994, *Astrophys. J.* , 430, 413

Sobotka, M., Brandt, P. N. & Simon, G. W. 1999, *Astron. Astrophys.* , 348, 621

Sobotka, M. & Sütterlin, P. 2001, *Astron. Astrophys.* , 380, 714

Sütterlin, P. 2001, *Astron. Astrophys.* , 374, L21

Thomas, J. H. & Weiss, N. O. 1992, in Sunspots: Theory and Observations, NATO ASIC Proc. 375, J. H. Thomas & N. O. Weiss (eds.), Kluwer, p. 3

PART FOUR

WAVES AND OSCILLATIONS IN THE SOLAR ATMOSPHERE

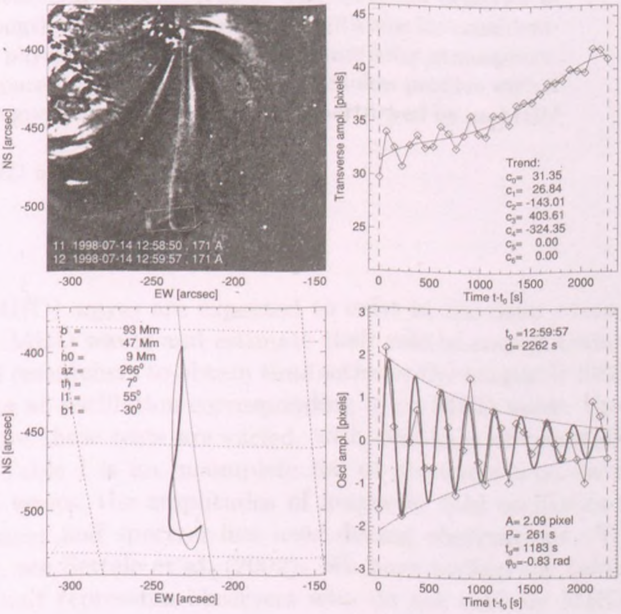

Observing MHD Oscillations in Sunspot: The Effects of Vertical Magnetic Gradients and Thermodynamic Fluctuations

A.A. Norton[1] and H. Uitenbroek[2]
[1]High Altitude Observatory
NCAR, PO Box 3000, Boulder, CO, 80307 USA
[2]National Solar Observatory
Sac Peak, PO Box 62, Sunspot, NM 88349 USA
E-mail: [1]`norton@ucar.edu`, [2]`huitenbroek@nso.edu`

Abstract

Attempts to detect magnetohydrodynamic waves in the solar photosphere by identifying oscillations in the magnetic field have proved problematic due to suspected contributions from systematic temperature and density fluctuations causing the spectral line formation height to vary, which in turn samples a vertical gradient in the magnetic field strength. We investigate this effect in sunspot umbrae and penumbrae through the analysis of data obtained with the Advanced Stokes Polarimeter in spectral lines with notoriously different temperature sensitivities. The temporal behavior of the magnetic field strength in sunspot is presented with special consideration to line formation physics occurring in the dynamic solar atmosphere. These results are compared to forward modeling of Stokes profiles with a radiative transfer code given a sunspot atmosphere perturbed by an MHD oscillation.

Keywords: *Sun, MHD waves, observations*

1. Introduction

Magnetohydrodynamic (MHD) waves are expected to exist in the solar atmosphere. A desire to detect MHD waves and estimate their role in energy transport has motivated several researchers to obtain time series of the magnetic field with the hope of measuring an oscillation corresponding to an MHD wave. Unfortunately, the results from these tests are varied, with problems of crosstalk of one kind or another. Table I is an incomplete list of observers who have conducted tests for MHD waves, the amplitudes of magnetic field oscillations measured and the instrument and spectral line used during observations. To view a more complete list, see Settele et al. (2002). We have broken the table in two parts: the upper half represents observers who do not exclude MHD waves as an interpretation, the lower half are those who believe the measured oscillations are due to crosstalk. Most of the observers concentrate solely on the dynamics of sunspots, which is also the focus of this paper.

One crosstalk mechanism, thought to be responsible for oscillations observed by Rüedi et al. (1998) and Bellot Rubio et al. (2000), intrigued us as a possible way to reconcile the conflicting reports and bring solar physics community closer to understanding the real amplitude of MHD waves. To understand this crosstalk mechanism, imagine that a magnetic field embedded in the solar atmosphere has a vertical gradient, d|B|/dz, such that the absolute value of the field strength is decreasing with height. Also imagine that there exist temperature and density perturbations (from an MHD or acoustic wave) which cause the effective height of formation of the spectral line to bob up and down in the atmosphere. That would cause an oscillation to be measured in the magnetic field which is not intrinsic to the MHD oscillation itself, but instead results from sampling at different heights for differing wave phase. This would show up even in a purely (field aligned) acoustic wave, which has no intrinsic magnetic oscillations itself.

We were inspired by Rüedi et al. (1999) who investigated the effect of vertical magnetic gradients on MDI data by simulating the NiI 6768 Å line with MHD perturbations for the center-of-gravity magnetogram method and MDI's modified center-of-gravity algorithm. They found that thermodynamic fluctuations alone (without a vertical gradient) gave rise to a magnetic flux density oscillation with the signature of (v, δ|B|)=90°. However, the introduction of a vertical gradient reversed this effect such that increasing gradients decreased the amplitude introduced by the thermodynamic crosstalk and eventually introduced an oscillation whose signature was (v, δ|B|)=−90°. We thought it was an important task to determine whether commonly used FeI lines and an inversion technique used by spectropolarimetric instruments sampled the vertical gradient in a similar fashion. A simple observational test could be done to estimate the thermodynamic fluctuations.

Our intention for this research was to observe with spectral lines of notoriously different thermodynamic sensitivities, assume a vertical magnetic gradient, and through the comparison of forward modeling with observations, place upper bounds on the thermodynamic perturbations present. In other words, if there are thermodynamic fluctuations, the temperature and density sensitive line will experience larger height of formation fluctuations than the insensitive line. Through forward modeling, height of formation variations could be calculated for both lines. Comparison of height of formation changes coupled with an assumed vertical gradient and the oscillation amplitudes present in observa-

Table 1: Incomplete List of MHD Wave Searches

	Amplitude	Instr.	Line (Å)
Ulrich, 1996*	2 Mx/cm^2	MWO	5896 NaD1
Horn et al., 1997	30 G	FPI	5250 Fe1
Norton et al., 1999*	18 Mx/cm^2	MDI	6768 NiI
Balthasar, 1999	40-70 G	FPI	6843 FeI
Settele et al., 2002	6 G	ASP	6302 FeI
Rüedi et al., 1998	6 Mx/cm^2	MDI	6768 NiI
Lites et al., 1998	4 G	ASP	6302 FeI
Bellot Rubio et al., 2000	4 G	TIP	15650 FeI

*Observations taken outside of sunspot.

tions, would allow an upper boundary to be placed on temperature and density perturbations.

2. Observations & Data Calibration

Two sets of observations were taken with the HAO/NSO Advanced Stokes Polarimeter (ASP: Elmore et al., 1992; see also Lites, 1996). The first dataset was a time series consisting of umbra, penumbra and plage of the active region NOAA9697 located at N14 W13 on 18 November 2001 from 14:27-16:09 UT. The slit was stepped across the region for ten steps each of 0.6″. The region scanned was 6″×85″. The FeI spectral line pair 6301/6302 Å was observed in channel A while the FeI 5147/5250 Å spectral line pair was observed in channel B simultaneously. The second dataset was a time series consisting of outer umbra, inner penumbra and some plage above the active region NOAA9866 located at S8 E56 on 10 Mar 2002 from 20:45-21:09 UT. The slit was stepped across the region for sixteen steps each of 0.37″. The region scanned was 6″×85″. The FeI spectral line pair 6301/6302 Å was observed in channel A while the NiI spectral line 6768 Å was observed in channel B simultaneously.

Calibration of the data was performed as described by Skumanich et al. (1997). Calibrated data were then inverted through the use of a 2-component (1 of them non-magnetic) Milne-Eddington (ME) atmosphere (Skumanich et al., 1987). Image motion between single scans was removed, when necessary, by obtaining a maximum correlation with a single good map of the signed in-

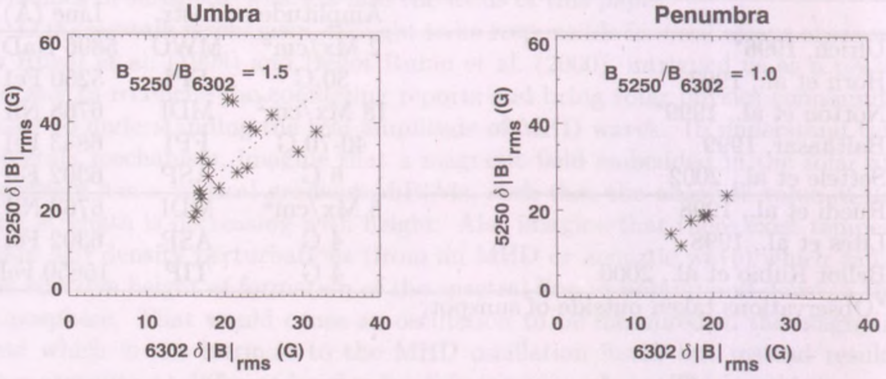

Figure 1: Comparison of field strength oscillation amplitudes as measured in umbra and penumbra with 6302/6301 & 5250/5147 Å line pairs.

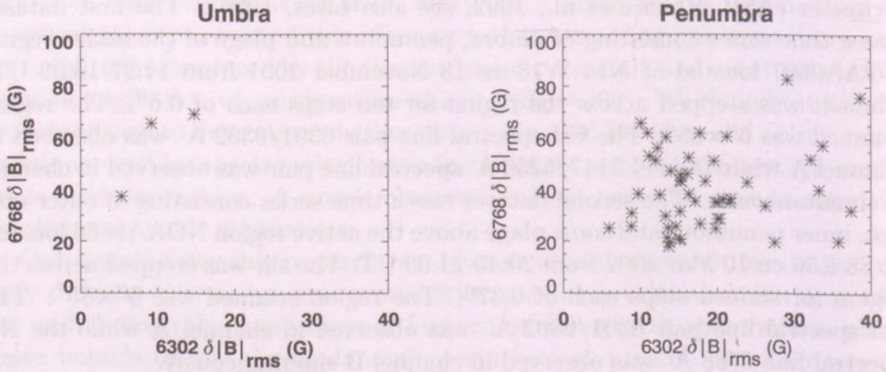

Figure 2: Comparison of field strength oscillation amplitudes as measured in umbra and penumbra with 6302/6301 Å line pair & 6768 Å spectral line.

tegrated Stokes V signal and shifting the data subpixel amounts through linear interpolation. Drifts in the data were removed through maximum correlation and bilinear interpolation of entire maps.

3. Observational Analysis & Results

Time series of magnetic field strength are interpolated onto an evenly sampled time grid. The data is detrended and power is calculated using a Fast Fourier Transform. No spatial averaging is used. The 2.5-4.5 mHz frequency is defined as the 5 minute band whereas noise is determined in the 7.0-8.3 mHz frequency bin. A statistical significance test is applied to the data according to Groth (1975) where a multiplicative of the mean noise level was used to determine if the power in the 5 minute band was at a 99% confidence limit. Only those spatial positions common to both spectral lines **and** containing significant power were then further analyzed. Only umbral and penumbral points were analyzed and these were done so separately. The reason for the separate analysis is that geometries and thermodynamics should vary significantly from umbra to penumbra and we wanted to limit the analysis to features whose physics are fundamentally similar. Again, for the 10 March 2002 data, only umbral and penumbral points were analyzed.

Fig 1 shows results for the simultaneous observations with FeI 5250/5147 Å and FeI 6302/6301 Å line pairs. The FeI 5250/5147 Å data shows RMS magnetic field amplitudes in umbra 1.5 times higher than those seen in FeI 6302/6301 Å data. This could be the result of larger fluctuations in spectral line formation heights of 5250 Å sampling the vertical gradient. Penumbral ratios of RMS magnetic field amplitudes are unity, signifying different physics occurring in penumbral structures than in umbra.

Seen in Fig 2, the NiI 6768 line shows RMS magnetic field amplitudes in umbra 10 times higher than those seen in FeI 6302/6301 line pair. However, so few data points in the umbra met the significance criteria that it is difficult to give credence to this result. Furthermore, the comparison of 6768 Å and 6302/6301 Å penumbral data shows the NiI 6768 Å results are dominated by noise. Therefore, the NiI 6768 Å data cannot be used conclusively. It must be considered that the Milne Eddington least squares inversion performs better with a spectral line pair than it does with a single line (Lites et al., 1994). Therefore, the larger RMS amplitudes are probably due to greater error in the 6768 inversion which uses a single spectral line as opposed to the 5250/5247 or 6302/6301 pair inversion.

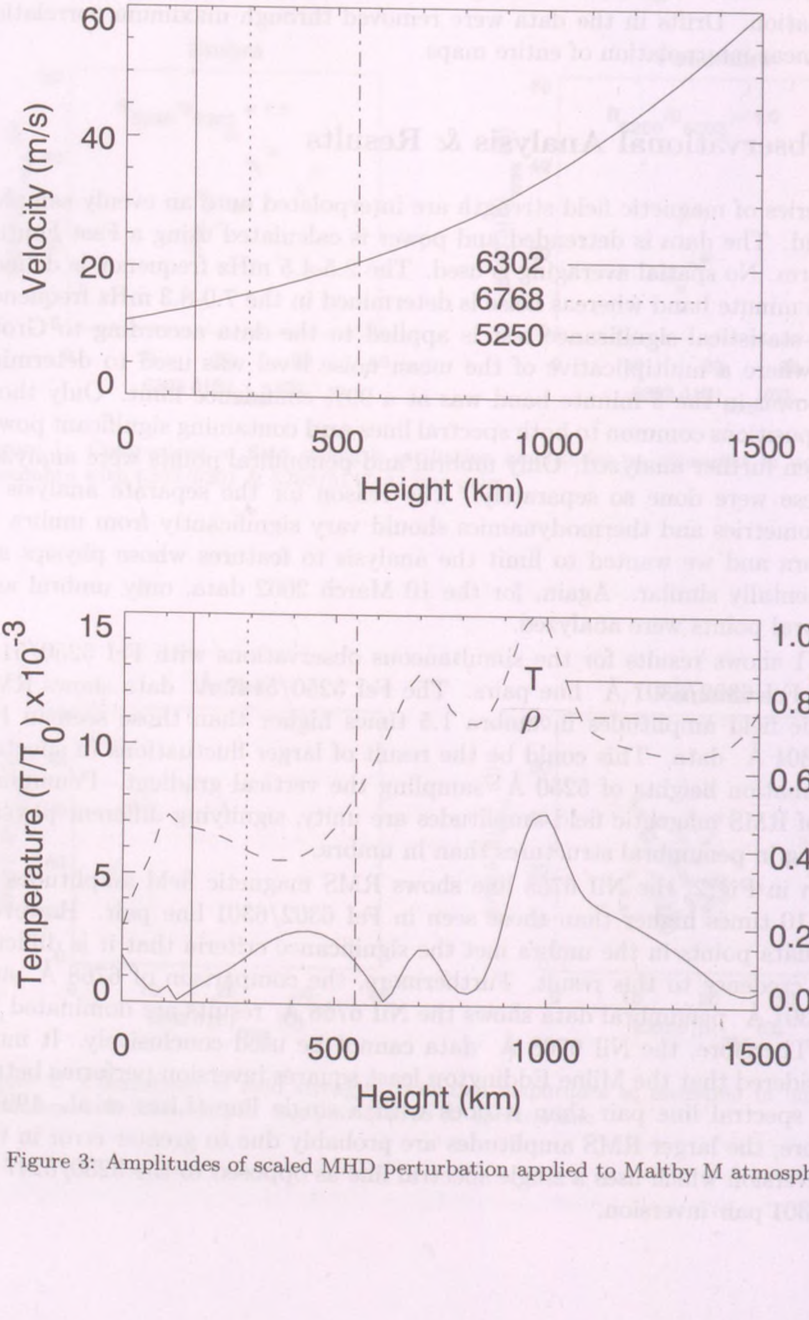

Figure 3: Amplitudes of scaled MHD perturbation applied to Maltby M atmosphere.

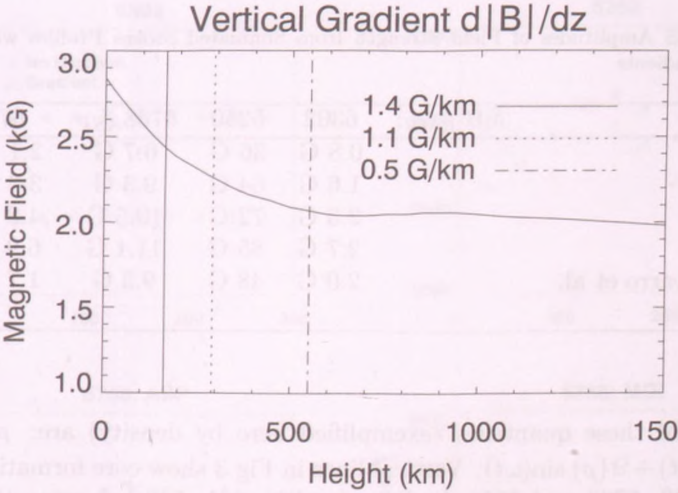

Figure 4: A vertical magnetic field gradient observed by Socas-Navarro et al. (2000) in a sunspot is used in conjunction with the Maltby-M umbral atmosphere to simulate Stokes profiles.

4. Forward Modeling Results

Stokes profiles were simulated using a non-LTE numerical radiative transfer code (Uitenbroek, 2001) based on the multilevel accelerated lambda iteration (MALI) formalism of Rybicki & Hummer (1991). All calculations were made in a 1-dimensional plane parallel geometry. The model atom used is a 23 level FeI atom. The oscillator strength of the 5250/5247 Å line was multiplied by three, to compensate for the population deficiency caused by overionization (Bruls et al., 1990).

A linear adiabatic wave of 3.33 mHz frequency (300 second period) was calculated as described by Cally et al. (1994). The model consists of three layers: a Maltby M model (Maltby et al., 1986) for $-122<z<2146$ km, an isentropic polytrope below and an isothermal corona (2×10^6 K) above, and was found to support a p_1 wave with horizontal wavenumber $1.96\times10^{-3}+6.18\times10^{-5}i$ km^{-1} (the imaginary part is due to spatial decay resulting from slow mode leakage). The perturbation amplitudes were scaled by ten times the original perturbation calculations in order to better match with observations. Maximum perturbation amplitudes as a function of height in the atmosphere are shown in Fig 3 for the vertical velocity, temperature and density perturbations. The temporal

Table 2: RMS Amplitudes of Field Strength from Simulated Stokes Profiles with Vertical Magnetic Gradients

Gradient	$\delta\lvert\mathrm{B}\rvert_{RMS}$: 6302	5250	6768_{ASP}	6768_{MDI}
0 G/km	0.8 G	36 G	6.7 G	2.1 Mx/cm^2
1 G/km	1.6 G	64 G	9.3 G	3.3 Mx/cm^2
2 G/km	2.3 G	72 G	10.5 G	4.8 Mx/cm^2
3 G/km	2.7 G	85 G	11.1 G	6.9 Mx/cm^2
Socas-Navarro et al. (2000)	2.0 G	48 G	9.3 G	1.7 Mx/cm^2

variations of these quantities (exemplified here by density) are: $\rho_{\mathrm{pert}}(t) = \Re\{\rho\}\cos(\omega t) + \Im\{\rho\}\sin(\omega t)$. Vertical lines in Fig 3 show core formation heights for the 6302, 6768 and 5250 Å lines (z=168, 291, 549 km respectively) in a NLTE umbral atmosphere.

The MHD perturbation was applied to a Maltby M atmosphere with and without vertical magnetic gradients. In the case of no vertical gradient, a 2500 G field was supplied. For a realistic gradient, a NLTE inversion of sunspot observation (Socas-Navarro et al., 2000) was used, see Fig 4. Also, gradients of 1, 2 and 3 G/km were tested. The Stokes profiles output from the model were inverted using a ME fitting procedure for a completely magnetized atmosphere (no stray light). In this manner, the magnetic field strength was determined from simulated profiles for one MHD oscillation period for the 6302, 6768 and 5250 Å spectral lines for a constant field and a realistic gradient, see Fig 5.

The results show that thermodynamic fluctuations alone and resultant line profile changes cause varied B amplitudes to be derived from the inversion. Therefore, thermodynamic crosstalk is not limited to the magnetogram algorithms, but is also present in inversion methods. The RMS amplitudes for each spectral line pair and vertical gradient can be found in Table 2. Sampling of the vertical gradients is present as seen in the increasing amplitudes with increasing gradients in Table 2. Height of formation fluctuations due to the MHD thermodynamic perturbations were $\delta z_{6302} \approx 3.6$ km, $\delta z_{6768} \approx 6.0$ km and $\delta z_{5250} \approx 30$ km.

The phase differences observed for both thermodynamic crosstalk and vertical gradient sampling are (v, $\delta\lvert\mathrm{B}\rvert$)=90° for all the spectral lines analyzed with the Milne Eddington fitting routine similar to the ASP analysis. This is distinctly different from results (Rüedi et al., 1999) for 6768 Å line and the

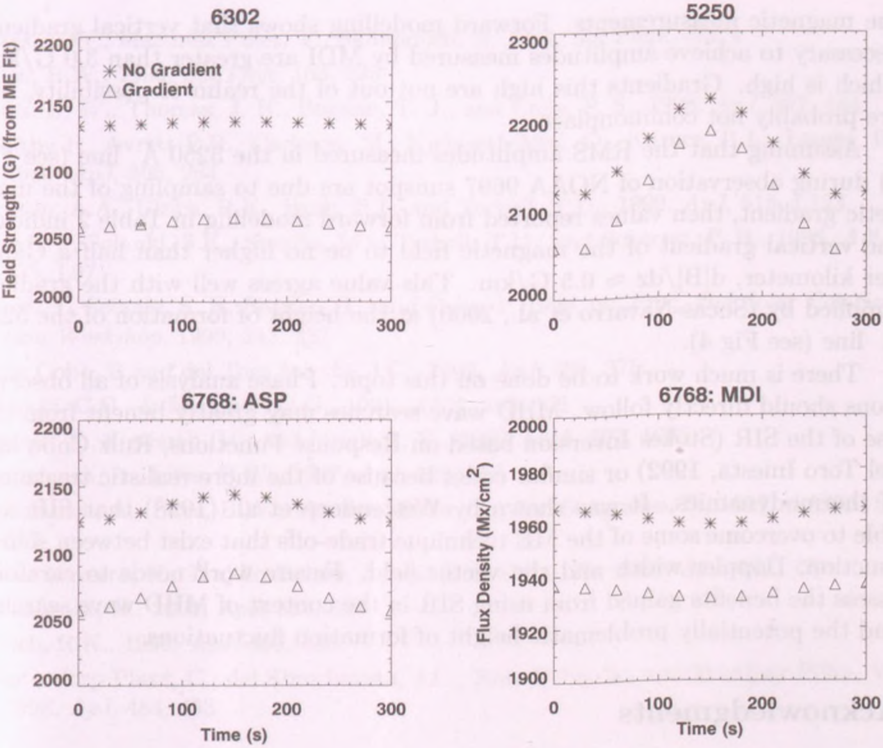

Figure 5: The field strengths derived from a ME fit to profiles computed as a Maltby M atmosphere experiences velocity and thermodynamic perturbations.

magnetogram method. The plot on the lower right in Fig 5 shows that provided with the same exact line profiles, the MDI analysis algorithm interprets changes in the line profile as a **decrease** in magnetic flux when the ASP fitting routine interprets the same line profile changes as an **increase** in field strength. Indeed, this is worrying.

5. Discussion

Results herein and those of Rüedi et al. (1999) could reconcile the $(v, \delta|\mathrm{B}|)$ phase differences measured with ASP (90°) and MDI (−90°), if thermodynamic line profile changes and vertical gradients are the cause of measured oscillations in the magnetic measurements. Forward modelling shows that vertical gradients necessary to achieve amplitudes measured by MDI are greater than 3.0 G/km, which is high. Gradients this high are not out of the realm of possibility, but are probably not commonplace.

Assuming that the RMS amplitudes measured in the 5250 Å line (see Fig 1) during observation of NOAA 9697 sunspot are due to sampling of the magnetic gradient, then values reported from forward modeling in Table 2 indicate the vertical gradient of the magnetic field to be no higher than half a Gauss per kilometer, $d|B|/dz \approx 0.5$ G/km. This value agrees well with the gradient supplied by (Socas-Navarro et al., 2000) at the height of formation of the 5250 Å line (see Fig 4).

There is much work to be done on this topic. Phase analysis of all observations should directly follow. MHD wave searches may greatly benefit from the use of the SIR (Stokes Inversion based on Response Functions, Ruiz Cobo and del Toro Iniesta, 1992) or similar codes because of the more realistic treatment of thermodynamics. It was shown by Westendorp et al. (1998) that SIR was able to overcome some of the ME technique trade-offs that exist between source function, Doppler width and the vector field. Future work needs to carefully assess the benefits gained from using SIR in the context of MHD wave searches and the potentially problematic height of formation fluctuations.

Acknowledgments

We thank: H. Socas-Navarro for the use of his ME inversion code and observed magnetic gradient, B. Lites for assistance in ASP data reduction, and P. Cally for supplying an MHD eigenfunction.

References

Balthasar, H., 1999, *Sol Phys*, 187, 389

Bellot Rubio, L.R., Collados, M., Ruiz Cobo, B., Rodriguez Hidalgo, I., 2000, *ApJ*, 534, 989

Bruls, J.H, Lites, B.W., and Murphy, G. A., in: *Proc. of 11th Sac Peak Workshop*, 1990, 444

Cally, P.S., Bogdan, T.J., and Zweibel, E.G., 1994, *ApJ*, 437, 505

Elmore, D.F., Lites, B.W., Tomczyk, S., et al, 1992, *SPIE* 1746, 22

Groth, E., 1975, *ApJS*, 29, 285

Horn, T., Staude, J. and Landgraf, V., 1997, *Solar Phys.* , 172, 69

Lites, B.W., Martínez Pillet, V., Skumanich, A. 1994, *Sol Phys*, 155, 1

Lites, B.W., 1996, *Sol Phys*, 163, 223

Lites, B. W., Thomas, J. H., Bogdan, T. J., and Cally, P. S., 1998, *ApJ*, 497, 464

Maltby P., Avrett E.H., Carlsson, M., Kjeldseth-Moe, O., Kurucz, R.L., Loeser, R., 1986, *ApJ*, 306, 284

Norton, A.A., Ulrich, R.K., Bush, R.I., and Tarbell, T.D., 1999, *ApJ*, 518, L123

Rüedi, I., Solanki, S.K., Stenflo, J.O., Tarbell, T.D., and Scherrer, P. H., 1998, *A&A*, 335, L97

Rüedi, I., Solanki, S. K, Bogdan, T., and Cally, P. 1999, in: *Proc. 2nd Solar Polarization Workshop*, 1999, 243, 337

Ruiz Cobo, B and del Toro Iniesta, J.C., 1992, *ApJ*, 398, 375

Rybicki, G.B., & Hummer, D.G., 1991, *A&A*, 245, 171

Settele, A., Sigwarth, M., and Muglach, K., 2002 *A&A*, 392, 1095

Skumanich, A., Lites, B.W., 1987, *ApJ*, 322, 473

Skumanich, A., Lites, B.W., Martínez Pillet, V., and Seagraves, P., 1997, *AJSS*, 110, 357

Socas-Navarro, H., Trujillo Bueno, J., and Ruiz Cobo, B., 2000, *ApJ*, 530, 977

Uitenbroek, H., 2001, *ApJ*, 557, 389

Ulrich, R.K., 1996, *ApJ*, 465, 436

Westendorp Plaza, C., del Toro Iniesta, J.C., Ruiz Cobo, B., and Martínez Pillet, V., 1998, *ApJ*, 484, 453

CHALLENGES IN CORONAL MORETON WAVES

I. Ballai[1] and R. Erdélyi[2]
SPARC, Dept. of Applied Mathematics, Univ. of Sheffield
Hounsfield Rd., Hicks Building, Sheffield, S3 7RH, England (UK)
E-mail: [1]`i.ballai@sheffield.ac.uk`, [2]`robertus@sheffield.ac.uk`

Abstract

Observations with the Extreme Ultraviolet Imaging Telescope (EIT) onboard SOHO have revealed the existence of transient coronal waves which propagate across the visible solar disc and are generated by an impulsive event. Using observational quantities (propagation speed, attenuation length) we derive average values for magnetic field intensity and viscosity in the low corona, i.e. we develop *global coronal seismology.*

KEYWORDS: *Sun, MHD, waves*

1. Introduction

The latest observational results provided by space telescopes showed us directly the existence of *global coronal waves*, able to propagate in the solar atmosphere for distances comparable with the solar radius. Usually these waves originate from an impulsive source, though the generation mechanism is still unknown. Because of their type of propagation, these waves are different from those observed recently in coronal loops, called local coronal waves.

One of the oldest global waves known in the solar atmosphere are the chromospheric Moreton waves (Moreton and Ramsey, 1960) seen in the wings of H_α propagating with a speed of 400-2000 km/s in an arc rarely exceeding 120° in the hot chromosphere at 10^4 K. Extrapolating the speed and locations of the arc indicates that the waves' origin intersects well with the impulsive phase of an associated H_α flare. The arc may not form or may not be observable until it is tens of Mm from the flaring region. Based on their propagation character, Moreton waves are considered fast shock waves. Another global wave phenomenon is the X-ray wave seen by YOKHOH in soft X-ray propagating in the corona with a speed of 600 ± 100km/s. They are interpreted as fast shock waves. Narukage et al. (2002) studied the Moreton and X-ray waves which appeared on 3 November 1997 and they concluded that the two type of waves are very well correlated in time and space, so (i) they must have the same origin and (ii) the X-ray waves are the coronal counterpart of the chromospheric Moreton waves.

Recent observations by the Extreme-ultraviolet Imaging Telescope (EIT) onboard SOHO have provided unambiguous evidence for large-scale coronal impulses initiated during the early stage of a flare and/or CME. Although it seems that all EIT waves are correlated with CMEs, there are some reports stating that in fact EIT waves would be correlated with flares, at least those EIT waves which are very bright. EIT waves are typically of lower amplitude than Moreton waves and they can extend 360° surrounding the initiating region.

EIT waves are seen in a bandpass dominated by the emission lines of Fe XII at 192.3, 193.5 and 195 A (the 195 A bandpass). The emission lines exhibit a peak emission near 1.6 MK at coronal densities. EIT waves propagate in the quite Sun with a speed of 200-400 km/s at almost constant altitude. Observations show that an EIT wave has two stages: first there is an early (driven) stage where the wave is associated with radio II type burst. In the initial stage the propagating wave could excite plasma radiation by accelerating electrons and creating an energized population that serves as the source of the radio emission. The second stage consists of a freely propagating wavefront.

The correlation between EIT and Moreton waves is still subject to a strong debate in the literature. For a very long time, EIT waves have been considered as the coronal counterpart of chromospheric Moreton waves. This was based on studies by Thompson et al. (2000) and Warmuth et al. (2002)) where the authors found a very good correlation between Moreton and EIT waves. In contrast, Shibata et al. (2001) and Eto et al. (2002) found that EIT and Moreton waves are not correlated, so the terminology of coronal Moreton waves attributed to EIT waves may seen to be inappropriate. This conclusion is further supported by the differences of their characteristic properties (different generating event, different propagation speed, different propagation character, etc.).

2. Application: Magnetic field and plasma diagnostic

Since EIT waves are able to cross very large distances, they can carry information about the plasma they pass through. The method of subtracting these information from waves is called *coronal seismology* (Aschwanden et al. 1999, 2002, Nakariakov et al., 1999, Nakariakov & Ofman, 2001, Ruderman and Roberts, 2002) and it became possible after the launch of high resolution space telescopes. Coronal seismology is a perfect tool to obtain physical parameters such as magnetic field and transport coefficients (volume and shear viscosity, resistivity, thermal conduction). Measuring the properties of MHD waves and oscillations (periods, wavelengths, amplitudes, attenuation lengths) combined with theoretical models (dispersion relations, evolutionary equations) we can determine coronal parameters.

Since EIT waves are observed to propagate in every direction almost isotropically, we suppose that they are fast magnetoacoustic waves (FMW) propagating perpendicular to the vertical equilibrium magnetic field. The temperature forming the 195 Å wavelength is $T = 1.6 \times 10^6$K corresponding to a sound speed c_S $(= (\gamma k_B T/\mu m_p)^{1/2})$ of 190 km/s ($\gamma = 5/3$, ratio of the specific heats; k_B, Boltzmann's constant; $\mu = 0.6$, the mean molecular weight; m_p, proton mass). Since the FMW propagate perpendicular to the field, their phase speed is given by $(c_S^2 + v_A^2)^{1/2}$, where v_A is the Alfvén speed. EIT waves are considered to be generated in the low corona at about $0.08R_\odot$ above the photosphere where the electron number density is 4.22×10^8 cm^{-3}. Then the magnetic field can be calculated by $B = v_A(4\pi m_p n)^{1/2}$, where n denotes the full particle number density, which is related to the electron number density by $n_e = 0.52n$ for $\mu = 0.6$. For the given speeds, we obtain the magnetic field is $0.8 - 4.5$ G. Before we step forward, we should remark that the lower limit of the propagation speed (200 km/s) is suspicious since for this value the plasma-beta is larger than unity, and the strength of the magnetic field obtained in such case is well below the acceptable values.

For an average value of EIT waves' speed of 300 km/s we find that the magnetic field is 3 G what we use in the forthcoming calculations. From $Br^2 = const.$, i.e. the magnetic flux is constant, we obtain that the magnetic field is 3.5 G in the photosphere and at 1 AU it is 7.5×10^{-5} G, respectively. These values are in very good agreement with the averages of the magnetic field found in the literature.

Another possibility to exploit EIT waves is to extract information about its wave behaviour and to use them to obtain averaged values for transport coefficients. This task is rather difficult due to the poor temporal resolution of the EIT camera. In the best case, the waves disappear after 3 or 4 images were taken. Unfortunately, this is far from being enough to carry out wavelet analysis. Likely, this problem will be overcome by TRACE and the forthcoming space satellites with a much better time resolution. We find, analyzing the front of an EIT wave, that it is very difficult to observe any wave characteristics. Instead it is likely that the EIT wavefront is an additional source of FMW at any time.

However, the information which can be still extracted from their propagation is related to their velocity attenuation. For illustration, we consider the event which occurred on 7 April 1997, at the start of solar cycle 23. The EIT wave has been generated by a flare situated in NOAA AR 8027, located slightly southeast of disk center. The peak emission occurred at 14:07 UT and images were taken at 14:12 UT; 14:21 UT; 14:35 UT; 14:53 UT after which the leading front of the wave disappeared. Figure 1 shows a series of running difference images taken at the above times. These images were obtained by rotating each image back to the time of the pre-event (at 13:28 UT). White regions show an increase in emission while dark regions indicate a decrease.

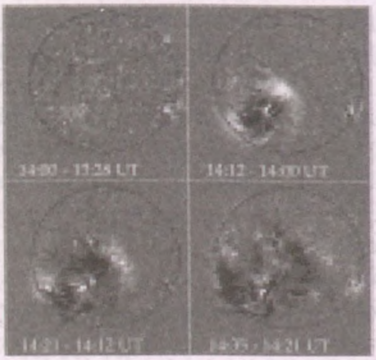

Figure 1: SOHO/EIT 195 $\mathring{A}$ running difference images showing the propagation of an EIT wave on 7 April 1997. The images were taken at 14:00 UT, 14:12 UT, 14:21 UT, 14:35 UT, with image at 13:28 subtracted from them (courtesy of B. Thompson)

Measuring the distance travelled by the leading front at the given times, we were able to obtain that the distance over which the speed of the wavefront decreased e-fold is roughly 365.3 Mm, i.e. $0.52 R_\odot$. This result, determined from the observations is going to be used in conjunction with theoretical modelling in order to determine plasma parameters.

We suppose the coronal plasma is isotropic, inhomogeneous and viscous. For the sake of simplicity we choose a constant background magnetic field parallel to the z-axis in Cartesian geometry. Although a spherical geometry and a viscosity described by the Braginskii tensor (usually in coronal plasmas the viscosity due to ions is given by this tensor) would be a better approximation, we suppose a simplified case in order to get a first insight into the problem of EIT wave attenuation. The equilibrium density and pressure decrease with height according to an $exp[-z/H]$ law where H is the pressure scale height ($H = 79$ Mm) in an isothermal plasma.

For a horizontal propagation perpendicular to the ambient magnetic field, the evolution of the velocity is given by an equation of the form $\sum_{n=1}^{4} a_n(\eta) d^n v/d\eta^n$

0, where $\eta = \omega^2 H^2 / v_A^2 exp[z/H]$. Considering weak dissipation (just like in coronal plasmas), the solution of this ODE with non-constant coefficients can be found in form of Fröbenius series, provided $\eta < 1$, resulting in

$$v \sim e^{-z/l_a} cos(Az), \tag{1}$$

where l_a is the attenuation length and A is a constant given by the equilibrium quantities. In Eq. (1) l_a is given by

$$l_a = \frac{2H}{\frac{2\nu^2}{H^2 c_S^2} + 1 - \sqrt{1 - \frac{4\omega^2 H^2}{c_S^2} + 4k^2 H^2}}. \tag{2}$$

The frequency of the waves constitute a serious uncertainty because the poor temporal resolution of the EIT camera does not allow us to perform a more precise analysis to obtain this quantity. However, we suppose that EIT waves have a frequency of 1 mHz. Using the attenuation length obtained earlier, we found that the coefficient of kinematic viscosity derived, based on the attenuation of an EIT wave with a frequency of 1 mHz, is $2.67 \times 10^{12}\ m^2/s$, two order of magnitude larger than the value obtained using the Spitzer's formula (Spitzer, 1962).

3. Conclusions

The present study is a first attempt to exploit the remarkable properties of coronal global waves to carry information about the mean values of the magnetic field strength and transport coefficients. The extraction of information from the observed wave propagation combined with the prediction of theoretical models allow us to develop global coronal seismology.

For the studied event, occurred on 7 April 1997, we obtained an average value of the magnetic field strength and the coefficient of kinematic viscosity. While the value of the magnetic field strength is in very good agreement with other previous studies, the value of the coefficient of viscosity is larger than the value obtained from Spitzer's classical formula.

Obviously, the calculations in the present paper are just a first approximation where we used the simplest model possible. For a better understanding of the phenomena of global coronal waves one should include other important effects, such as the effect of curvature, the anisotropic character of the coronal plasma, the effect of geometrical dispersion, etc. The results obtained by the EIT camera should be combined with observations by TRACE which has a better temporal resolution. Of course, the field of view of TRACE is limited compared to EIT. These new effects will be addressed in our forthcoming investigations.

Acknowledgments

The authors acknowledge the financial support by PPARC (UK) and the NFS Hungary (OTKA, TO43741). R. E acknowledges M. Kéray for patient encouragement. R. E also acknowledges the support received from the Nuffield Foundation (NUF-NAL 99).

References

Aschwanden et al. 2002, Sol. Phys., 206, 99

Aschwanden et al. 1999, *Astrophys. J.* , 520, 880

Eto, S. et al. 2002, *PASJ*, 54, 481

Moreton, G.F. & Ramsey, H.E. 1960, *PASP*, 72,357

Nakariakov, V. M. et al. 1999, Science, 285, 862

Nakariakov, V.M. & Ofman, L. 2001, *A&A*, 372, L53

Narukage, N. et al. 2002, *Astrophys. J.* , 572, L109

Ruderman, M.S. & Roberts, B. 2002, *Astrophys. J.* , 577, 475

Shibata, K. et al. 2001, in Martens, P.C.H and Cauffman, D. (eds.) Cospar Series, p. 103

Spitzer, L. 1962, Physics of Fully Ionized Gases, Interscience, New York

Thompson, B. et al. 2000, *Solar Phys.* , 193, 161

Warmuth, A. et al. 2002, in H. Sawaya-Lacoste (ed.), ESA SP-477, p. 198

THERMAL CONDUCTION DAMPING OF LONGITUDINAL WAVES IN CORONAL LOOPS

I. De Moortel[1] and A.W. Hood
School of Mathematics and Statistics, University of St Andrews
North Haugh, St Andrews, KY16 9SS, Scotland
E-mail: [1]`ineke@mcs.st-and.ac.uk`

Abstract

High cadence TRACE observations show that outward propagating intensity disturbances are a common feature in large coronal loops. An overview is given of measured parameters of such longitudinal waves in coronal loops. We found that loops that are situated above sunspot regions display intensity oscillations with periods centred around 3 minutes, whereas oscillations in 'non-sunspot' loops show periods centred around 5 minutes. The observed longitudinal waves are interpreted as propagating slow magneto-acoustic waves and we show that the disturbances are not flare-driven but are most likely caused by an underlying driver exciting the loop footpoints. We found that (slightly enhanced) thermal conduction could account for the observed damping lengths.

KEYWORDS: *Sun, corona, oscillations*

1. Introduction

An important class of proposed mechanisms to explain the high temperatures in the solar corona are the wave heating mechanisms, which rely on the dissipation of wave energy to provide the required heating. Although the existence of MHD waves in the corona has been widely accepted on theoretical grounds for several decades (Roberts 2000), observational evidence remained inconclusive. However, satellites such as TRACE and SOHO have recently provided a multitude of observations of both transversal and longitudinal oscillations. For example, periodic density and intensity variations were detected in polar plumes (Ofman et al.,1997; DeForest & Gurman, 1998) by both UVCS and EIT onboard SOHO and interpreted by Ofman et al. (1999) as slow magneto-acoustic waves. Similar propagating intensity variations were detected in large coronal loops in the 171 Å and 195 Å passbands of both EIT/SOHO and TRACE (Berghmans & Clette, 1999; De Moortel et al., 2000; Robbrecht et al.,2001). An extensive overview and analysis of a large number of transversal, flare-excited, coronal loop oscillations was presented by Schrijver et al. (2002) and a detailed discussion of the measured parameters can be found in Aschwanden et al. (2002).

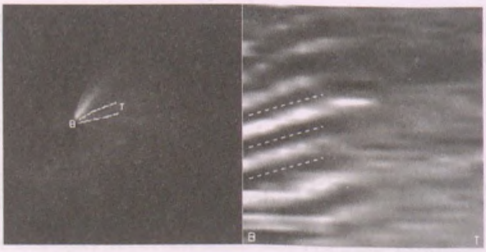

Figure 1: *Left:* Typical example (TRACE 171 Å - 13 June 2001, 0646 UT) of a large coronal loop footpoint supporting an oscillatory signal. *Right:* A plot of the running difference between the average time series.

In this paper we give a short overview of some of the observed properties of longitudinal waves, observed by TRACE. The observations and data analysis are described in Section 2. An explanation of the analysis and an overview of the results is given in Section 3, followed by a discussion on the damping by thermal conduction and conclusions in Section 4.

2. Observations and Analysis

The analysed observations are high-cadence EUV TRACE data (171 Å), taken as part of JOP 83 (23 March 1999 and 04-19 April 2000) and JOP 144 (05-13 June 2001). All data were corrected for dark current and cosmic ray hits using the standard TRACE procedures. For a detailed analysis, we extracted subcubes of roughly 25-30 minutes, with a constant cadence.

For the data analysis, we use a running difference to identify propagating disturbances and a wavelet analysis (99.0 % confidence level) to determine an oscillation timescale (De Moortel et al. 2000). An example of a large coronal loop supporting a longitudinally propagating intensity perturbation is shown in Fig. 1 (left). The straight, diagonal ridges of higher (bright) and lower (dark) intensity in the running difference image (Fig. 1, right) indicate that a disturbance is travelling along the coronal structure with a more or less constant speed.

3. Results

The statistical information of the averages and ranges of some of the different measured parameters can be found in Table 1. The propagation speeds (122±43 km/s) were calculated from the slopes in the running differences, and in most

Table 1: Statistical overview of the averages and ranges of physical properties of the 38 oscillations found in the footpoints of large coronal loops.

Parameter	Average	Range
Oscillation period P	282 ± 93 s	$145 - 525$ s
Propagation speed v	122 ± 43 km/s	$70 - 235$ km/s
Relative Amplitude A	4.1 ± 1.5 %	$0.7 - 14.6$ %
Damping length L_d	8.9 ± 4.4 Mm	$2.9 - 23.2$ Mm
Energy flux F	342 ± 126 ergs/cm^{2}s	$194 - 705$ ergs/cm^{2}s

cases, no significant deceleration or acceleration was observed. It is also worth remarking that we only found positive gradients, i.e. we only found outward propagating disturbances. The average amplitudes of the intensity oscillations, as percentages of the background brightness, are very small, of the order of 4.1 ± 1.5 %. From a wavelet analysis, we obtained the oscillation periods but, as we are concentrating on propagating signals, we only take into account those periods P_{prop} that are roughly consistent and above the confidence level in a number of consecutive positions along the loops. We found values for these dominant oscillatory periods of the order of $P = 282 \pm 93$ seconds, and as all of these are well above the acoustic cutoff value, the waves are propagating into the corona. However, De Moortel et al. (2002a) pointed out that loops that are situated above sunspot regions display intensity oscillations with a period of the order of $P_S = 172 \pm 32$ seconds, whereas oscillations in 'non-sunspot' loops show periods of the order of $P_{NS} = 321 \pm 74$ seconds. From the number of consecutive positions where a similar period is detected, we can estimate a 'detection length', $L_d = 2.9 - 23.2$ Mm. This is not a true damping length but only indicates where the intensity changes vanish into the data noise and can thus be thought of as a lower limit to the true physical damping length.

4. Discussion and Conclusions

Taking into account all the observed and measured properties, the small-amplitude, propagating intensity disturbances were interpreted as *slow magneto-acoustic waves.* The compressive disturbances have no noticeable effects on the loops, as the overall, large-scale structure and appearance of the coronal loops remained stable and unchanged throughout the observational sequences. At the time

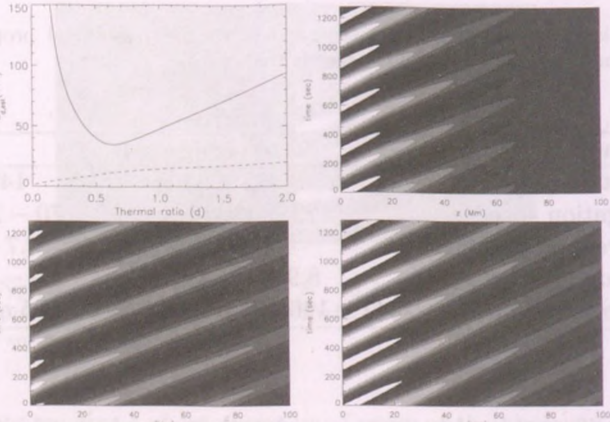

Figure 2: *Top-left:* Plot of the estimated damping length $L_{d,est}$ in Mm as a function of the thermal ratio d. *Top-right:* Contour plot of perturbed density from a numerical simulation with $d \approx 4\times0.16$. *Bottom-left:* Contour plot of perturbed density from a numerical simulation with $d \approx 0.16$. *Bottom-right:* As on the left but with $d \approx 10 \times 0.16$.

of observing, no major flares occurred in any of the considered active regions, making it highly unlikely that the observed longitudinal waves are flare-driven. However, the clear difference in periods found in loops situated above sunspots (~ 3 min) and loops above non-sunspot regions (~ 5 min) strongly points toward an underlying driver exciting the loop footpoints. This results suggests that both the 3-minute sunspot oscillations and the global 5-minute solar oscillations directly or indirectly drive oscillations in coronal loops.

To examine the effect of thermal conduction on the observed waves, we look for plane wave solutions and assume a constant background magnetic field, pressure p_0 and density ρ_0. The linearised MHD equations then combine into the dispersion relation

$$\kappa_{\|0}(\gamma-1)p_0T_0k^4 - [\kappa_{\|0}(\gamma-1)\omega^2\rho_0T_0 - i\gamma p_0^2\omega]k^2 - i\omega^3\rho_0p_0 = 0\,, \tag{1}$$

where $\kappa_{\|0}$ is the parallel thermal conductivity, ω the frequency and k the wavenumber in the z-direction. Given the frequency, ω, this is a 4th order equation, giving 4 solutions, k_i, for the wavenumber. In the absence of thermal conduction, we would obtain a quadratic equation for k, corresponding to sound waves, and the extra mode generated when $\kappa_{\|0} \neq 0$ is a thermal mode. The full solution for the perturbed velocity is then given by,

$$v = Ae^{-ik_1 z} + Be^{-ik_2 z} + Ce^{-ik_3 z} + De^{-ik_4 z}\,, \tag{2}$$

where the constants A, B, C and D are determined from the boundary conditions. As we study the damping of oscillations, we are only interested in the positive solutions for k, which decay for increasing z. These solutions will be complex, with the imaginary part corresponding to the decay. Assuming standard coronal values for all variables, we find estimates for the damping length of the order of 4.3 Mm and 137 Mm (De Moortel et al., 2002c).

To examine the importance of parallel thermal conductivity, the estimated damping length $L_{d,est}$ is plotted (Fig. 2, top-left) against a dimensionless thermal ratio

$$d = \frac{(\gamma - 1)\kappa_{\|0} T_0 \rho_0 \omega}{\gamma^2 p_0^2}\,.$$

For standard coronal values, $d \approx 0.16$. However, for $d \approx 4 \times 0.16$ the damping length reaches a minimum of 35 Mm, implying that the observed detection lengths could be explained by considering enhanced thermal conductivity, $\kappa_{\|0} = 4 \times 10^{-11} T_0^{5/2}$ W m^{-1} deg^{-1}. The contour plot (Fig. 2, top-right) of the perturbed density confirms that, for $d \approx 4 \times 0.16$, the perturbations drop off by more than a factor of four in about 40 Mm, after which the perturbations would be lost in the data noise. On the bottom row of Fig. 2 similar plots of the perturbed density are shown for $d \approx 0.16$ and $d \approx 10 \times 0.16$ respectively. When comparing these contour plots with the plot for $d \approx 4 \times 0.16$, it becomes clear that arbitrarily increasing the thermal conduction does *not* necessarily decrease the damping length. For large thermal conduction, the plasma becomes isothermal and the remaining mode is an isothermal sound wave, travelling at the (slower) isothermal sound speed. This slower propagating speed is reflected in the steeper gradients in the contour plot for $d \approx 10 \times 0.16$. This implies that, to obtain damping lengths below the value of 35 Mm, an additional damping mechanism would have to be included in the model. One possibility would be to include (parallel) viscosity. A comparison between the effect of viscosity and thermal conduction is made by Hood & De Moortel (2003). Additionally, the effects of inhomogeneities might become important, as the estimated wavelengths are of the order of the gravitational scale height for some of the observed oscillations. For a more comprehensive and detailed description of the analysis and results presented in these short proceedings, we refer the reader to De Moortel et al. (2002b, 2002c).

References

Aschwanden, M.J., De Pontieu, B., Schrijver, C.J., Title, A. 2002, *Sol. Phys.* **206**, 99

Berghmans, D., Clette, F., 1999, *Sol. Phys.* **186**, 207

De Moortel, I., Ireland, J., Walsh, R.W. 2000, *A & A* **355**, L23

De Moortel, I., Ireland, J., Hood, A.W.,Walsh, R.W. 2002a, *A & A* **387**, L13

De Moortel, I., Ireland, J., Hood, A.W.,Walsh, R.W. 2002b, *Sol. Phys.* **209**, 61

De Moortel, I., Hood, A.W., Ireland, J.,Walsh, R.W. 2002c, *Sol. Phys.* **209**, 89

DeForest, C.E., Gurman, J.B. 1998, *ApJ* **501**, L217

Hood, A.W., De Moortel, I. 2003, *in preparation*

Ofman, L., Romoli, M., Poletto, G., Noci, C., Kohl, J.L. 1997, *ApJ* **491**, L111

Ofman, L., Nakariakov, V.M., DeForest, C.E.: 1999, *ApJ* **514**, 441

Robbrecht, E., Verwichte, E., Berghmans, D., Hochedez, J.F., Poedts, S., Nakariakov, V.M. 2001, *A & A* **370**, 591

Roberts, B. 2000, *Sol. Phys.* **193**, 139

Schrijver, C.J., Aschwanden, M.J., Title, A. 2002, *Sol. Phys.* **206**, 69

SPICULE FORMATION BY ION-NEUTRAL DAMPING

S. P. James[1] and R. Erdélyi[2]
Space and Atmosphere Research Center, University of Sheffield
Hicks Building, Hounsfield Rd., Sheffield S3 7RH, United Kingdom
E-mail: [1]`s.p.james@shef.ac.uk`, [2]`robertus@sheffield.ac.uk`

Abstract

The possible generation of spicules by Alfvénic waves is studied in MHD where dissipation is mainly caused by ion-neutral collision damping, as suggested by Haerendel (1992). The propagation of high frequency Alfvén waves on vertically open solar magnetic flux tubes is considered by numerically solving a set of fully nonlinear, dissipative 1.5D MHD equations with the waves being generated by a continuous sinusoidal driver in the low atmosphere of the Sun. Spicule-like structures with heights of around 4 000 – 10 000 km were formed, primarily by the impact of a series of slow shocks generated by the continuous interaction between the upward propagating driven and reflected wave trains rather than the predicted ion-neutral damping mechanism.

KEYWORDS: *Sun, MHD, plasma physics*

1. Introduction

In the photosphere and chromosphere the solar plasma is only partially ionised. Changes in the magnetic and electric fields directly impact the ion fluid but the neutral fluid is indirectly affected, being collisionally coupled to the ions. At sufficiently high frequencies the friction between the ion and neutral fluids can become important and Alfvén wave damping and dissipation can occur. Haerendel (1992) showed that this effect produces a net waveperiod averaged force in the direction of wave propagation which, for realistic parameters of the solar atmosphere, can support a spicular structure against gravity. De Pontieu (1999) numerically investigated this effect using an essentially 1D hydrodynamic model by looking at the evolution along a cylinder of flux lines and included the heating and coupling into vertical momentum due to wave damping by applying the WKB approximation to plane polarised small amplitude Alfvén waves. It was found that structures resembling solar spicules could indeed be generated and supported by this mechanism under these approximations. However, the assumption of both linearity and the WKB approximation were violated. This work extends the model to 1.5D fully dissipative, nonlinear MHD simulations. 1.5D MHD equations, adiabatic apart from heating due to ion-neutral damping, are solved numerically using a flux corrected transport technique. The equations are adiabatic with the exception of heating due to ion-neutral damping. Further details can be found in James & Erdélyi (2002).

2. Results

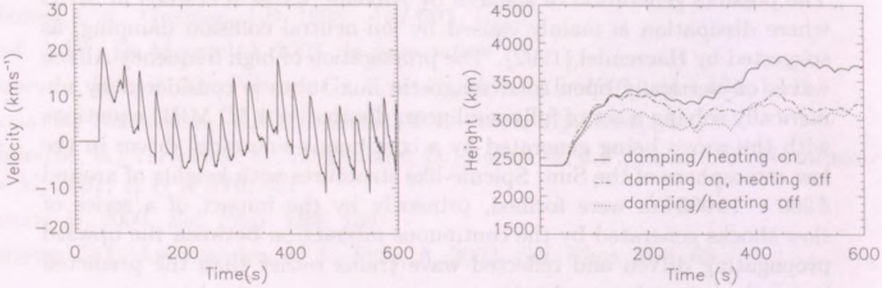

The figure above left shows the velocity profile of the transition region, identified with the top of the spicule for 4s waveperiod, amplitude 20% of the background Alfvén speed and 20 G coronal magnetic field. The wavefront reaches the transition region at about 50 s and starts to push it upwards. The plasma is then decelerated by gravity. Somewhat more than half of the Alfvén wave flux is reflected off the transition region resulting in a downward propagating train of reflected waves. This reflected wave train interacts with the upward propagating waves resulting in a series of shocks which propagate upward at the slow speed. The figure above right shows the motion of the transition region for three runs with identical parameters. The inclusion of damping alone makes little difference whilst the inclusion of heating increases the height of the structure. Evolution of the structure is *dominated by the shocks rather than the force from ion-neutral damping predicted by the linear WKB theory.* However, the heating from damping has a definite effect, increasing the thermal pressure gradient and helping to support the plasma against gravity, resulting in greater heights. At longer wave periods, the three results converge as the damping and resultant heating become negligible. At shorter wave periods, the waves become too strongly damped in the upper chromosphere and the reduction in wave amplitude reaching the transition region overcomes the positive benefit from increased heating resulting in smaller structures.

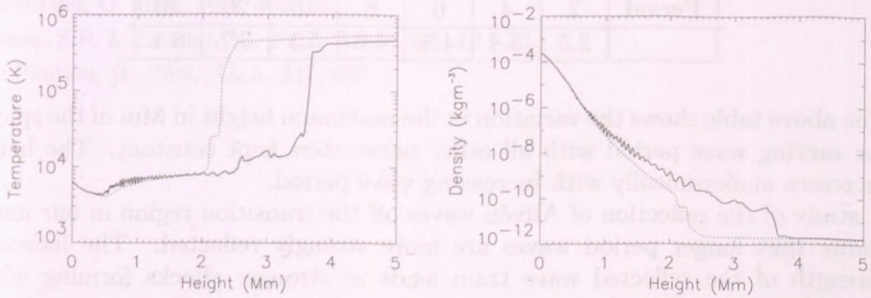

The figures above show the temperature and density profiles at the end of one characteristic simulation with the initial profiles shown for reference. The density profile shows the stratification into high and low density regions caused by the interaction of the upward propagating and reflected wave trains. The profiles are similar in character for all parameters considered. The peaks and troughs in the density profile become considerably more pronounced with increasing wave period, reaching more than a factor of 10 apart for 40 s wave periods. Such fine structure may not be visible in observations so that the results are not necessarily in contradiction with the fairly flat profiles observed.

Magnetic field	10	20	40
4s Period	3.4	3.8	5.1
40s Period	5.4	6.1	5.6

The damping strength is proportional to the magnetic field which reduces the amplitude of waves reaching the transition region and tends to reduce height. In contrast, temperatures and therefore the supporting thermal pressure are higher for the same reason. Characteristic velocities (in the absence of damping) are also higher due to the increased Alfvén speed. Once again though, it is reflections that dominate the picture. Increasing the coronal field leads to two competing effects regarding reflection strength. Firstly, the increased wavelength relative to the fixed transition region width makes reflections more efficient. On the other hand, steepened waveforms are more strongly reflected. Increasing the wavelength results in less steepening over the same distance which reduces reflection efficiency. This explains why the 4s period results show a monotonic increase as the 10G and 20G cases lead to only weak reflection whilst the results for 40s period show no clear trend.

Period	2	4	6	8	10	20	40
	3.5	3.8	4.5	4.6	5.1	5.7	6.1

The above table shows the variation in the maximum height in Mm of the spicule for varying wave period with all other parameters kept constant. The height increases monotonically with increasing wave period.

A study of the reflection of Alfvén waves off the transition region in our model shows that longer period waves are more strongly reflected. The increased strength of the reflected wave train leads to stronger shocks forming which would help to explain the increased velocities and heights. Countering this, the heating effect will decrease with increasing time period, reducing the ability of the thermal pressure gradient force to support the structure against gravity.

3. Conclusion

Evolution of the structure was found to be dominated by the slow shocks formed by the continuous interaction between the upward propagating wave train and the waves reflected off the moving transition region. The structures formed had density and temperature profiles broadly in agreement with observations. Heights and velocities could also be recreated but were more parameter sensitive. Alfvén wave damping helped to heat the structure but the coupling into vertical momentum predicted by the WKB linear analysis was only a minor effect in the subsequent evolution. Since the effect depends on the level of ionisation, inclusion of thermal conduction and radiative losses may be beneficial. As well as the WKB approximation initially being violated in the transition region, it is also violated everywhere once the interaction of upward propagating and reflected waves results in stratification into high and low density regions. It is perhaps not surprising then that the anticipated effects failed to materialise. This stratification is primarily the result of a partially standing wave. A more random source of Alfvénic disturbances should reduce this effect.

Acknowledgments

This work was supported by UK PPARC. RE acknowledges M. Kéray for patient encouragement and the financial support obtained from the NSF, Hungary (OTKA).

References

Haerendel, G. 1992, Nat, 360, 241

James, S.P. & Erdélyi, R., 2002, A&A, 393, L11-L14

De Pontieu, B. 1999, A&A, 347, 696

QUASI-PERIODIC BEHAVIOUR OF A FLARE RIBBON SYSTEM

A. Ludmány[1]**, B. Major**[2] **and V. M. Nakariakov**[3]
[1]Heliophysical Observatory H-4010 Debrecen, P.O.B. 30. Hungary
[2]Eötvös University, Dept. of Astronomy H-1518 Budapest, P.O.B. 32., Hungary
[3]Physics Department, University of Warwick Coventry, CV4 7AL, UK
E-mail: [1]`ludmany@tigris.klte.hu`, [2]`major@konkoly.hu`,
[3]`valery@astro.warwick.ac.uk`

Abstract

A series of quasi-periodic pulsations have been detected in the flare of 19th July 1999. The total area occupied by the flare ribbons exhibited temporary increases in the declining phase of the flare at certain moments, the period of the pulses was about 20-30 minutes. The phenomenon has been recognized in the center, as well as at 0.5 and 1.0 Å wings on both sides of the H-alpha line.

KEYWORDS: *flare, oscillations*

1. Introduction

Oscillatory and wave phenomena in the solar corona attract continuously growing attention of observers and theorists in the context of MHD coronal seismology and coronal heating. Often, the oscillations are associated with flaring loops. Svestka (1994) described repetitive X-ray brightenings with mean periods close to 20 min. A typical example was studied by Harrison (1987): the Hard X-ray Imaging Spectrometer on SMM detected soft X-ray (3.5 to 5.5) keV pulsations with the period of 24 min. Very recently, 10-20 min periodicities have been found in the Doppler shift of the EUV emission lines observed by SOHO/SUMER (Kliem et al. 2002) and interpreted as slow magnetoacoustic modes by Ofman and Wang (2002). To our knowledge, there have not been reports of long-time periodicities associated with coronal events observed in the white light and in this contribution they are discussed for the first time.

2. Observational material and procedure

The event of July 19, 1999 was a classic impulsive flare with classification 2N/M5.8, it had two well developed, complex and receding systems of ribbons (Kulinová and Karlický, 2001). The observations have been gathered in the

Heliophysical Observatory, Debrecen, with the large coronograph and the attached tunable Lyot-filter. The FWHM of the filter is 0.4 Å. During flares the observer makes serii of observations at four wavelengths: line centre, +0.5 Å, -0.5 Å, and at a special passband ± 1 Å. A total of 19 such serii (76 frames) have been gathered between 07:46:53 and 11:03:08 UT, the first series recorded the state immediately before event. Figure 1 shows the first series about the flare. The observations were recorded on KODAK H-alpha patrol film and the involved frames were digitized later. With this strategy one can easily follow the intensity of the flare, because the H-alpha faculae are visible only up to about ±0.5 Å.

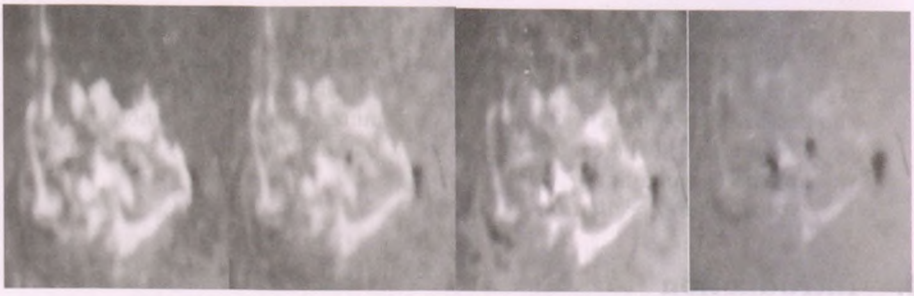

Figure 1: Images of the flare at the Hα line center, +0.5Å, -0.5Å, and ± 1 Å.

The aim of observing this series was to determine the time profile of the total flare ribbon area. Since the images were made by automatic exposures and an absolute photometric calibration was not possible, an indirect method was applied. This method was based on the analysis of the intensity histogram of each frame. The histograms of the intensities contain the three main components of the chromospheric pattern: the flare, facular and background points. Each component has a normal intensity distribution, so the total distribution is a superposition of three gaussians. The area of the gaussian representing the flare intensities is considered as a measure of the flare ribbon size. Figure 2.a. shows the histogram of a frame and the three fitted gaussians, the curve belonging to the flare points can readily be recognized.

3. Observational results

The time profiles at the four wavelengths are depicted together in Figure 2.b. The continuous line with crosses indicates the area at line center, dotted line

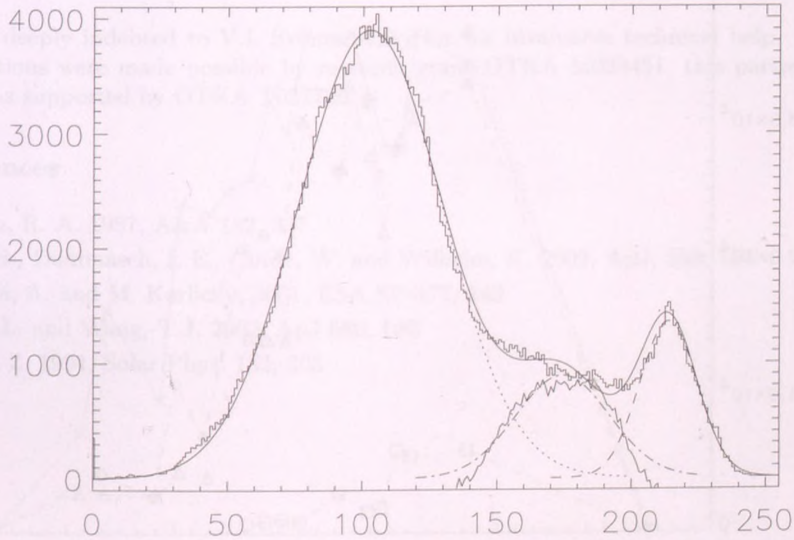

Figure 2: (a) Intensity histogram of a frame at the line center, horizontal axis: intensity level given by the 8-bit camera, vertical axis: number of pixels.

with triangles: +0.5 Å , dashed line with diamonds: -0.5 Å dot-dashed line with squares: ±1 Å. All of these distributions exhibit certain fluctuations which cannot be regarded as random. The curves have local minima and maxima close to each other which cannot happen incidentally because the measurements and the selection criteria are made differently and independently at the different wavelengths. The curves should be regarded as independent, so their local maxima and minima corroborate each other.

The most important piece of information to be deduced from the curves is the duration of the peaks. After the first maximum and decrease a temporary recovery follows at about 9:10 UT, then another decrease and increase at 9:40 and two later recoveries (in ±1 Å frames already not visible) at about 10:00 and 10:20 UT. The areas are depicted in the number of pixels, the area of a pixel is 0, 13 $arcsec^2$ (0.3549 *as* x 0.3643 *as*), no foreshortening has been taken into account because we are here only interested in the temporal behaviour and not

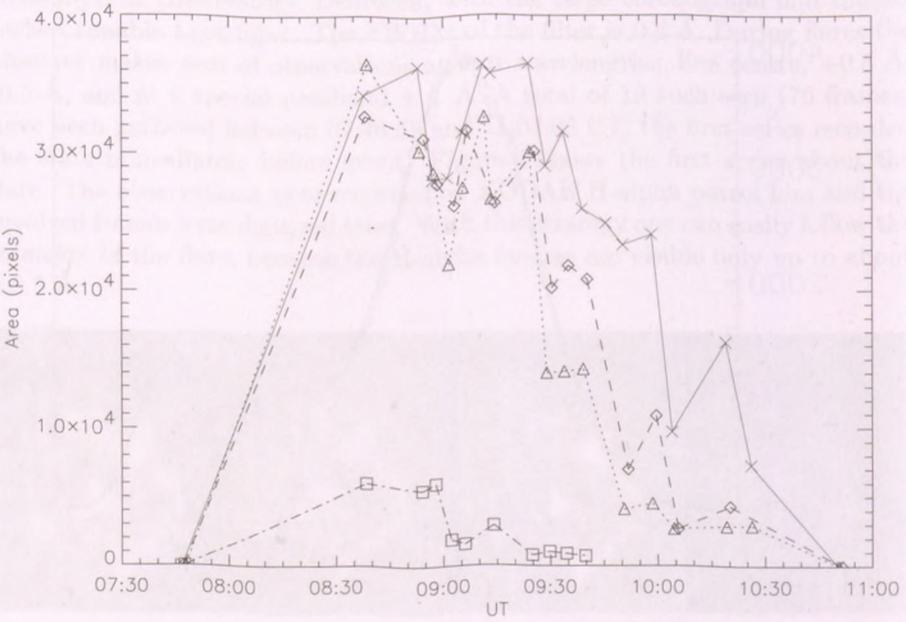

Figure 2: (b) Time profiles of the flare at the four wavelengths studied.

in the absolute size of the flare. One can see that the period of consecutive local maxima is between 20 and 30 minutes.

4. Discussion

The observed quasi-periodic variations of the white light emission intensity generated by a solar flare may be associated with slow magnetoacoustic oscillations of the flaring arcade, similar to that reported by Kliem et al. (2002). In this scenario, the slow waves are trapped between the loop footpoints and cause longitudinal field-aligned changes in the plasma density. The density fluctuations modulate the emission intensity observed. More detailed study of this scenario will be presented elsewhere.

Acknowledgments

We are deeply indebted to V.I. Skomorovsky for his invaluable technical help. The observations were made possible by research grant OTKA M028451, this particular work was supported by OTKA T037725.

References

Harrison, R. A. 1987, A&A 182, 337
Kliem, B., Dammasch, I. E., Curdt, W. and Wilhelm, K. 2002, ApJ, 568, L61
Kulinová, A. and M. Karlický, 2001, ESA SP-477, 143
Ofman, L. and Wang, T.J. 2002, ApJ 580, L85
Svestka, Z. 1994, Solar Phys. 152, 505

TRANSFORMATION OF THE ALFVÉN WAVES IN THE LOW BETA PLASMA

V. Fedun,[1] **A. Yukhimuk**[2] **and A. Voitsekhovskaja**[2]
[1]Taras Shevchenko National University
03022 Kyiv, Ukraine
[2]Main Astronomical Observatory NAS of Ukraine
03680 Kyiv, Ukraine
E-mail: [1]`fedun@mao.kiev.ua`, [2]`yukhimuk@mao.kiev.ua`

Abstract

The nonlinear mechanism of the transformation of magnetohydrodynamic (MHD) Alfvén waves to kinetic Alfvén waves (KAW) in the homogeneous magnetized plasma with small plasma parameter $\beta << 1$ is investigated. As the generation mechanism, the parametric instability, where the MHD Alfvén wave is the pumping wave is considered. On the basis of the two-fluid MHD and Vlasov equation the nonlinear dispersion relation describing three-wave interaction, the instability growth rate and the threshold of the instability are found. The theoretical results are used for the interpretation of plasma heating in the solar corona.

KEYWORDS: *Sun, MHD, Alfvén wave, instability*

1. Introduction

MHD Alfvén waves are weakly damping and there is a problem for transformation energy from waves to plasma particles. For the first time kinetic effects (account of the finite values of the proton Larmor radius) in Alfvén waves were taken into account in papers Coroniti (1970) and Stefant (1970). However only after the publication by Hasegawa (1976), kinetic Alfvén waves have received enough attention. KAWs retain main properties of MHD Alfvén waves, but they have some new important properties as well, including (1) dependence of the wave dispersion on the transverse wave vector component, and (2) presence of a non-zero longitudinal component of the electric field E_z.

In the present paper we focus on the new aspects of the transformation of MHD Alfvén waves into kinetic Alfvén waves. It is assumed that an MHD Alfvén wave with finite amplitude and dispersion relations $\omega_0^2 = k_{0z}^2 V_A^2$, propagates in the homogeneous magnetized plasma $\left(\vec{B}_0 = B_0 \vec{e}_z\right)$ with a small plasma parameter $\beta = \frac{8\pi n T}{B_0^2} << 1$ and decays into two KAW with wave vectors $\vec{k}_1$ and

$\vec{k}_2$ and frequencies ω_1 and ω_2, Were $V_A = \sqrt{\frac{B_0^2}{4\pi n_0 m_i}}$- is the Alfvén velocity, T=$(T_e + T_i)$ is the plasma temperature and m_i is the ion mass. The conservation laws for the three wave interactions are assumed to be satisfied:

$$\omega_0 = \omega_1 + \omega_2, \quad \vec{k}_0 = \vec{k}_1 + \vec{k}_2.$$

Also we assume that all wave vectors are situated in the XOZ plane.

2. The nonlinear dispersion equation for three-wave interaction

As an initial set of equations, for studying three-wave nonlinear interaction, we use the two-fluid MHD:

$$\frac{\partial \vec{V}_\alpha}{\partial t} = \frac{1}{m_\alpha}\left(e_\alpha \vec{E} + \vec{F}_\alpha\right) + \left(\vec{V}_\alpha \times \vec{\omega}_{B\alpha}\right) - \frac{T_\alpha}{m_\alpha n_\alpha}\vec{\nabla} n_\alpha,$$

$$\frac{\partial n_\alpha}{\partial t} + \vec{\nabla}\left(n_\alpha \vec{V}_\alpha\right) = 0,$$

$$\vec{\nabla} \times \vec{B} = \frac{4\pi}{c}\vec{j} + \frac{1}{c}\frac{\partial \vec{E}}{\partial t}$$

$$\vec{\nabla} \times \vec{E} = -\frac{1}{c}\frac{\partial \vec{B}}{\partial t},$$

$$\vec{\nabla} \cdot \vec{E} = 4\pi\rho.$$

Here $\vec{j} = e\left(n_i \vec{V_i} - n_e \vec{V_e}\right)$, $\rho = e\left(n_i - n_e\right)$,

$$\vec{F_\alpha} = \frac{e_\alpha}{c}\left(\vec{V}_\alpha \times \vec{B}\right) - m_\alpha\left(\vec{V}_\alpha \vec{\nabla}\right)\vec{V}_\alpha.$$

The index $\alpha = i, e$ correspond to ion and electron components of plasma respectively. As $F_e = \frac{m_e}{m_i}F_i$, influence of F_i force is small, and can be neglected. In the Ampere low we neglect the displacement current for low-frequency waves. The electron density and velocity, electric and magnetic fields are written in the forms:

$$n_e = n_0 + \tilde{n}_0 + n_1 + n_2,$$

$$\vec{V} = \vec{V}_0 + \vec{V}_1 + \vec{V}_2,$$

$$\vec{E} = \vec{E}_0 + \vec{E}_1 + \vec{E}_2,$$

$$\overrightarrow{B} = \overrightarrow{B}_0 + \overrightarrow{b}_0 + \overrightarrow{b}_1 + \overrightarrow{b}_2,$$

where n_0 - is the average value of the plasma density, $\widetilde{n}_0$ - is the electron density perturbation caused by the MHD pump Alfvén wave, the index "0" in all expressions correspond to the pump wave, and indexes "1" and "2" – correspond to the first and second KAW respectively.

To obtain the dispersion relation for the kinetic Alfvén waves, we use the plasma approximation:

$$n_{1i} = n_{1e}, \tag{1}$$

where n_{1e} and n_{1i} - are the perturbations of electron and ion densities respectively. From the equation of motion and the continuity equation, we find the expression for n_{1e} related to the KAW. Expression for the perturbed ion density is found from the Vlasov equation Shukla (2000). From (1) we have the relation between the vector potential $\overrightarrow{A}_1$ and the scalar potential φ_1. The second relation between $\overrightarrow{A}_1$ and φ_1 we can find from the perpendicular projection of the Ampere law:

$$-k_1^2 k_{1z} A_{1z} = \frac{4\pi}{c} k_{1x} j_{1x}. \tag{2}$$

Equating the expression for $\overrightarrow{A}_1$ form (1) and (2) we have the nonlinear equation circumscribing the dispersion of the kinetic Alfvén waves Yukhimuk (1998):

$$\left[\frac{V_{1f}^2}{V_A^2}\left(1+\alpha_1\left(\frac{\chi_{1e}}{\mu_{1i}}-1\right)\right)-\left(1+\alpha_1\frac{T_e}{T_i}\right)\right]\varphi_1 = Q_{1NL}. \tag{3}$$

Here nonlinear term Q_{1NL} is given by

$$Q_{1NL} = \frac{1}{iek_{1z}}F_{1ez} - \frac{m_e}{m_i}\frac{V_{1f}^2}{V_A^2}\left(1+\chi_{1e}\right)\frac{1}{iek_{1x}}\left(F_{1ex} - i\frac{\omega_{Be}}{\omega_1}F_{1ey}\right) -$$

$$-\frac{1}{\delta_i^2 k_{1z}^2}\frac{m_i}{e}\left(1+\chi_{1e}\right)\left(\frac{n_{1e}^L}{n_0}V_{1ex}^L\right),$$

where $V_{Te} = \sqrt{\frac{T_e}{m_e}}$ is the thermal electron velocity, $\chi_{1e} = k_{1x}^2\delta_e^2$, $\delta_e = \frac{c}{\omega_{pe}}$ is the electron inertial length, $\delta_i = \frac{c}{\omega_{pi}}$ is the ion inertial length, $\alpha_1 = 1 - \Gamma_0\left(\mu_{1i}\right) - \frac{2\omega_1^2\Gamma_1(\mu_{1i})}{\omega_1^2-\omega_{Bi}^2}$, $\Gamma_{0,1}\left(\mu_{1i}\right) = I_{0,1}\left(\mu_{1i}\right)exp\left(-\mu_{1i}\right)$, $I_{0,1}$ is the zero-(first) order modified Bessel function, $\mu_{1i} = k_{1x}^2\rho_i^2$, $\rho_i = \frac{V_{Ti}}{\omega_{Bi}}$ is the ion thermal gyroradius. If in the plasma propagate only noninteracting kinetic Alfvén waves ($Q_{1NL}=0$), from (3) we obtain the dispersion equation for KAWs as:

$$\omega_1^2=\frac{1+\alpha_1\frac{T_e}{T_i}}{1+\alpha_1\left(\frac{\chi_{1e}}{\mu_{1i}}-1\right)}k_{1z}^2V_A^2. \tag{4}$$

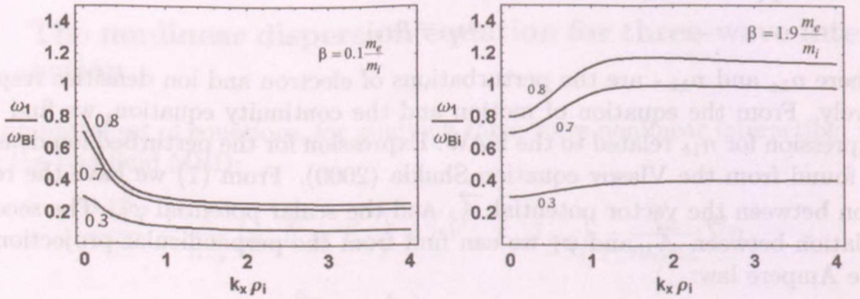

Figure 1: Dependence of the normalized kinetic Alfvén frequencies on the normalized wavenumbers $k_{1x}\rho_i$, $k_{1z}\delta_i$ and plasma parameter β.

In absence of the pump wave from (3) for $\mu_{1i} << 1$ the linear dispersion equation for KAW is:

$$\omega_1^2=\frac{1-\frac{\omega_1^2}{\omega_{Bi}^2}+\mu_{1S}}{1-\frac{\omega_1^2}{\omega_{Bi}^2}+\chi_{1e}}k_{1z}^2V_A^2. \tag{5}$$

Here $\mu_{1S}=\frac{k_{1x}^2V_S^2}{\omega_{Bi}^2}$, $V_S=\sqrt{\frac{T_e}{m_i}}$ - is the ion-sound velocity. In (4) and (5) we are take into account effects due to finite Larmor radius of ions (μ_{1S}) and effects due to the electron inertial (χ_{1e}). Using expression (3), the dispersion equation for kinetic Alfvén waves is found as:

$$\varepsilon_{1A}\Phi_1=\mu_{1A}\left(E_{0x}\Phi_2^*\right), \tag{6}$$

where

$$\mu_{1A}=-i\frac{\omega_1}{\omega_0}\frac{e}{m_e}\frac{V_A^2}{\omega_{Be}^2}\frac{k_{0z}k_{2x}k_{1z}^2}{k_{2z}}\frac{1}{1+\chi_{1e}},$$

$$\varepsilon_{1A}=\omega_1^2-\frac{1+\mu_{1S}}{1+\chi_{1e}}k_{1z}^2V_A^2,$$

$$\Phi_1 = \frac{e\varphi_1}{T_e}.$$

The dispersion equation for the second kinetic Alfvén wave follows from (6) when the indexes "1" and "2" are exchanged. Using dispersion equations for two KAW we can find a nonlinear dispersion equation describing three-wave interaction (decay of the MHD Alfvén pump wave into two KAWs):

$$\varepsilon_{1A}^{*}\varepsilon_{2A} = \mu_{1A}^{*}\mu_{2A}\left|E_{0x}\right|^{2}. \tag{7}$$

The presence of the pump wave leads to the energy transfer from MHD Alfvén wave to the kinetic Alfvén waves, which increase their amplitudes. Assuming in (7) $\omega_1 = \omega_{1r} + i\gamma$, $\omega_2 = \omega_{2r} + i\gamma$, (where $|\gamma| << \omega_{1r}, \omega_{2r}$) and expanding ε_{1A} and ε_{2A} in Taylor series in the small parameter $i\gamma$, we obtain an expression for the instability growth rate:

$$\gamma = \sqrt{\frac{W}{16}}\left(\mu_{1i}\mu_{2i}\right)^{\frac{1}{4}}\frac{\omega_{pe}}{\omega_{Be}}\omega_0,$$

where $W = \frac{|E_0|^2}{4\pi n_0 T_e}$.

3. Conclusion

One of the most interesting phenomena appearing on the Sun is the high temperature of the solar corona, which reaches $10^6 K$ (compare with $5\cdot 10^3 K$ at the level of the photosphere). For maintaining such a high temperature and compensating the radiative cooling the constant inflow of energy is needed. The necessary energy is considered to be carried by Alfvén waves, excited in the lower layers of the atmosphere of the Sun. But Alfvén waves are weakly damping. On the other hand, the damping of kinetic Alfvén waves is strong. Therefore, they can effectively heat the solar corona. As an application of our theoretical results, obtained in this work, we consider some regions of the solar atmosphere where plasma parameter is small. For typical values of coronal plasma parameters $B_0 = 100G$, $T_e = 10^6 K$, $n_0 = 10^{10} sm^3$ we have the instability growth rate $\gamma \approx 6\cdot 10^2 s^{-1}$ and the time of instability development $\tau \approx 2\cdot 10^{-3} s$. Therefore, the presented process can reduce the transmission of the energy from large-scale MHD Alfvén waves to small-scale KAW, which are able to heat the corona.

Acknowledgments

Viktor Fedun acknowledges the financial support by the Organizing Committee of the NATO ARW "Turbulence, Waves, and Instabilities in the Solar Plasma".

References

Coroniti, F. V., Kennel, C. F. 1970, J. Geophys. Res., 75, 1863

Stefant, R. J. 1970, Phys. Fluids., 13, 440

Hasegawa, A., Chen, L. 1976, Phys. Fluids., 19, 1924

Yukhimuk, V.A., Voitenko, Yu. M., Fedun, V. M., Yukhimuk, A.K. 1998, J. Plasma Phys., 60, 485

Shukla, P.K., Stenflo, L. 2000, J. Plasma Phys., 64, 125

PART FIVE

TURBULENCE AND RECONNECTION IN THE SOLAR CORONA

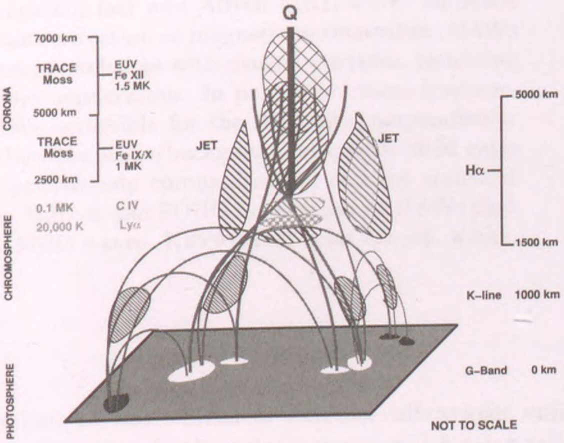

References

Wendel, F. V., Hamel, C. F. 1970, J. Geophys Res., 75, 1890

Stefant, R. J. 1970, Phys. Fluids, 13, 440

Hasegawa, A., Chen, L. 1976, Phys. Fluids, 19, 1924

Yukhimuk, V.A., Voitenko, Yu. M., Fedun, V. M., Yukhimuk, A.K. 1998, Plasma Phys., 60, 485

Shukla, P.K., Stenflo, L. 2000, J. Plasma Phys., 64, 125

NONLINEAR WAVE DYNAMICS IN THE DISSIPATION RANGE: IMPACT ON CORONAL HEATING PROCESSES

Y. Voitenko[1,2] **and M. Goossens**[1]
[1]Centre for Plasma Astrophysics, K.U.Leuven
Celestijnenlaan 200B, 3001 Heverlee, Belgium
[2]Main Astronomical Observatory, Dept of Space Plasma Physics
Zabolotnoho 27, 03680 Kyiv, Ukraine
E-mail: [1]`Yuriy.Voitenko@wis.kuleuven.ac.be`

Abstract

There is abundant observational evidence that the ions in the solar corona (in particular, O^{+5}) are heated anisotropicaly, predominantly across the background magnetic field. This heating is usually attributed to the dissipation of ion-cyclotron waves. We study an alternative possibility with the dissipation range in the solar corona formed by the kinetic Alfvén waves (KAWs) which are very short- wavelengths across the magnetic field. Instead of transport of MHD wave energy towards to the range of ion-cyclotron waves, we study transport into the dissipation range of KAWs. We show that the nonlinear excitation of short-wavelength (of the order 10 m) KAWs in the extended solar corona and solar wind can be provided by upward-propagating fast and Alfvén MHD waves launched from the coronal base by the convection or magnetic reconnection. KAWs are very efficient in the energy exchange with plasma particles, providing plasma heating and particles acceleration. In particular, these transversal wavelengths make KAWs accessible for the stochastic perpendicular heating of oxygen ions when the wave/background magnetic field ratio exceeds 0.005. Both the quasi-steady coronal heating and the transient heating events observed by Yohkoh and SOHO may be due to KAWs that are nonlinearly excited by MHD waves. KEYWORDS: solar corona, waves, instabilities

1. Introduction

Spectroscopic SOHO observations of the widths of extreme ultraviolet emission lines indicate that ions are very hot in the solar corona at 2-5 solar radii. Moreover, the ion kinetic temperatures seem to be highly anisotropic with the perpendicular (with respect to the background magnetic field) temperature being much larger than the parallel temperature (Dodero et al., 1998; Cranmer et al. 1999). A similar trend, though not so pronounced, is observed in the solar wind, where the perpendicular temperature of ions is higher than the parallel and the ion magnetic moments increase with the distance from the Sun (Marsch, 1991). These observations suggest that the ions are energized (heated and/or accelerated) anisotropically, mainly across the magnetic field.

The perpendicular heating of the ions in the solar corona and solar wind has been mainly attributed to the ion-cyclotron damping of high-frequency Alfvén waves (see recent papers by Marsch and Tu, 2001, and Hollweg and Markovskii, 2002, and references therein). The ion-cyclotron sweep has been widely discussed as a mechanism for the energization of the solar atmosphere by relatively high-frequency ($1 \div 10^3$ s^{-1}) Alfvén waves injected at the base of solar corona (e.g., Tu & Marsch 1997; Leamon et al. 2000). Numerous magnetic reconnection events at the base of the solar corona can provide a possible source for these waves (McKenzie et al. 1995), and the decrease of the ion-cyclotron frequencies with the distance from the Sun gives rise to the cyclotron damping of these waves. Most attention has been given to the cyclotron sweep of Alfvén waves due to the parallel inhomogeneity of the magnetic field (length scale $L_\parallel \sim 10^{10}$ cm). However, the waves also undergo strong phase mixing due to the perpendicular density inhomogeneity (length scale $L_\perp \sim 10^5 \div 10^7$ cm). The perpendicular wave vector increases with distance z as $k_\perp = -(\omega/V_A)(z/L_\perp)$, and at 2-3 solar radii the Alfvén waves with $\omega = 1 \div 100$ s^{-1} would attain $k_\perp \rho_p \gg 1$, where ρ_p is the ion (proton) gyroradius. However, they should Landau-damp well before, at the distances $< 10^{10}$ cm.

Another possibility is that the ion-cyclotron waves are excited in-situ in the solar corona and solar wind. The nonlinear excitation by MHD turbulence - turbulent Kolmogorov cascade towards higher frequencies - has been discussed as an alternative for the cyclotron sweep mechanism (Hollweg 1986; Li et al. 1999). The ion-cyclotron waves can also be excited linearly by the perpendicular currents developed by finite-amplitude MHD waves (Markovskii, 2001; Markovskii and Hollweg, 2001). Yet another possibility is the excitation by plasma outflows from coronal reconnection events (Voitenko and Goossens, 2002a).

All of these schemes imply that the wave dissipation range is formed by the high-frequency waves with frequencies close to the local ion-cyclotron frequencies. We note, however, that the ion-cyclotron scenario is not free from difficulties and is not the only possibility. An alternative possibility is that the dissipation range is formed by the waves that are short-wavelength across the magnetic field. So, the turbulent cascade in Alfvénic turbulence is highly anisotropic: it does not change the parallel wavenumbers that determine the wave frequencies, but increases the perpendicular wavenumbers (Zank & Matthaeus 1992; Leamon et al. 2000). The phase mixing in a transversally nonuniform plasma works in the same direction. These mechanisms, again, are too slow for providing the necessary rate of the transfer of wave energy from the MHD length scales, where the bulk of the energy resides, to the dissipative length scales, which are of the order of the proton gyroradius ρ_p.

In the present paper we investigate the possibility that the dissipation range is formed by the Alfvén waves, which have a sufficiently short wavelength across the magnetic field for the dissipative effects to become significant. An extension of the low-frequency Alfvén wave branch into the region of finite $k_\perp \rho_p$ ($k_\perp$ is the wavenumber component that is perpendicular to the background magnetic field) is called a kinetic Alfvén wave (KAW).

The energy reservoir is provided by the low-frequency large-scale MHD waves that are launched in the corona by the photospheric motions or excited at the coronal base by magnetic restructuring. However, instead of following local nonlinear interactions among MHD waves, which are rather slow, we study the nonlinear excitation of KAWs which are already in the dissipative range. We show that the presence of the finite-amplitude MHD waves, polarized in the sense of Alfvén and/or fast wave, gives rise to the nonlinear excitation of KAWs via three-wave resonant interaction. This process provides a jump-like transport of MHD wave energy directly in the dissipation range. When the excited KAWs have a sufficiently short wavelength and have a sufficient amplitude, they give rise to a stochastic acceleration of the ions across magnetic field.

2. Nonlinear excitation of short-scale kinetic Alfvén waves by large-scale MHD waves

In terms of the effective density potential $\phi = (T_e/e)\ln(n_e/n_0)$, the eigenmode equation for KAWs is (Voitenko and Goossens 2002b):

$$\left(\frac{\partial^2}{\partial t^2} - V_A^2 K^2 \nabla_\parallel^2 - 2\gamma_{\rm d}\frac{\partial}{\partial t}\right)\phi = N_{\rm tot}. \tag{1}$$

$\gamma_{\rm d}$ is the linear damping/growth rate due to wave-particle interaction, K is the dispersion function in the perpendicular wavenumber space,

$$K^2 \approx \frac{1+\mu_T}{1+\chi_e}, \tag{2}$$

where $\mu_T = \rho_T^2 k_\perp^2$, $\rho_T^2 = V_T^2/\Omega_p^2$, $V_T^2 = T/m_p$, $T = T_p + T_e$, $\Omega_p = eB_0/m_pc$ is the ion-cyclotron frequency, $V_A = B_0/\sqrt{4\pi n m_p}$ is the Alfvén velocity, $\beta = V_T^2/V_A^2$

is the gas/magnetic pressure ratio, $\chi_e = \delta_e^2 k_\perp^2 = \beta^{-1}(m_e/m_p)\,\mu_T$, δ_e is the electron inertial length. The KAW dispersion function $K > 1$ for $m_e/m_p < \beta < 1$, and $K < 1$ for $\beta < m_e/m_p$.

The nonlinear part N_{tot} of (1) is quite complicated and is given by Voitenko and Goossens (2002). The nonlinear second-order terms that appear in N_{tot} come from the electron and ion continuity equations, and from the parallel and perpendicular components of the Ampere law. The nonlinear interaction is due to the KAW dispersion and the finite values of the number density fluctuations n/n_0, magnetic compressibility $B_\parallel/B_0$, and parallel velocity of electrons $v_{e\parallel}/V_A$ in KAWs.

2.1. Parametric decay of MHD waves into KAWs

The parametric decay instability is a well-known process for the nonlinear transfer of energy from a finite-amplitude pump wave to secondary (sometime called daughter) waves (Galeev and Sagdeev, 1979). The matching conditions relate the frequencies and the wavenumbers of participating waves are important for an efficient energy transfer. We concentrate here on the decay instabilities of the large-scale pump MHD waves (Alfvén or fast magnetoacoustic) into KAWs, AW(FW)=KAW+KAW, which are made possible by scalar nonlinear interactions (Voitenko and Goossens, 2002b). These decay instabilities result in a jump-like spectral transport of MHD wave energy directly into the dissipation range (i.e., dissipative length scales).

It is useful to factorize the KAW wave functions of the excited KAWs ϕ_1 and ϕ_2 into an exponential phase dependence and a slowly varying amplitude, $\Phi_{1,2} = \Phi_{1,2}(t)$:

$$\phi_{1,2} = \Phi_{1,2} \exp\left(-i\omega_{1,2}t + i\mathbf{k}_{1,2}\cdot\mathbf{r}\right).$$

The equations for the resonant short-scale Alfvén waves 1 and 2, coupled to the large-scale pump wave P, are then obtained from the nonlinear eigenmode equation (1) as

$$\left[\frac{\partial}{\partial t} - \gamma_{\mathrm{d}1}\right]\Phi_1 = U_{1,-2,\mathrm{P}}\Phi_2^* b_{\mathrm{P}}; \tag{3}$$

$$\left[\frac{\partial}{\partial t} - \gamma_{\mathrm{d}2}\right]\Phi_2^* = U_{-2,1,-\mathrm{P}}\Phi_1 b_{\mathrm{P}}^*, \tag{4}$$

$b_{\mathrm{P}} = B_{\mathrm{P}}/B_0$ is the normalized magnetic field of the pump wave. The coupling coefficients are

$$U_{1,-2,\mathrm{P}} = \left(-i\omega_1\Phi_2^* b_{\mathrm{P}}\right)^{-1} N_{\mathrm{tot}}\left(1;-2;\mathrm{P}\right),$$

$$U_{-2,1,-\mathrm{P}} = \left(i\omega_2 \Phi_1 b_{\mathrm{P}}^*\right)^{-1} N_{\mathrm{tot}}\left(-2;1;-\mathrm{P}\right),$$

where N_{tot} have to be calculated from by eliminating all the pump variables in favor of b_{P}, and by eliminating all the KAW variables in favor of Φ. Then, looking for exponentially growing (or decaying) solutions of the system (3-4), $\Phi_{1,2} \sim \exp\left(\gamma_{\mathrm{tot}} t\right)$, we find the total growth (or damping) rate

$$\gamma_{\mathrm{tot}} = \frac{\gamma_{\mathrm{d}1} + \gamma_{\mathrm{d}2}}{2} \pm \sqrt{\left(\frac{\gamma_{\mathrm{d}1} - \gamma_{\mathrm{d}2}}{2}\right)^2 + \gamma_{NL}^2}, \tag{5}$$

where γ_{NL} is the nonlinear growth rate - the rate of the nonlinear pumping of MHD wave energy into daughter KAWs:

$$\gamma_{NL} = \sqrt{U_{1,-2,\mathrm{P}} U_{-2,1,-\mathrm{P}}}\, |b_{\mathrm{P}}|\,. \tag{6}$$

2.2. Nonlinear excitation of KAWs by MHD fast waves

We focus on the decay FW=KAW+KAW, where the pump is a FW with a frequency ω_{P} propagating at an angle to the background magnetic field, $\mathbf{k}_{\mathrm{P}} = (k_{\mathrm{P}\perp}; 0; k_{\mathrm{P}z})$, the z-axis is parallel to $\mathbf{B}_0$. As we are interested in a non-local process of the decay into KAWs with high perpendicular wavenumbers, $\mathbf{k}_{2\perp}, \mathbf{k}_{1\perp} \gg \mathbf{k}_{\mathrm{P}\perp}$, we have $-\mathbf{k}_{1\perp} \approx \mathbf{k}_{2\perp} \equiv \mathbf{k}_{\perp}$ and $K\left(k_{2\perp}\right) \approx K\left(k_{1\perp}\right) \equiv K$. The frequency matching condition,

$$\omega_1 + \omega_2 - \omega_{\mathrm{P}} = 0. \tag{7}$$

and the parallel wavenumber matching condition,

$$k_{1z} + s_2 \left|k_{2z}\right| = k_{\mathrm{P}z}, \tag{8}$$

can be solved for $s_2 = -1$ (anti-parallel propagating decay waves), giving frequencies of decay waves for given $K = K\left(k_{\perp}\right)$ as

$$\omega_1 = \frac{1}{2}\left(1 + \frac{k_{\mathrm{P}z}}{k_{\mathrm{P}}} \frac{K}{K_{\mathrm{P}}}\right)\omega_{\mathrm{P}}; \quad \omega_2 = \frac{1}{2}\left(1 - \frac{k_{\mathrm{P}z}}{k_{\mathrm{P}}} \frac{K}{K_{\mathrm{P}}}\right)\omega_{\mathrm{P}}. \tag{9}$$

For $s_2 = 1$ (parallel propagating decay waves), we find from (7) that the KAWs' wavenumbers should be fixed, $\mu_T = \mu_T^* \equiv (1+\beta)\, k_{\mathrm{P}\perp}^2 / k_{\mathrm{P}z}^2$. The decay into parallel propagating KAWs is thus selective (restricted by the matching conditions). For $s_2 = -1$ (anti-parallel propagating decay waves), the matching conditions reduce to the requirement $\omega_2 > 0$, which can be satisfied in a wide range of perpendicular wavenumbers $\mu_T < \mu_T^*$. The coupling coefficients, the nonlinear growth rate, and further details of the decay FW=KAW+KAW are given in Voitenko and Goossens (2002b).

2.3. Nonlinear excitation of KAWs by MHD Alfvén waves

We now focus on a pump AW with a frequency ω_P and a wave vector

$$\mathbf{k}_\mathrm{P} = (k_{\mathrm{P}\perp}; 0; k_{\mathrm{P}z}), \tag{10}$$

that decays into KAWs with $k_{1\perp} \approx -k_{2\perp} \gg k_{\mathrm{P}\perp}$ and with approximately equal dispersions, $K\left(k_{1\perp}^2\right) \approx K\left(k_{2\perp}^2\right)$.

The frequency matching condition, $\omega_1 + \omega_2 = \omega_\mathrm{P}$, and the parallel wavenumber matching condition, $s_1\omega_1 + s_2\omega_2 = \omega_\mathrm{P} K$, can be satisfied only for antiparallel propagation of the daughter KAWs (we take $s_\mathrm{P} = k_{\mathrm{P}z}/\left|k_{\mathrm{P}z}\right|$). So, assuming $s_1 = 1$, we must have $s_2 = -1$. This determines the KAW frequencies as

$$\omega_1 = \frac{1+K}{2}\omega_\mathrm{P}; \quad \omega_2 = \frac{1-K}{2}\omega_\mathrm{P}. \tag{11}$$

Hence, the process is only possible if $K < 1$, i.e., in a very low-β plasma ($\beta < m_e/m_p$). The KAWs in a $\beta < m_e/m_p$ plasma are sometimes called inertial Alfvén waves, because their dispersion is determined mainly by the parallel electron inertia.

In the dipole approximation, $-\mathbf{k}_{1\perp} \approx \mathbf{k}_{2\perp} \equiv \mathbf{k}_\perp$, the coupling coefficients of KAWs with a pump MHD Alfvén wave are reduced to quite simple expressions:

$$U_{1,-2,\mathrm{P}} = -U_{-2,1,-\mathrm{P}} = i\frac{1}{K}\left(\frac{m_p}{m_e}\beta - K^2\right)\frac{\delta_e^2 k_\perp^2}{1+\delta_e^2 k_\perp^2} V_A\left(\mathbf{e}_\mathrm{P}\cdot\mathbf{k}_\perp\right), \tag{12}$$

$\mathbf{e}_\mathrm{P}$ is the magnetic polarization vector of the pump wave, $\mathbf{e}_\mathrm{P} = \mathbf{B}_\mathrm{P}/B_\mathrm{P}$. The total growth rate of KAWs is given by (5), where the nonlinear pumping rate is found from (6) as

$$\gamma_{NL} = \sqrt{\frac{m_p}{m_e}}\left|1 - \frac{m_p}{m_e}\beta\right| \frac{\delta_e^3 k_\perp^3}{\sqrt{1 + \frac{m_p}{m_e}\beta\delta_e^2 k_\perp^2}\,\left(1 + \delta_e^2 k_\perp^2\right)^{3/2}} \left|b_\mathrm{P}\right| \Omega_p. \tag{13}$$

As long as β is distinctly smaller than m_e/m_p, the MHD Alfvén waves decay very strongly, exciting KAWs. However, $\gamma_{NL} \to 0$ for $\beta \to m_e/m_p$. The decay is impossible for $\beta > m_e/m_p$, where the resonant conditions cannot be satisfied.

These features of the nonlinear growth rate, together with the dissipative properties of KAWs, create an interesting feedback loop for the plasma/MHD wave flux system. When the flux of MHD Alfvén waves enters the region where $\beta < m_e/m_p$, nonlinearly driven KAWs are generated and tend to heat the plasma up to the level where the β is kept slightly below m_e/m_p, $\beta = \beta_c \lesssim$

m_e/m_p. When used in (13), this particular value β_c provides a dynamical equilibrium in which the nonlinear growth rate γ_{NL}, at which the energy is pumped in the plasma via intermediate KAWs, balances the energy lost from the plasma due to emission, thermal conduction and plasma acceleration. With different powers of the launched MHD Alfvén flux, the interplay of these processes can set up different regimes - from weak additional heating in the vicinity of the transition point $\beta = m_e/m_p$, to the creation of an extended region where $\beta \lesssim m_e/m_p$, which ends up with accelerated flows of heated plasma, where $\beta > m_e/m_p$.

3. MHD wave decay and anisotropic plasma heating in the solar corona

The nonlinear properties of KAWs provide a very promising plasma energization mechanism that can be responsible for the plasma heating and solar wind acceleration in the coronal holes. Let us imagine an initial static equilibrium where the plasma is heated locally, only at low heights (e.g., by acoustic shock waves), and the plasma temperature and density decrease with heliocentric distance along open magnetic field lines. The gas/magnetic pressure ratio β should also decrease, practically to zero, at the distance of the order of the hydrostatic scale height. Now, assume a flux of MHD waves, launched in the corona by photospheric motions (or by magnetic reconnection events at the coronal base).

3.1. Quasi-steady plasma heating

The flux of MHD Alfvén waves propagates upward unattenuated up to the height where β becomes equal to m_e/m_p. As soon as β drops below m_e/m_p, the MHD Alfvén waves undergo a strong parametric decay into KAWs. Due to their short perpendicular wavelengths, the nonlinearly excited KAWs dissipate via collisional or collisionless wave-particle interaction, which, in turn, gives rise to the plasma heating and particles acceleration. Thus, the flux of KAWs, that propagates further upward, can easily increase β again well above m_e/m_p in the high corona and provide the energy source for the solar wind acceleration. The eventual result of this should be a new, dynamic equilibrium, in which (i) the first transition point from $\beta > m_e/m_p$ to $\beta < m_e/m_p$ is shifted to larger heights (result of the dissipation of downward KAW flux); (ii) there is an extended region where β is kept (by the dynamical back reaction on the KAWs damping) at a level below m_e/m_p, so as to provide an efficient conversion of the upward MHD Alfvén flux into two counter-streaming KAW fluxes; (iii) there is a second transition point from $\beta < m_e/m_p$ to $\beta > m_e/m_p$, beyond which the plasma is strongly heated by the upward KAW flux and expands forming solar wind.

Let us turn to numerical estimates. We take plasma parameters that are typical for coronal holes. The temperatures and densities of electrons in coronal holes are rather well determined (see Wilhelm et al., 1998, and references therein). Near critical point, we take $\beta = 0.99 m_e/m_p$, $T_e = 10^5$ K, $n_e = 3 \times 10^7$ cm^{-3}, magnetic filed $B_0 = 5$ G and $T_p/T_e = 1.5$, $\Omega_p = 5 \times 10^4$ s^{-1}. Then the electron collisional frequency ν_e may be estimated as $\nu_e \sim 100$ s^{-1}. As the collisional (resistive) dissipation of KAWs is stronger than the Landau damping for low-frequency waves $\omega_k < 10$ s^{-1}, we use the collisional damping as an estimate for the dissipation rate:

$$\gamma_{\mathrm{d}1} = \gamma_{\mathrm{d}2} = \gamma_{\mathrm{d}} = -0.25\nu_e \frac{k_\perp^2 \delta_e^2}{1 + k_\perp^2 \delta_e^2}, \tag{14}$$

and

$$\gamma_{\mathrm{tot}} = \gamma_{\mathrm{d}} + \gamma_{NL}.$$

The maximal growth $\gamma_{\mathrm{tot}} \approx 0.6$ s^{-1} is attained at $k_\perp^2 \delta_e^2 \approx 1$ if we take an (underestimated) amplitude $b_{\mathrm{P}} = 0.0023$ for the MHD waves, participating in elementary three-wave interactions. Formally, we can have a much higher growth rate with different wave and plasma parameters, but we are restricted by the condition of weak growth/damping, i.e., γ_{tot} should be smaller than ω_{P}, $\gamma_{\mathrm{tot}} < \omega_{\mathrm{P}}$, which can be violated for the low-frequency MHD waves. In this respect we note that the wave flux, coming from the $\beta > m_e/m_p$ region, meets initially very small values of $1 - \beta m_p/m_e$, satisfying the condition $\gamma_{\mathrm{tot}} < \omega$, but providing fast enough conversion of wave energy. This mechanism is working in such a way as to keep β very close to m_e/m_p, so that the values $\beta = 0.99 m_e/m_p$ can be reasonable. But, for any $\beta < m_e/m_p$, the fastest growing waves have perpendicular wavenumbers in the range $k_\perp^2 \delta_e^2 = 1 \div 3$.

An essential feature of the heating by Alfvén wave decay is its relation to the region of $\beta \lesssim m_e/m_p$ at some distance from the Sun. The AW-driven KAW flux will dissipate fast in the vicinity of the critical level where $\beta \sim m_e/m_p$ (with the rate (14) in collisional regime), and will thus provide a localized quasi-steady heating.

At the same time, the part of the wave flux polarized in the sense of a fast mode can decay and heat plasma in the wide range for β, $\beta > m_e/m_p$. The heating by the FW-driven KAWs can be distributed over large distances from the Sun because the condition $\beta > m_e/m_p$ is fulfilled in the most part of corona and in the solar wind. The progressive refraction of FWs with heliocentric distance could provide the disturbed source for KAWs.

3.2. Transient brightenings

Transient brightenings on time scales of about one minute or shorter are observed in the low corona by Yohkoh and SOHO (blinkers, nano- and microflares) and attract an increasing interest (Shimizu et al., 1992; Innes et al., 1997; Berger et al., 1999; Roussev et al., 2001; Berghmans et al., 2001). It is believed that most of these explosive events are closely related to the interaction of magnetic fluxes, separated by current sheets. Fushiki and Sakai (1994) have shown that fast waves can be produced in the solar atmosphere by a pinching current sheet.

We have shown (Voitenko and Goossens, 2002b), that the fast waves emitted from the magnetic reconnection events heat the surrounding plasma by heavily damped KAWs that are excited by the parametric decay instability of the fast waves. For the FW with amplitude $b_{\mathrm{P}} = 0.1$ and frequency $\omega_{\mathrm{P}} = \nu_e = 30$ s^{-1}, pumped from the current sheet, we estimate the typical time for the decay instability into KAWs to develop and the plasma to heat, $\tau_{\mathrm{tot}} \sim \tau_{NL} \sim \tau_c \sim 1$ s. This process provides fast local heating of coronal plasma in the volume of about $10^3 \times 10^3 \times 10^3$ km^3.

3.3. Stochastic ion heating by KAWs

The nonlinear driven KAWs with $k_\perp^2 \delta_e^2 \sim 1$ are almost electrostatic in sense that their electric field is almost parallel to the wave vector, $|\mathbf{k} \cdot \mathbf{E}| \gg |\mathbf{k} \times \mathbf{E}|$. In this case the velocity of the polarization drift of the ions becomes large, which makes the KAWs available for the stochastic ion energization (heating) across the magnetic field. Stochastic ion heating by (quasi-) perpendicular electrostatic waves has been studied by Stasiewicz et al. (2000). The efficiency of this process can be estimated on the basis of individual particles motion in wave fields (Balikhin et al., 1993). Hence, we consider the motion of two ions that are initially close in the phase space, $|\delta \mathbf{r}| = |\mathbf{r}_1 - \mathbf{r}_2| \ll |\mathbf{r}_1|, |\mathbf{r}_2|$, and $|\delta \mathbf{v}| = |\mathbf{v}_1 - \mathbf{v}_2| \ll |\mathbf{v}_1|, |\mathbf{v}_2|$. From the ion equation of motion, we obtain for the perpendicular components of the velocity difference:

$$\frac{d}{dt}\delta v_x = \frac{q_i}{m_i}\frac{\partial E_x}{\partial \mathbf{r}_\perp}\delta \mathbf{r}_\perp + \Omega_i \delta v_y,$$

$$\frac{d}{dt}\delta v_y = -\Omega_i \delta v_x,$$

where the x-axis is taken in the direction of $E_\perp$. Differentiating the first equation with respect to time, and eliminating δv_y by the use of the second equation, we obtain the linearized equation for the x-component of the velocity difference:

$$\frac{d^2}{dt^2}\delta v_x = \left[\frac{q_i}{m_i}\frac{\partial E_x}{\partial x} - \Omega_i^2\right]\delta v_x .$$

Chaotic energization occurs when the difference between the particle velocities grows exponentially with time,

$$\delta v_x = \delta v_{x0}\exp\left(\gamma_{\rm ch} t\right).$$

This corresponds to

$$\gamma_{\rm ch}^2 = \left(\frac{q_i}{m_i}\frac{\partial E_x}{\partial x} - \Omega_i^2\right) > 0.$$

We can write the condition of the stochastic heating of ions i in terms of the wave magnetic field B_y as

$$\frac{k_x V_A}{\Omega_i}\frac{1+\mu_p}{K}\frac{B_y}{B_0} > 1. \tag{15}$$

Hence, the condition for the stochastic heating of oxygen ions O^{+5} is

$$\frac{m_i}{5m_p}\frac{k_x V_A}{\Omega_p}\frac{1+\mu_p}{K}\frac{B_y}{B_0} > 1.$$

For the nonlinearly excited KAWs with $k_x\delta_e \gtrsim 1$ we obtain the condition for the relative KAW amplitudes as

$$\frac{B_y^{KAW}}{B_0} > \frac{5m_p}{m_i}\sqrt{\frac{m_e}{m_p}}\frac{K}{k_x\delta_e\left(1+\mu_p\right)} = (1 \div 3)\times 10^{-3}. \tag{16}$$

Since the amplitudes of coronal MHD wave are in the range $B^{MHD}/B_0 = 0.05 \div 0.1$, the condition (16) becomes realistic even for a small fraction ($\lesssim 0.1$) of MHD wave energy transferred to KAWs, and the O^{+5} ions can be strongly heated in the perpendicular direction. However, due to the high efficiency of the nonlinear excitation of KAWs, we could expect much more energy to be transferred to KAWs, of the order of the initial MHD wave energy. In this case the protons can also be stochastically heated by KAWs. The condition for stochastic proton heating is $B_y^{KAW}/B_0 \gtrsim 0.01$.

4. Conclusions

We have studied the parametric excitation of KAWs by pump Alfvén and fast waves. The main conclusion is that these elementary nonlinear processes can strongly accelerate the spectral evolution of wave energy from MHD length scales to dissipative short length scales in the solar corona. The parametric decay instability of a pump MHD Alfvén wave into KAWs is only possible in a very low-β plasma, $\beta < m_e/m_p$. The pump fast magneto-acoustic wave can drive KAWs in a low-β plasma, $\beta < 1$.

The nonlinear excitation of KAWs in the extended solar corona can be provided by upward-propagating (Alfvén and fast) MHD waves launched from the convection zone or excited by the magnetic reconnection events at the coronal base. Short transversal wavelengths of the order 10 m make KAWs accessible for the stochastic heating of oxygen ions if the wave/background magnetic field ratio exceeds 0.005. The resulting ion heating is primarily in the direction perpendicular to the background magnetic field. This process provides an alternative to the ion-cyclotron explanation for the intense transverse heating of oxygen ions observed by SOHO at $2 \div 4$ solar radii. Similarly, the impulsive heating events at the coronal base can be due to the dissipation of KAWs nonlinearly driven by MHD waves, excited by the collapsing current sheets.

Acknowledgments

This work was supported by the FWO research grant G.0344.98. Y. V. acknowledges the financial support from the conference organizers.

References

Balikhin, M., Gedalin, M., Petrukovich, A. 1993, Phys. Rev. Lett., 70, 1259

Berger, T. E., De Pontieu, B., Schrijver, C. J., and Title, A. M. 1999, ApJ, 519, L97

Berghmans, D., McKenzie, D., and Clette, F. 2001, A&A, 369, 291

Cranmer, S. R., Field, G. B., Kohl, J. L. 1999, ApJ, 518, 937

Dodero, M. A., Antonucci, E., Giordano, S., and Martin, R. 1998, Solar Phys., 183, 77

Fushiki, T. and Sakai, J.-I. 1994, Solar Phys., 150, 117

Galeev, A. A., Sagdeev, R. Z. 1979, in M. A. Leontovich (ed.), Reviews of Plasma Physics, Vol. 7., Plenum, New York, p. 1

Hollweg, J. V. 1986, J. Geophys. Res., 91, 4111

Hollweg, J. V., and Markovskii, S. A. 2002, J. Geophys. Res., 107, SSH 1

Innes, D. E., Inhester, B., Axford, W. I. and Wilhelm, K. 1997, Nature, 386, 811

Leamon, R. J., Matthaeus, W. H., Smith, C. W., Zank, G. P., Mullan, D. 2000, ApJ, 537, 1054

Li, X., Habbal, S. R., Hollweg, J. V., Esser, R. 1999, J. Geophys. Res., 104, 2521

Markovskii, S. A. 2001, ApJ, 557, 337

Marsch, E. 1991, in R. Schwenn and E. Marsch (eds.), Physics of the Inner Heliosphere, Vol. II, Springer Verlag, Heidelberg, Germany, p. 45

Marsch, E., Tu, C. Y. 2001, J. Geophys. Res., 106, 8357

McKenzie, J. F., Banaszkiewicz, M., Axford, W. I. 1995, A&A, 303, L45

Roussev, I., Galsgaard, K., Erdelyi, R., Doyle, J. G. 2001, A&A, 370, 298

Shimizu, T., Tsuneta, S., Acton, L. W., Lemen, J. R., and Uchida, Y. 1992, Publ. Astron. Soc. Japan, 44, L147

Tu, C. Y., Marsch, E. 1997, Solar Phys., 171, 363

Voitenko, Yu. M., Goossens, M. 2002a, Solar Phys., 206, 285

Voitenko, Yu. M., Goossens, M. 2002b, Solar Phys., 209, 37

Wilhelm K., Marsch E., Dwivedi, B. N. et al. 1998, ApJ, 500, 1023

NANO-SCALE RECONNECTION IN THE SOLAR TRANSITION LAYER

D. Marik
SPARC, Dept. of Applied Mathematics, Univ. of Sheffield
Hicks Building, Hounsfield Road, S3 7RH, sheffield, UK
E-mail: `D.Marik@sheffield.ac.uk`

Abstract

Magnetic reconnection in the lower transition region of the solar atmosphere is numerically simulated by solving the fully nonlinear, time-dependent, dissipative, radiative 2D MHD equations. Setting the initial parameters describing transition region explosive events, we computed the evolution of the reconnection jets. Taking into account the limit of the spatial and temporal resolution of the CDS camera and converting the high-resolution numerical results into 'CDS-resolution', the propagating reconnection jets are found to have similar properties as those described by CDS blinker observations. These results suggest SOHO CDS may actually observe reconnection driven explosive events as blinkers.

KEYWORDS: *Sun, MHD, blinkers, explosive events, transition region*

1. Observations

Transition region blinkers (TRBs) are observed in the past five years in the lower solar atmosphere. Numerous blinker observations followed their discovery by the Coronal Diagnostic Spectrometer (CDS) of the Solar and Heliospheric Observatory (SOHO) (Harrison (1997)).

Blinkers are best detected in the O V line and are found to occur in both active and quiet regions of the Sun. Typical behaviour of active-region blinkers is very similar to quiet-region blinkers (for more details see e.g. Bewsher et al. (2002)).

The mean lifetime of a blinker event is approximately 16 minutes, the mean rise and fall times are around 8 minutes and the intensity enhancement ratios are around 1.8. There is evidence that blinkers appear to be increases in density and/or filling factor rather than increases in temperature. Harrison et al. (1999) suggest it is probable that blinker events are driven by activity which most likely continues to dump energy into the plasma throughout the blinker duration. The mean area of blinkers is 2.9×10^7 km^2. The frequency of blinker events on the solar disk is 1 - 20 s^{-1}.

2. Blinkers as CDS signature of reconnection?

Marik & Erdélyi (2002) proposed a blinker model, coinciding best with the above observational findings, based on magnetic reconnection. Our aim is here to apply this model and to investigate the plasma jets driven by the process of magnetic reconnection in a 2D magnetic plasma representing the solar TR. Magnetic flux cancellation may be initiated by localized increase of magnetic diffusivity in a current concentration separating two magnetic flux tubes (Roussev et al. (2002)). Another driving mechanism could be the reconnection between randomly emerging magnetic flux at the boundary of active regions or supergranular cells where the newly emerged flux is pushed into the background magnetic field (Jin et al. (1996)). In both cases, reconnection results in jet ejections along the current sheet developed at magnetic shears. (Note it is *not* necessary to have opposite polarities! See, e.g. Zhang et al. (2000), Ryutova & Tarbell (2000).)

The above picture of reconnection is accepted as a probable mechanism driving explosive events (Innes et al. (1997), Erdélyi et al. (1997), Erdélyi & Sarro (1999), Erdélyi et al. (1999), Roussev el al. (2001b)). Explosive events (EEs) are strongly localised high velocity jets in the transition region observed by SUMER onboard SOHO (Erdélyi et al. (1998), Perez et al. (1998), Perez et al. (1999)). How could they link to slow speed TRBs observed by CDS? What could their role be in blinker evolution? In spite of the *apparently* distinctive character of these two phenomena we propose they may be manifestations of the same physical process observed by different instruments. CDS has, at most, a spatial resolution of $1.7'' \times 4.0''$ which is many times the area of an average explosive event on the solar surface. Hence, CDS provides unresolved *integrated signals* from a whole surface where many tiny and localised magnetic reconnections may occur. This may suggest blinkers could in reality be identical to EEs (or a series of them) but CDS cannot resolve these events. MHD reconnection simulations of EEs are carried out. The reconnection jet velocity and profiles are re-mapped into CDS resolutions. These re-mapped profiles are found not be in contradiction with observations describing TRBs.

3. The equilibrium model

The solar atmospheric plasma is considered as an ideal gas embedded in an intermittent inhomogeneous vertical magnetic field (y-coordinate), where xz is the plane of the solar surface with z-coordinate being the ignorable direction.

Gravity is neglected. The governing equations of a 2D dissipative, radiative MHD are considered (see, e.g. Roussev el al. (2001b) for details on inclusion of dissipation and radiation).

The initial magnetic field configuration describing a current sheet is given by $\mathbf{B} = (0, B_y(x), 0);\;\; B_y = B_0 \tanh(Cx/L_0)$, where L_0 and B_0 are typical values of length scale and magnetic field strength, respectively, and C is a constant. The initial equilibrium velocity is assumed to be zero throughout the computational domain. The total pressure balance is given by $B_y^2(x)/2 + P(x) = B_0^2/2 + P_0 = \text{const}$, where $P(x)$ is the kinetic gas pressure and can be computed once the initial magnetic field distribution, $B_y(x)$ is given. For the sake of simplicity a uniform kinetic gas pressure distribution in the y-direction is assumed as a first approximation resulting in the thermal energy, $e = P/(\gamma - 1)$, also being uniform along y (although in reality it decreases in height towards the solar corona). To represent the TR containing a current sheet the density stratification in the y-direction is given by $\varrho(y) = \varrho_0 \left\{1 + \Delta\varrho \left\{1 - \tanh\left[(\varepsilon/L_0)(y + y_s)\right]\right\}\right\}$, where ϱ_0 is a typical value of the mass density in the low density region and $2\Delta\varrho$ is the jump in density across the transition region. The corresponding equilibrium temperature profile is an increasing function in height, and is given by $T(y) = P/\varrho(y)$. The mass density distribution in the x-direction reads as $\varrho(x) = \varrho_0 \left(P/P_0\right)^\theta = \varrho_0 \left(e/e_0\right)^\theta$, where θ is a free parameter (one over the polytropic index) used to control the density profile in the current concentration. The full 2D profile of the mass density is computed by $\varrho(x, y) = \varrho(x)\varrho(y)/\varrho_0$. Using the equation of state $e = \varrho T/(\gamma - 1)$, one can derive the 2D temperature profile $T(x, y)$. Finally we also assume energy balance in the entire physical domain for the initial state: $S(x, y) - \nabla \mathbf{q}(x, y) - L_r(x, y) = 0$ at $t = 0$, where S, $\mathbf{q}$ and L_r are the volumetric heating rate, the heat flux and the radiative loss, respectively.

Magnetic reconnection is governed by a time-dependent localized magnetic diffusion $\eta_{loc} = \eta_0 F(t) \exp\left\{-\alpha/L_0^2[x^2 + (y + y_0)^2]\right\}$, where y_0 is a shift parameter and $\eta_0 = V_{A0} L_0/R_m$ (R_m is the magnetic Reynolds number, V_{A0} is the Alfvén speed given by $V_{A0} = B_0/\sqrt{\varrho_0}$) and $F(t)$ is a time dependent function.

4. Numerical Method

The numerical experiments are performed using a 2D compressible MHD code based on staggered mesh. The MHD equations are solved in a 2D domain using non-uniform staggered grids. The grids are stretched in the x-direction to better resolve the region around the current concentration in which the important dynamics of the experiment takes place. In the y-direction, however, there is no stretching applied since we need high resolution all the way throughout this direction of the domain. The MHD code used in our experiments conserves mass, momentum, energy, and magnetic field divergence.

5. Reconnection jets

The compressible fully nonlinear 2D MHD equations are solved for typical parameters of EEs. Our aim here is not to study the parameter space for EEs; this has recently been extensively done by Roussev et al. (2001abc, 2002), instead we focus on obtaining characteristic profiles of velocity, density and temperature distributions for EEs. These profiles will be re-mapped into CDS resolution and will be compared to TRBs. Fig. 1 shows there is a blue shifted jet propagating towards the high temperature region ($y > y_0$) with increasing velocity and there is a red shifted jet moving towards the high density region ($y < y_0$) submerging into the lower atmosphere.

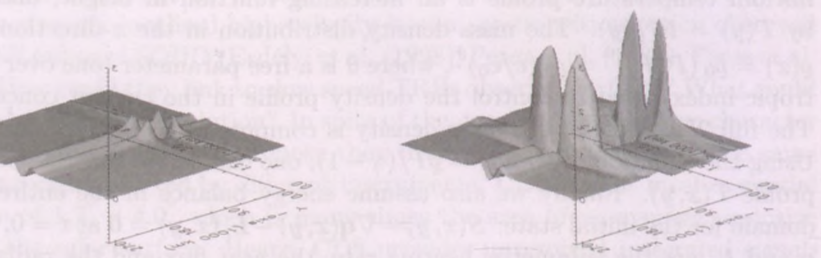

Figure 1: The evolution of the relative density distribution of the reconnection jets. The density is in units of $\varrho_0 = 2.54 \times 10^{-14}$ g cm^{-3}. The real times of the images are 205s (left), and 334s (right).

EEs simulated above (or seen by SUMER) appear to have different properties from blinker events seen by CDS as described above. They are smaller and their lifetime is much shorter. The observed velocity profiles also appear not to match, because EEs have a maximum jet head velocity around the TR Alfvén speed (as it should be!) while, according to recent spectral analyses TBRs do not really show considerable velocity enhancements. Blinker velocities of around 20 km/s are the upper limit (Harrison et al. (1999)).

Let us now re-map the obtained high spatial and temporal resolution results of the reconnection model of EEs in Fig. 1 by taking into account the resolution limits of a typical CDS observation of TRBs. We convert the velocity, temperature and density profiles of the outwards propagating blue jet of an EE. Before we proceed we recall: (i) a CDS pixel overlaps a $1.7'' \times 4''$ domain which actually corresponds to more than the whole EE area on the solar surface; (ii) the CDS exposure time is around 10 sec; (iii) images are averaged over the whole depth of a domain. Fig. 2a shows the difference between the numerical simulation (maximum speed in the line of sight) and what CDS would 'see' as an integrated velocity profile.

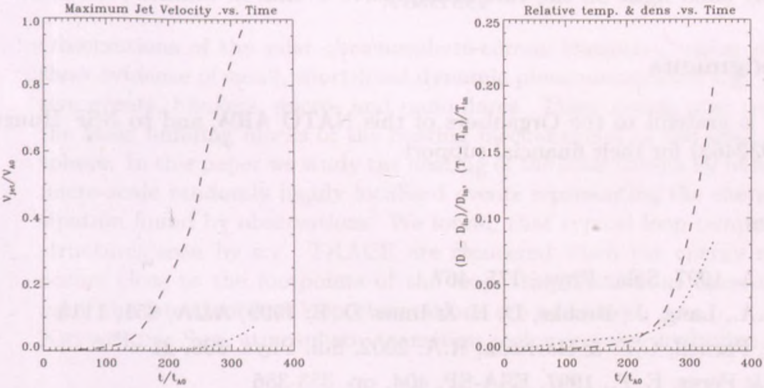

Figure 2: Left are the simulated (long dashed) and the re-mapped 'CDS-eye' integrated (dotted) velocity profiles obtained from the case study in Fig. 1. ($V_{A0} = 1.293 \cdot 10^2$ km s^{-1}, $t_{A0} = 23.2s$. Right are the corresponding relative density (long dashed) and the relative temperature (dotted) profiles.

Although there does not seem to be an obvious saturation of the integrated velocity profile around the 20 km/s observed maximum, it reaches much lower values than the actual simulations (Figure 2a) and remains well under this threshold. Unfortunately we cannot simulate blinkers for longer than 6-8 minutes as a 6 minutes event takes more than two days CPU to run. However, the location of the blue jet after 300 sec is already well in the solar corona anyway. Similarly in Fig. 2b one sees that the integrated, averaged relative temperature and density. Observe the enhanced density as speculated by Harrison (1997). These integrated velocity, relative temperature and density profiles suggest the reconnection model could describe blinkers.

On the other hand, one has to recall that 80-90% of blinkers are in unipolar magnetic field dominated areas which may contradict blinkers are the results of magnetic reconnection *unless* there is a shear in unipolar magnetic fields.

Sunspots in many cases show light bridges providing sheared fields. There is no reason to believe that smaller flux tubes cannot have such bridges as well. Two final comments: (i) The re-mapped density enhancement of an EE per CDS pixel may seem to be small. However, EE's show up very repeatedly in SUMER lines. (ii) The averaged temperature enhancement in Fig. 2b ($\approx 10\%$) is well within observation errors.

Statistical analysis of joint SUMER and CDS observations supported by high-resolution ground based magnetograms to construct a magnetic carpet of blinkers may shed light on the role of explosive events in blinker formation.

Acknowledgments

The author is grateful to the Organisers of this NATO ARW and to NSF Hungary (OTKA TO32462) for their financial support.

References

Harrison, R.A. 1997, Solar Phys., 175, 467

Harrison, R.A., Lang, J., Brooks, D. H. & Innes D. E. 1999, A&A, 351, 1115

Bewsher D., Parnell, C.E. & Harrison, R.A. 2002, Sol. Phys. 206, 21

Erdélyi, R. & Perez, E. P., 1997, ESA-SP, 404, pp. 353-356

Erdélyi, R., Sarro, L. M., & Doyle, J. G., 1998, ESA-SP, 421, pp. 207-211

Erdélyi, R. & Sarro, L. M., 1999, ESA-SP, 446, pp. 299-304

Erdélyi, R., de Pontieu, B & Sarro, L. M., 1999, ESA-SP, 448, 1345

Innes, D.E., Inhester, B., Axford, W.I. & Wilhelm, K. 1997, Nature, 386, 811

Jin, S.-P., Inhester, B. & Innes, D. 1996, Solar Phys., 169, 279

Marik, D. & Erdélyi, R., 2002, A&A, 393, 73

Perez, E. P., Doyle, J. G. & Erdélyi, R., 1998, ASP-CS, 154, 666

Perez, E. P., Erdélyi, R. & Sarro, L. M., 1999, A&A, 342, 279

Roussev, I., Doyle, J.G., Galsgaard K. & Erdélyi R. 2001c, A&A, 380, 719

Roussev, I., Galsgaard, K., Erdélyi, R. & Doyle, J.G. 2001a, A&A, 370, 298

——, 2001b, A&A, 375, 228

Roussev, I., Galsgaard, K. & Judge, P. G. 2002, A&A, 382, 639

Ryutova, M.P. & Tarbell, T.D. 2000, ApJ, 541, 29

Zhang, J., Wang, J., Lee, C.-Y. & Wang, H. 2000, Solar Phys., 194, 59

IMPULSIVE HEATING IN THE SOLAR ATMOSPHERE

C. A. Mendoza-Briceño[1,2] and R. Erdélyi[2]
[1]Centro de Astrofísica Teórica, Fac. de Ciencias, Univ. de los Andes
Aptdo Postal 26, La Hechicera, Mérida 5251, Venezuela
[2]SPARC, Dept. of Applied Mathematics, Univ. of Sheffield
Hicks Building, Hounsfield Road, S3 7RH, Sheffield, UK
E-mail: [1]`cesar@ciens.ula.ve`, [2]`robertus@sheffield.ac.uk`

Abstract

Observations of the solar chromosphere-corona transition region plasma show evidence of small, short-lived dynamic phenomena called e.g., explosive events, blinkers, micro- and nano-flares. These events may serve as the basic building blocks of the heating mechanism(s) of the solar atmosphere. In this paper we study the heating of the solar corona by numerous micro-scale randomly highly localized events representing the energy dissipation found by observations. We found, that typical loop temperature structures seen by e.g. TRACE are recovered when the energy release occurs close to the footpoints of the loop. Implications of these results upon the latest coronal loop observations are addressed.

KEYWORDS: *S*un, atmosphere, transition region, corona, hydrodynamics

1. Introduction

One outstanding problem in solar physics today concerns the heating of the solar corona. Recent interest has centered on the idea that the solar atmosphere is heated by small events, which are believed to be manifestations of localized magnetic field reconnection (Parker 1988), where direct current dissipation occurs. Since these events have associated about 10^{-9} times the energy of a typical large flare, they are usually called nanoflares. High resolution satellites (SOHO and TRACE) have revealed a kind of very small-scale activity at transition-region temperatures (Pérez et al. 1999; Erdélyi, De Pontieu, & Roussev 2001). More recently Benz & Krucker (2002) analyzed the energy distribution of the different microevents reported in the literature and estimated their total energy input into the corona, finding that the energy input observed by EIT on the SOHO satellite can be estimated to be of the order of 10% of the total radiative output in the same region. These heating events are candidate signatures of nanoflares (or microflares) proposed to explain the high temperature and the very existence of the corona.

Several authors have proposed hydrodynamic models to study the temperature evolution of coronal plasma loop under the assumption of a time-varying heating (e.g., Sterling, Shibata, & Mariska 1993; Walsh & Galtier 2000). Models with a spatially and temporally varying heating have also been considered to study impulsively heated solar flares (Mariska et al. 1989; Peres et al. 1987; Betta et al. 2001) and coronal loops maintained close to steady conditions (Reale et al. 1994; Betta et al. 1999). In particular, in the latter models the effects of releasing either periodic or random heat pulses at the loop apex were studied. On the other hand, Sarro et al. (1999) proposed numerical models to study the nature of explosive events (i.e., of impulsive mass motions) and their contribution to the coronal heating mechanism. The response of the coronal plasma loop to a dynamic heat input generated by the flux braiding model was studied by Walsh and Galsgaard (2000). More recently, Spadaro et al. (2002), Mendoza-Briceño et al. (2002), and Warren et al. (2002) investigated the hydrodynamic evolution of coronal loops undergoing transient heating.

In this paper, we investigate the response of the coronal loop plasma to randomly injected microscale heat pulses near the footpoints. In contrast with previous work (Mendoza-Briceño et al. 2002), here we consider the effects of asymmetrical energy releases near the footpoints of semi-circular loops.

2. Hydrodynamical Modeling

Since the plasma dynamics in a coronal loop is dominated by the magnetic field, we make the usual assumption that the plasma motion takes place primarily along the magnetic field lines which in turn determine the loop geometry. Heat conduction due to the electron diffusion also occurs along the field lines rather than across them. In this way, each plasma loop can be treated almost independently from the neighboring ones implying that the thermo-dynamical evolution of the coronal plasma along the field lines is essentially one-dimensional (1D). Under these conditions, the energy conservation equation, including the effects of thermal conduction and radiative cooling and heating reads

$$\frac{\partial(\rho T)}{\partial t} + \frac{\partial(\rho v T)}{\partial s} = -\frac{\mu(\gamma-1)}{\mathcal{R}_g}\left[p\frac{\partial v}{\partial s} + \rho^2 Q(T) - H(s,t) - \frac{\partial}{\partial s}\left(\kappa\frac{\partial T}{\partial s}\right)\right]. \quad (1)$$

In these equations, s denotes the position along a loop of constant cross-section, ρ is the plasma mass density, v is the fluid velocity, T is the plasma temperature, p is the gas pressure, $g(s)$ is the component of gravity along the field line, $Q(T)$ is the optically thin radiation-loss function, $H(s,t)$ is the coronal heating function,

$\gamma(=5/3)$ is the ratio of specific heats, μ is the mean molecular weight, and $\kappa \approx 10^{-11} T^{5/2}$ W m^{-1} K^{-1} is the coefficient of thermal conductivity parallel to the magnetic field (Braginskii 1965). The set of governing differential equations is closed by assuming a pressure relation of the form $p = \mathcal{R}_g \rho T/\mu$, where $\mathcal{R}_g$ is the gas constant.

Here we adopt many of the same parameters and assumptions that were used in Mendoza-Briceño et al. (2002), with the exception that now the condition of reflection symmetry about the apex is completely relaxed. In this way, the entire semi-circular loop is represented by the calculations. This allows for models of the cooling of loops that are being impulsively heated near their footpoints in an asymmetrical manner.

In order to describe the spatial and temporal variation of heating, we choose a function of the form

$$H(s,t) = h_0 + H_0 \exp(-\alpha t) \exp\left[-\frac{(s-s_0)^2}{\beta^2}\right], \tag{2}$$

where s_0 denotes the location of the heating pulse, $\beta \approx 3.6 \times 10^4$ m is the width of the heating, $h_0 = 3.6 \times 10^{-5}$ J m^{-3} s^{-1} is the constant background heating needed to maintain the initial atmosphere, $H_0 = 3$ J m^{-3} s^{-1} is the maximum amplitude of the impulsive heating and $\alpha = \ln(0.1)/\Delta t$. Hence, 90% of the total energy is deposited during a finite time Δt. For the calculations of this paper the time duration of the heating is taken to be $\Delta t = 150$ s. In particular, we study the response of the loop to random energy inputs of total energy $E_{tot} \sim 10^{18}$ J. The pulses are randomly injected in a small loop segment of length $0.1L$ from the footpoints, with elapsing times of either 60 or 120 s. In order to produce asymmetrical injections of the energy input near the footpoints, the random spatial distribution of the pulses on one loop segment is taken to be different from that on the opposite loop segment.

With the above prescriptions, the governing equations are solved numerically using the same 1D finite-difference hydrodynamics code employed in Mendoza-Briceño et al. (2002).

3. Results and Conclusions

All calculations start with initial conditions corresponding to a hydrostatic equilibrium loop of total length $L = 1.0 \times 10^7$ m (10 Mm), excluding the chromosphere. The initial atmosphere is such that the base pressure is 0.01 N m^{-2} for all cases. The boundary conditions are specified by fixing the same initial density and temperature at the two footpoints. Since $p \propto \rho T$, this is equivalent to assign a constant pressure at $s = 0$ and L. The presence of a deep chromosphere is here simulated by allowing mass to flow across the footpoints by just hydrodynamically evolving the velocity there. We first describe the case in which 10 randomly spaced pulses are released near the two footpoints, with the random spatial distributions (s_0) of the pulses being different on both sides. The time evolution of the loop temperature is displayed in Fig. 1a where a sequence of computed profiles along the entire loop length is shown at intervals of 10 s each. The pulses are randomly injected over a loop segment of $0.1L$ from the footpoint locations and with elapsing times of 60 s with the first pulse being injected at $t = 0$.

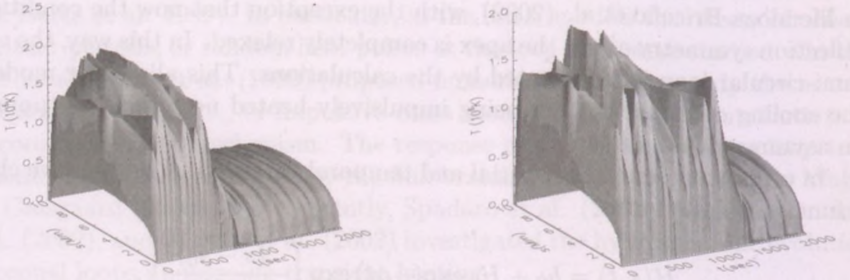

Figure 1: Evolution of the temperature along the loop length for 10 random pulses injected near the two footpoints. Different random spatial distributions of the pulses are used at each side. The time interval between successive pulses are: of 60 s (*Left*) and 120 s (*Right*) , with the first pulse being injected at $t = 0$.

For comparison, Fig. 1b depicts the resulting temperature evolution when the elapsing time between successive injections is increased from 60 to 120 s. The trends of the evolution are quite similar to those shown in Fig. 1a, with the exception that in this case the overall loop temperature is slightly reduced. The effects of increasing the elapsing time between successive pulses is more clearly seen in Fig. 2a, which shows the time variation of the temperature at the apex for the evolutions of Figs. 1a (solid line) and 1b (dashed line). On average summit temperatures around 1.5 MK are maintained during the first 540 s of the evolution for the model of Fig. 1a and during the first 1100 s for the model of Fig. 1b.

Fig. 2b shows two temperature profiles resulting from averaging in time the

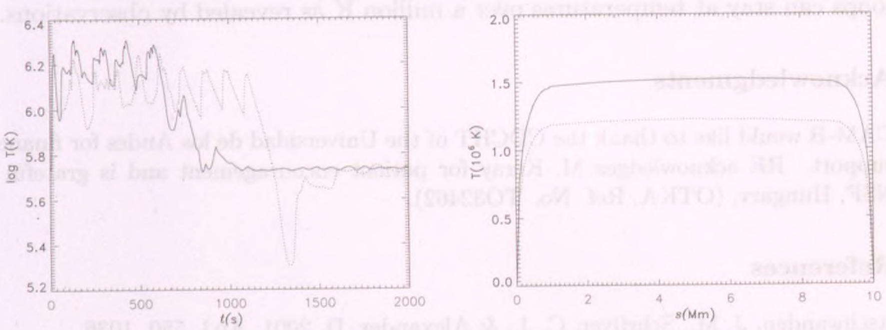

Figure 2: *Left:* Evolution of the summit temperature for the same models of Fig. 1a (solid line) and Fig. 1b (dashed line). *Right:* Integrated temperature profiles for the two random energy pulse distributions given at 60 s (solid line) and 120 s (dashed line) of elapsing times.

temperature evolution for the two models of Figs. 1a (solid line) and 1b (dashed line), all integrated over the first 550 s and 1100 s of the corresponding evolutions and for ten injected thermal pulses. The random temperature profile for elapsing time of 60 s show a higher summit temperature compared to the evolution with elapsing time of 120 s. From this figure we may also note that farther away from the footpoint the two curves reproduce a quasi-isothermal profile along the loop, suggesting a footpoint exponential decay heating as discussed by Aschwanden et al. (2001) and Mackay et al. (2000; see their Fig. 5b).

We have presented hydrodynamic loop simulations to study the response of the plasma to input energy releases near the footpoints of loops of semi-circular shape. In contrast with previous calculations, the entire loop length is represented by the calculations. This allows considering the effects on coronal heating for more realistic cases in which the injections on one side of the loop are not necessarily symmetrical with respect to the other side. The energy input was introduced as an additional heating term in the energy equation by just perturbing the initial hydrostatic equilibrium profile.

The calculations show that successive energy inputs can maintain the plasma along the loop at typical coronal temperatures. On the other hand, the appearance of localized thermal bumps along the loop length seem to be a pattern for models with random pulse injections. Such bumps could be related to the signatures observed by Patsourakos & Vial (2002).

In summary, we find that by dynamically injecting energy (e.g., as a result of nano-scale magnetic reconnection as predicted by Parker 1988) coronal plasma loops can stay at temperatures over a million K as revealed by observations.

Acknowledgments

CAM-B would like to thank the CDCHT of the Universidad de los Andes for financial support. RE acknowledges M. Kéray for patient encouragement and is grateful to NSF, Hungary, (OTKA, Ref. No. TO32462).

References

Aschwanden, J. M., Schrijver, C. J., & Alexander, D. 2001, ApJ, 550, 1036

Benz, A. O. & Krucker, S. 2002, ApJ, 568, 413

Betta, R. M., Peres, G., Reale, F., & Serio, S. 2001, A&A, 380, 341

Betta, R. M., Reale, F., & Peres, G. 1999, ESA SP-446, 179

Braginskii, S. I. 1965, Rev. Plasma Phys., 1, 205

Erdélyi, R., De Pontieu, B., & Roussev, L. M. 2001, ASP Conf. Ser, 223, 619

Mackay, D. H., Galsgaard, K., Priest, E. R., Foley, C. R. 2000, Sol. Phys., 193, 93

Mariska, J. T., Boris, J. P., Oran, E. S., Young, T. R., & Doschek, G.A. 1989, ApJ, 255, 783

Mendoza-Briceño, C. A., Erdélyi, R., & Sigalotti, L. Di G. 2002, ApJ, 579, L49

Parker, E. N. 1988, ApJ, 330, 380

Patsourakos, S. & Vial, J. C. 2002, A&A, 385, 1073

Pérez, E. P., Doyle, J. G., Erdélyi, R., & Sarro, L.M. 1999, A&A, 342, 279

Peres, G., Reale, F., Serio, S., & Pallavicini, R. 1987, ApJ, 312, 895

Reale, F., Peres, G., & Serio, S. 1994, in V. Rusin, P. et al. (eds), IAU Colloq. 144 Solar Corona Structures, 215

Sarro, L. M., Erdélyi, R., Doyle, J. G., & Pérez, E. P. 1999, A&A, 351, 721

Spadaro, D., Lanza, A.F., Lanzafame, A.C., Karpen, J.T., Antiochos, S.K., & MacNeice, P.J. 2002, ESA SP-505, in press

Sterling, A. C., Shibata, K., & Mariska, J. T. 1993, ApJ, 407, 778

Walsh, R. W. & Galsgaard, K. 2001, ESA SP-493, 427

Walsh, R. W. & Galtier, S. 2000, Sol. Phys., 197, 57

Warren, H. P., Winebarger, A. R., & Hamilton, P. S. 2002, ApJ, 579, L41

Published by the Department of Astronomy of the Eötvös University
Budapest 2003

This volume contains focus reviews, oral contributions and poster paperspresented at the NATO Advanced Research Workshop "Turbulence, Waves, andInstabilities in the Solar Plasma", held at Hotel Normafa, Budapest, 16--20September, 2002.

The purpose of the workshop was to facilitate interchange andcommunication between diverse groups studying different layers and regions ofthe Sun but from the same aspect, concentrating on the study of small-scalemotions. While the emphasis was on the common theoretical roots of thesephenomena, observational aspects were not excluded either.